Large-Scale Structure of the Earth's Mantle and Inner Core

A thesis presented
by
Miaki Ishii
to
The Department of Earth and Planetary Sciences
in partial fulfillment of the requirements
for the degree of
Doctor of Philosophy
in the subject of
Geophysics
Harvard University
Cambridge, Massachusetts
April, 2003

Professor Adam M. Dziewoński
Professor Göran Ekström
Professor Jeroen Tromp

Miaki Ishii

Large-Scale Structure of the Earth's Mantle and Inner Core

Determining the internal structure of the Earth has been one of the main focus of seismology, since it can be related to the composition, dynamics and evolution of the planet. Large-scale perturbations within the mantle and the inner core are sought in this study, using mainly splitting of the normal modes, or free oscillations, of the Earth. This data set is complemented by gravity anomalies and body wave travel times in mantle and inner core modelling, respectively.

Using the unique sensitivity of normal modes, three-dimensional models of shear wave speed, compressional wave speed, and density within the mantle are obtained. The mode data limit the models to be only large-scale, even degree structures. Nonetheless, the wave speed models compare favourably with existing models constructed using other seismic data. The attempt to resolve density variations for the mantle based upon seismic observations is the first of its kind, and the model shows some interesting features. In particular, dense material is observed at locations of strong wave speed reduction near the core-mantle boundary. In general, comparison of the various models suggests that the mantle may not be as chemically homogeneous as previously thought.

The inner core is believed to be transversely isotropic, but the degree and complexity of anisotropy varies wildly from one model to another, partly dependent on the type of data used. To obtain a global model which satisfies normal mode observations, body wave absolute and differential travel times, these three sets of data are inverted simultaneously. The resulting model does not vary with radius, and is only weakly anisotropic. Analysis of misfits also indicates that the discrepancies between existing models originate due to biased sampling, contamination from mantle structure, and/or small-scale variations that may be in the inner core or the mantle.

However, the absolute travel times from antipodal distances show globally coherent deviations from the above anisotropy model. They imply that anisotropy within the central 300 km of the Earth differs significantly from the bulk inner core. The existence of such a distinct layer suggests various possibilities for the elastic properties and chemistry of the inner core material, and the dynamics and evolution of the Earth's core.

Contents

List of Figures

List of Tables

To
Michiko Yoshina
who firmly believed that her wild grand-daughter
will someday accomplish something.

Preface

The work presented in this thesis began when Prof. Jerry X. Mitrovica, my undergraduate supervisor at the University of Toronto, casually suggested that I go to Harvard University for the summer and work with a seismologist. I was introduced to Prof. Jeroen Tromp, visited Harvard in April, and started working in May.

The focus of this study is on analysing normal mode splitting for structure within the Earth. We started by looking at mantle modes in order to constrain the mantle, and one of the results, a three-dimensional density model is still a controversial issue. There are many tests performed to convince the reviewers, but more importantly, ourselves, that normal mode can provide reliable constraints on density variations. Most of the tests are presented in this thesis, including those which are left out of published papers as supplementary material.

When we turned to inner core modes, we noticed a coherent non-zonal pattern. To better understand this feature, we first wanted to know inner core anisotropy. This study began very simply, using only mantle corrected inner core mode data. It quickly expanded to include absolute travel times, and then differential travel times. The mantle modes were also re-introduced to the analysis when the inversion scheme was changed to obtain mantle and inner core structure simultaneously. This approach was beneficial: mantle density was constrained better with the additional modes, and combination of various data isolated signal due to global anisotropy. With the new mantle and inner core models, the mode data are explained quite well, and the peculiar non-zonal pattern in inner core modes diminished significantly, although some of it is still left in residual splitting pattern.

About the time the inner core study began, Jeroen moved to Caltech, so this research was done with Jeroen and my two new advisors, Prof. Adam M. Dziewoński and Prof. Göran Ekström. Whenever I spoke about our inner core study, Adam would comment how strange it is that the absolute travel time data from antipodal distances behave so differently than those from shorter distances. At first, I attributed this to the small number of observations, but the pattern remained even when the data set was divided into subsets. This, and additional analyses, led Adam and I to propose that there is an inner-most inner core. The tests, I believe, give quite convincing evidence, although it is true that the database is not large enough to robustly determine the axis of symmetry.

I consider myself fortunate to have had not one, but three great seismologists as my supervisors. Jeroen was very generous and patient with me. Regardless of how basic or silly my questions may be, he was willing to spend some time answering them. Usually, he would drop by at the end of the day and say "how is life?" There were always too many things happening in life to describe, so my typical response was "fine," which, I later realised, was not a good way to start a conversation. Nonetheless, we often had nice chats and it was clear that Jeroen cared much for my well being, and perhaps, I was a little spoiled by that.

When I decided to stay at Harvard, Adam and Göran kindly agreed to be my supervisors. I must admit that I was afraid of both of them at the beginning, especially Adam. But soon, I found out that "a bit stiff" and "serious" outward look of Adam (as described in *Naked Earth: The New Geophysics*) is just an appearance. He made efforts to know how and what I was doing, and that was a great comfort. With his vast knowledge and experience of the field, he would make many suggestions, more quickly than I could follow up. In fact, there are ideas that are still left unpursued.

I hope to pursue them one day.

Adam's first words, when he comes to the computer room, are "how are things?" I am yet to learn what Göran's favourite question is. Nevertheless, Göran's comments intrigued me the most, and very often, they reassured me that I was doing something reasonable. For some reason, he represented security in my mind, and I benefitted much from it, particularly after a harsh review. I am also grateful that he went through my thesis meticulously, making corrections or writing comments on almost every other page. They were most valuable in revising this thesis. I sincerely thank my supervisors for their kindness, various forms of encouragements, and putting up with me. Without their guidance and care, I would not have accomplished as much, and my life as a graduate student would have been rather miserable.

There are others who also made my being at Harvard one of the happiest times. For example, I always had wonderful officemates who tolerated me: Dr. Gideon Smith, Dr. Weijia Su, Dr. Svetlana Panasyuk, Dr. Dimitri Komatitsch, and Bogdan Kustowski. I enjoyed chatting with them, to get a glimpse of how they work, and to learn some useful tricks. I also owe many thanks to others in the seismology group to whom I could turn whenever I had a problem: Meredith Nettles, Dr. Erik Larson, Dr. Yu (Jeff) Gu, Dr. Xian-feng Liu, Dr. Lapo Boschi, Karen Felzer, Dr. Rachel Abercrombie, Dr. Mike Antolik, and Jianfeng Pan. In particular, Karen not only put up with my odd habits as a housemate, but she helped revising the thesis. I would also like to thank technical and other assistances I got from William Toth, Kathy Harrow, and Michael Barrera. It amazes me that everyone in the group is so willing to help, which makes this place so charming. I am proud to have been a part of it.

There are others outside of the seismology group who made being a student here more exciting and a happy experience. Prof. Richard J. O'Connell gave me many thoughtful comments and remarks which were very valuable and often cheered me up. He always received me happily in his office for consultation or anything else, and his numerous good advice were much appreciated (including a suggestion to use lard for pie pastry, although, even with this, I still can't get it right). I also thank kindness shown to me by Dr. Renata Dmowka and Prof. Jim Rice. Dinners at their home were fun with good conversation, and I enjoyed every one of them. I will not forget that both Renata and Jim spent few hours talking to me when I was going through the difficulties of deciding whether to go to Caltech or to stay at Harvard.

Spending my time with Sybil and Adam Dziewoński was always pleasant, but especially so at their beautiful home with the prize garden. I spent many relaxing and happy afternoons with them, most of which were more refreshing than being home in Canada. Sybil and Adam generously pampered me, more than I probably deserve. I particularly admire Sybil. I have never met such a strong, independent, and intelligent woman who is, at the same time, so affectionate. I am truly grateful for what they have done for me in the last few years.

I would not be finishing up my thesis as I do now, without continual encouragements, advice, and moral support from Jerry X. Mitrovica. In fact, I do not think I would be in geophysics if he did not teach the first year physics course in 1994. Jerry is a great source of inspiration, wonderful mentor and friend. He helped me not only scientifically, but also with mundane things such as answering my banal questions (e.g, what is a CV?) and deleting/adding the's and a's in my manuscripts. Meeting him at the University of Toronto was my luckiest encounter, and I can never thank him enough (including hundreds of colour figures which almost bankrupted him). Jerry, thank you so much for guiding me throughout my undergraduate and graduate years.

Finally, I would like to thank my parents, Hiromi and Takashi Ishii, for their understanding and support. Care packages from Canada and Japan brought wonderful surprises and change to busy but somewhat monotonous days. I am happy to announce that the future we discussed at length on the phone (i.e., my being jobless and living at their expense) does not appear to be an immediate possibility. I would also like to thank my sister Chiaki, who endured long hours of my hopeless babbling. I do sympathise that it must be difficult to have me as an *older* sister.

I tried to shorten this thesis as much as possible without leaving out too much detail. I doubt that no one (with the exception of Göran, Adam, Rick, Prof. Jeremy Bloxham, and perhaps Jeroen and Jerry) is going to read it fully, but if it is still too long, well, my apologies.

with gratitude,
Miaki Ishii
March 07, 2003

Chapter 1

Introduction

Most of the Earth's interior is not physically accessible, due to rapidly increasing temperature and pressure. Seismic energy propagating through the Earth, recorded at seismic stations scattered on the surface, provide valuable data for understanding the internal properties. Early studies have documented that there are distinct layers within the Earth: the crust, mantle, outer core and inner core. Models of radially varying seismic wave speeds and density can be interpreted for the bulk composition of various layers, however, they cannot be immediately related to dynamic processes. Furthermore, observations indicate that there are significant deviations from these one-dimensional models, i.e., lateral variations and anisotropy. A brief description of each layer is given here to illustrate the motivation for the study undertaken in the following Chapters.

The crust is the layer with the strongest lateral variations both in terms of its thickness (oceanic crust is about 5 km thick, whereas continental crust can be as thick as 80 km), elasticity, and density. Fortunately, this is also the best sampled layer with rock samples, surface waves, topography, and so on. The properties of the crust are not investigated in this study, but data sampling deeper structure inevitably contain signal from the crust. Therefore data are corrected for crustal structure using an existing crustal model.

The mantle extends from 3500 to 6300 km radius of the Earth. It consists mainly of silicates and oxides of magnesium and iron, whose density results in nearly constant gravitational acceleration from the core-mantle boundary to the surface (e.g., Dziewoński & Anderson, 1981). Convection within this layer is driven by density variations, and is observed at the surface as plate tectonics. Much of seismic tomography efforts focus on the mantle, because lateral variations in seismic wave speeds can be related to this dynamic process. For example, images of subducted lithosphere (e.g., van der Hilst et al., 1997), depending upon whether it reaches the core-mantle boundary or not, give an indication of the mode of mantle convection (i.e., layered or whole mantle). Undulations of various discontinuities within the mantle also provide information on convection, as well as temperature and chemical variations (e.g., Gu et al., 1998). Seismic models can be compared with geochemical or mineralogical observations. Various geochemical signatures require different reservoirs within the mantle, which must be consistent with seismic images. Furthermore, regions of slow wave propagation in the deep mantle, associated with rising plumes, are often considered in conjunction with the chemistry of oceanic island basalts. Suggestions of compositional variations within the mantle, especially near the core-mantle boundary, have stimulated experiments and calculations of mantle minerals.

Tomographic models are also used as the input for obtaining other properties of the Earth's interior. For example, data such as gravity field variations, glacial rebound, and plate velocities, are inverted for mantle rheology using density distribution obtained from variations in seismic wave speed. Because there are significant consequences and applications for three-dimensional model of the mantle, seismic tomography has become a very popular topic of study. Most mantle models are given in terms of seismic wave speeds, but a density model would be more desirable in geodynamic studies. Such a model will take away one source of uncertainty, the relationship between variations in seismic wave speed and density distribution.

The outer core is the shell between 1200 and 3500 km radius. It is made up of liquid iron with a small amount of light elements. Because of the heavy iron, gravitational acceleration increases almost linearly with radius within the core to a nearly surface value at the core-mantle boundary. Viscosity of the outer core is estimated to be close to that of water (Gans, 1972; Poirier, 1988; de Wijs et al., 1998), and convection of iron in this layer generates the magnetic field. The liquidity and vigour of convection destroys heterogeneities with seismically detectable strength. Consequently, the outer core is assumed to be homogeneous throughout this study.

The solid inner core beneath the outer core is about 1200 km in radius, i.e., 30% smaller than the Moon; nonetheless, its iron composition makes it 35% heavier than the Moon. In comparison to Earth, the inner core constitutes less than 2% of Earth's mass occupying less than 1% of its volume. This tiny inner core has played and continues to play an important role in the evolution of the planet. Growth of the inner core provides a source of thermal (Braginsky & Roberts, 1995; Lister & Buffett, 1995) and compositional (Braginsky, 1963; Gubbins, 1977; Loper & Roberts, 1978) buoyancy for powering the geodynamo, and the solid sphere at the centre of the Earth acts to stabilize the magnetic field (Hollerbach & Jones, 1993; Glatzmaier & Roberts, 1995a). However, the inner core remains a poorly understood region compared to other layers because most seismic waves do not sample it and the extreme pressures and temperatures are not easily reproduced in the laboratory.

Unlike the mantle, the inner core can be sampled only by seismic methods. Studies have revealed that the inner core has some peculiar properties. Waves passing through the inner core travel at different speeds depending upon the direction in which they are propagating. Furthermore, some data suggest that the inner core may be rotating faster than the Earth itself. This super rotation has been used to constrain viscosity of the inner core (Buffett, 1997; Creager, 1997). However, models of anisotropy and super rotation vary considerably. Chapter 4 investigates anisotropy of the inner core and constructs a model which is consistent with a suite of disparate seismic observations.

This thesis addresses the question of large-scale variations within the mantle and inner core by mainly analysing seismic data. Chapter 2 presents background information on the data, theory, and modelling approach. The successive Chapters, 3 through 5, examine results for mantle, inner core, and a new region at the centre of the Earth, the inner-most inner core. The final Chapter discusses the importance and implications for internal structures from both seismological and non-seismological points of view.

Chapter 2

Data and Theory

2.1 Material Properties

Seismological studies of the Earth's interior focus upon elastic properties and density of the internal material. Assuming that only small stresses act on the material, stress and strain are related linearly through a fourth-order elastic tensor Λ. Even though it has 81 elements ($3 \times 3 \times 3 \times 3$ elements), physical conditions reduce the number of independent parameters to 21 without loss of generality. A conventional shorthand expresses the elements of this fourth-order tensor with only two indices. This notation, often used by engineers, assign a single index (ranging from 1 through 6) for each pair of original indices so that $1 = 11$, $2 = 22$, $3 = 33$, $4 = 23 = 32$, $5 = 13 = 31$, and $6 = 12 = 21$. For example, Λ_{1123} is written as Λ_{14}.

Determining all 21 independent elements of the elastic tensor may be the ultimate goal of seismology, but unlike a laboratory experiment, there are many limitations which make such attempts impractical. Instead, certain symmetry of a given material is assumed to further reduce the number of unknowns. Most studies of the lateral variations within the mantle assume that the mantle material behaves isotropically. Geodynamically, the vigorous mixing of the mantle is expected to produce isotropic interior, and investigation of the bulk mantle suggest that very little anisotropy exists (e.g., McNamara et al., 2001). However, considerable anisotropy has been reported for the upper-most and lower-most mantle, i.e., at the thermal boundary layers (e.g., Dziewoński & Anderson, 1981; Ekström & Dziewoński, 1998; Kendall, 2000). Anisotropy of the bottom thermal boundary should not affect results presented in this work, because data used to constrain mantle structure are sensitive broadly to structure near the core-mantle boundary. Hence effects due to this anisotropic layer will likely be small compared to the signal due to isotropic structure. This is not true for near-surface anisotropy, and the effects of such anisotropy on isotropic modelling need to be addressed.

The inner core observations, on the other hand, is explained well with transverse isotropy. No significant deviations from this anisotropy have been observed, although there are arguments that the top-most inner core is isotropic (e.g., Song & Helmberger, 1995; Ouzounis & Creager, 2001; Song & Xu, 2002). The tilt of the symmetry axis is a debated issue (e.g., Shearer & Toy, 1991; Creager, 1992; Su & Dziewoński, 1995; Song & Richards, 1996; McSweeney et al., 1997), but it is generally inferred to be much less than 10° from the rotation axis. This degree of tilting is likely to be within the uncertainty of the normal mode data. Transverse isotropy with the symmetry axis aligned with the rotation axis is therefore considered for most part of this study unless otherwise noted.

2.1.1 Isotropy

A material is isotropic if its elastic properties are identical in all directions. For example, an aggregate body with randomly oriented crystals exhibits this type of behaviour. An elastically isotropic material is described by two independent Lamé parameters μ and λ. The non-zero elements of the elastic tensor are then,

$$\begin{aligned}
&\Lambda_{11} = \Lambda_{22} = \Lambda_{33} = \lambda + 2\mu, \\
&\Lambda_{12} = \Lambda_{21} = \Lambda_{23} = \Lambda_{32} = \Lambda_{13} = \Lambda_{31} = \lambda, \quad \text{and} \\
&\Lambda_{44} = \Lambda_{55} = \Lambda_{66} = \mu.
\end{aligned}$$

It is physically appealing to introduce the bulk modulus, $\kappa = \lambda + \frac{2}{3}\,\mu$, which represents incompressibility of the material. The first Lamé parameter μ, i.e., the shear modulus, also has a clear physical meaning: it describes the rigidity of the material. In isotropic modelling presented in this study, μ and κ will be used as the two mineral physical properties rather than μ and λ.

Alternatively, an isotropic body can be characterised by two seismic wave speeds, compressional wave speed υ_P and shear wave speed υ_S. This parametrisation is favourable in seismic studies, where observations come from compressional and shear waves. The two wave speeds are related to the parameters μ and κ as well as density ρ by

$$\rho\,\upsilon_S^2 = \mu \qquad \text{and} \qquad \rho\,\upsilon_P^2 = \kappa + \frac{4}{3}\,\mu.$$

Sometimes, compressional wave speed is replaced by bulk sound speed υ_ϕ to better relate seismology and mineral physics. υ_ϕ is related to other parameters as

$$\rho\,\upsilon_\phi^2 = \kappa \qquad \text{and} \qquad \upsilon_\phi^2 = \upsilon_P^2 - \frac{4}{3}\,\upsilon_S^2.$$

The mantle modelling in Chapter 3 considers three sets of parametrisations (μ, κ, ρ), $(\upsilon_S, \upsilon_P, \rho)$, or $(\upsilon_S, \upsilon_\phi, \rho)$ can be considered.

The radial variation of these parameters is relatively well understood. Consequently, much effort has been concentrated in obtaining lateral variations. Most of mantle tomographic studies investigate perturbations in isotropic parameters relative to a radial Earth model. Perturbations in seismic parameters $\frac{\delta\,\upsilon_S}{\upsilon_S}$, $\frac{\delta\,\upsilon_P}{\upsilon_P}$, and $\frac{\delta\,\upsilon_\phi}{\upsilon_\phi}$ can then be related to perturbations in elastic moduli $\frac{\delta\,\mu}{\mu}$ and $\frac{\delta\,\kappa}{\kappa}$, and density $\frac{\delta\,\rho}{\rho}$ as

$$\begin{aligned}
\frac{\delta\,\upsilon_S}{\upsilon_S} &= \frac{1}{2}\left(\frac{\delta\,\mu}{\mu} - \frac{\delta\,\rho}{\rho}\right), \\
\frac{\delta\,\upsilon_P}{\upsilon_P} &= \frac{1}{2}\left[\frac{\upsilon_\phi^2}{\upsilon_P^2}\,\frac{\delta\,\kappa}{\kappa} + \frac{4}{3}\,\frac{\upsilon_S^2}{\upsilon_P^2}\,\frac{\delta\,\mu}{\mu} - \left(\frac{\upsilon_\phi^2}{\upsilon_P^2} + \frac{4}{3}\,\frac{\upsilon_S^2}{\upsilon_P^2}\right)\frac{\delta\,\rho}{\rho}\right], \qquad \text{and} \\
\frac{\delta\,\upsilon_\phi}{\upsilon_\phi} &= \frac{1}{2}\left(\frac{\delta\,\kappa}{\kappa} - \frac{\delta\,\rho}{\rho}\right).
\end{aligned}$$

Note that the reference values of υ_P, υ_S, and υ_ϕ are required to obtain perturbations in compressional wave speed from perturbations in μ, κ, and ρ.

2.1.2 Transverse Isotropy

A material is transversely isotropic if it exhibits cylindrical symmetry about an axis. Love (1927) uses parameters A, C, F, L, and N to specify this condition, where the parameters A and C are related to the speed of compressional waves travelling perpendicular and parallel to the symmetry axis, respectively, and the parameters L and N are associated with shear waves travelling parallel and perpendicular to the symmetry axis, respectively. The last parameter F describes how the waves are affected if they do not travel purely parallel or perpendicular to the symmetry axis. If one assumes that the symmetry axis is in the z-direction, Love's parameters are related to elements of the elastic tensor. The non-zero elements are

$$\begin{array}{lll} \Lambda_{11} = \Lambda_{22} = A & \Lambda_{12} = A - 2N & \Lambda_{44} = \Lambda_{55} = L \\ \Lambda_{33} = C & \Lambda_{13} = \Lambda_{23} = F & \Lambda_{66} = (\Lambda_{11} - \Lambda_{12})/2 = N. \end{array}$$

In the investigation of the inner core anisotropy (Chapters 4 and 5), the average shift in a normal mode frequency (i.e., at spherical harmonic degree zero) or constant offset in body wave travel times is not considered (see Section 2.2.3). This reduces the number of independent parameters to three, and following Woodhouse et al. (1986) and Tromp (1993, 1995b), they are defined as

$$\alpha = (C - A)/A_0, \qquad \beta = (L - N)/A_0, \qquad \text{and} \qquad \gamma = (A - 2N - F)/A_0, \tag{2.1}$$

where $A_0 = \rho_0 v_0^2$ is calculated using the density ρ_0 and compressional wave speed v_0 at the center of the spherically symmetric and isotropic reference Earth model PREM (Dziewoński and Anderson, 1981). Physically, α and β describe the relative difference in elastic parameters for compressional and shear waves travelling, respectively, parallel and perpendicular to the symmetry axis. Because only compressional wave data are available for body wave studies of the inner core, the number of independent parameters constrained by these data is further reduced to two. As discussed in section 2.2.3, there are different ways of defining the two independent parameters. This study uses definition following Morelli et al. (1986) with

$$\epsilon = \frac{C - A}{2\rho v_P^2} \qquad \text{and} \qquad \sigma = \frac{-A - C + 2F + 4L}{2\rho v_P^2},$$

where ρ and v_P^2 are obtained from the reference model. The parameters ϵ and σ can also be written in terms of α, β, and γ as

$$\epsilon = \frac{A_0}{\rho v_P^2} \frac{\alpha}{2} \qquad \text{and} \qquad \sigma = \frac{A_0}{\rho v_P^2} \left(2\beta - \gamma - \frac{\alpha}{2}\right). \tag{2.2}$$

2.2 Data

There are various data observed at the surface that contain information about the internal structure of the Earth. To investigate large-scale mantle heterogeneities, normal mode and gravity data are used in Chapter 3. In contrast, inner core studies in Chapters 4 and 5 include only seismic data: normal modes and body wave travel times.

2.2.1 Normal Modes

A normal mode, or free oscillation, of the Earth is a standing wave resulting from the constructive and destructive interferences of seismic waves travelling in opposite directions around the globe. A normal mode has a single characteristic frequency, however, any deviation of the Earth from sphericity results in the splitting of the resonance peak. There are three mechanisms that cause splitting of the modes: rotation, hydrostatic ellipticity and deviations from spherical symmetry such as lateral variations within the mantle. The effects of Earth's rotation and hydrostatic ellipticity can be predicted, and the remaining splitting, represented as splitting functions, can be used to constrain lateral variations in the mantle or transverse isotropy of the inner core.

Splitting Function Coefficients

A seismogram, $s(t)$, is related to the normal modes by

$$s(t) = \Re\mathrm{e}[\mathsf{r} \exp(i\mathsf{H}t)\mathsf{s} \exp(iwt) \exp(-qt)], \tag{2.3}$$

where r is the receiver vector combining instrumental response and modal displacement eigenfunctions, H is the splitting matrix of the modes, s is the source vector containing information on the earthquake mechanism, w is the characteristic frequency of the modes, and q is the decay rate (Woodhouse & Girnius, 1982). The real part of splitting matrix H of an isolated mode can be written as

$$\mathsf{H}^{mm'} = W^{mm'}\delta_{mm'} + \sum_{s,t} c_s^t \gamma_s^t, \tag{2.4}$$

where m is the angular order of the mode's singlet. The first term on the right hand side in equation (2.4) describes the effects due to the Earth's rotation and hydrostatic ellipticity:

$$W^{mm'} = (a + bm + cm^2)\delta_{mm'},$$

where b represents the first-order effect of the Earth's rotation (analogous to Zeeman splitting of hydrogen energy spectrum), and a and c represent the ellipticity and second-order rotation effects (Dahlen & Tromp, 1998). Using the known rotation rate and ellipticity of the Earth, $W^{mm'}$ can be calculated accurately (Woodhouse & Dahlen, 1978). The second term on the right hand side of equation (2.4) represents the splitting of the resonance peak due to internal structure related to spherical harmonic angular degree s and order t. Because isolated modes are standing waves, they are only sensitive to even degree structure. Effects due to odd degree structure are cancelled by destructive interferences, hence such structure cannot be modelled using isolated mode data. This standing wave condition is realised by the factor γ_s^t which, for an isolated mode, is zero when s is odd. The coefficients c_s^t contain information on the internal structure as sensed by the given mode. For this reason, they are sometimes referred to as structure coefficients. They are also called, because they determine splitting of a resonance peak, splitting function coefficients.

The splitting of a mode can be visualised in two dimensions using splitting function coefficients. Employing fully normalised spherical harmonics $Y_s^t(\hat{\mathbf{r}})$ (Edmonds, 1960), where $\hat{\mathbf{r}}$ denotes a point on the unit sphere, the splitting function σ is given by (Giardini et al., 1987)

$$\sigma(\hat{\mathbf{r}}) = \sum_{s=0} \sum_{t=-s}^{s} c_s^t Y_s^t(\hat{\mathbf{r}}).$$

Values of this two-dimensional map at a given point represents a local radial average of the underlying structure which is filtered through the mode's unique sensitivity to structure. Each mode has its own splitting function, and for modes with high angular degrees, it is equivalent to a surface wave phase velocity map. Depending upon whether the mode is dominantly sensitive to mantle or to the inner core, one can divide modes into mantle and inner core modes. Splitting functions of some mantle and inner core modes are compared in Figure 2.1. Because sensitivity to structure differs from mode to mode, the splitting functions are also unique to each mode, but the mantle modes are generally characterised by degree 2 order 2 pattern, whereas the inner core modes show strong zonal dependence.

In earlier normal mode studies (Giardini et al., 1987; Ritzwoller et al., 1988; Li et al., 1991a), splitting function coefficients of very long period, isolated spheroidal modes were determined for degrees 2 and 4 (Giardini et al., 1987, 1988; Ritzwoller et al., 1988). The occurrence of several large earthquakes in 1994–1996 has motivated new normal mode studies, and as a result, the quality and quantity of splitting function coefficients have improved dramatically. Compared to earlier data sets, higher-degree coefficients corresponding to smaller-scale structures have been measured up to angular degree and order 12 (Ritzwoller & Resovsky, 1995; He & Tromp, 1996; Resovsky & Ritzwoller, 1998). Another improvement to the data set comes from the addition of isolated toroidal modes (Tromp & Zanzerkia, 1995; Resovsky & Ritzwoller, 1998). These modes provide valuable additional constraints on shear velocity structure.

The sources of splitting function coefficients used in this study are summarised in Table 2.1. This database includes both spheroidal and toroidal modes with a considerable number of inner core

Figure 2.1: Splitting Functions of Mantle and Inner Core Modes

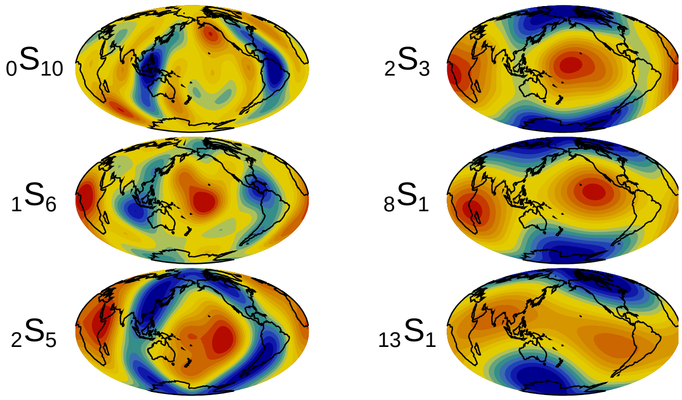

Comparison of the splitting functions of dominantly mantle sensitive modes (left) and modes with significant sensitivity to the inner core (right). The difference in pattern between the two types of modes is clearly evident. These splitting functions are obtained using coefficients determined by He & Tromp (1996).

Table 2.1: Summary of Splitting Function Coefficients of Isolated Modes

	Number of Modes				Modelling	
Source	S	T	mantle	IC	mantle	joint
Tromp & Zanzerkia (1995)	0	11	11	0	●	●
He & Tromp (1996)	67	0	36	31	●	●
Resovsky & Ritzwoller (1998)	72	41	97	16	●	●
Durek & Romanowicz (1999)	25	0	0	25		●
Masters et al. (2000a)	75	43	118	0		●

A table summarising the number of modes from a given source, divided by the type of modes: spheroidal (S) or toroidal (T), and mantle or inner core (IC) modes. A mode is considered to be an inner core mode if it has more than 0.1% of its energy is in the inner core. The modelling exercise for which the data sets are included are also indicated. The “mantle” modelling inverts only for mantle structure, and hence uses only the mantle modes from each source. In contrast, the “joint” modelling attempts to simultaneously obtain mantle and inner core structure, and uses all splitting function coefficients available.

Figure 2.2: Dispersion Diagram with Modes Used in Modelling

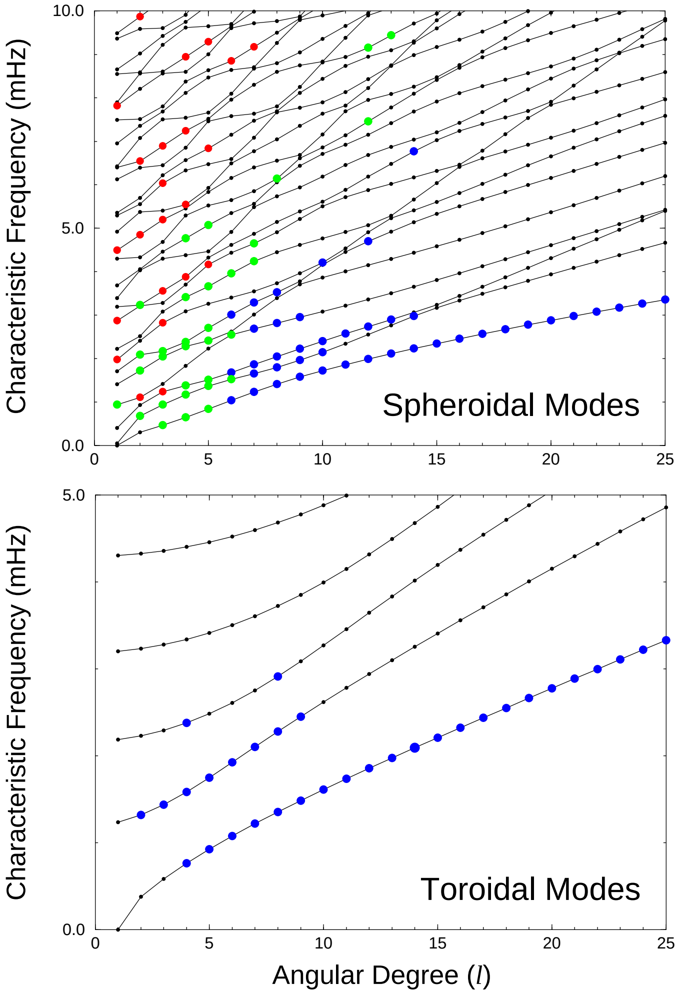

Dispersion diagrams identifying the mantle (blue), weak inner core (green), and inner core (red) modes used in constraining the internal structure. The angular degree (ℓ) of modes goes up to 25 in order to emphasise low ℓ overtone measurements. However, there are splitting function coefficients for fundamental spheroidal and toroidal modes up to degree 60 and 49, respectively.

sensitive modes. In some cases, the measurements of splitting coefficients of a mode is available from different groups. All measurements are included as independent constraints, much like using multiple rays passing through the same region in body wave tomography. To illustrate the range of frequency, angular degree, and overtones covered by the data set summarised in Table 2.1, modes with measurements are highlighted on the dispersion diagram in Figure 2.2. In Figures 2.3 and 2.4, splitting function coefficients of mantle modes (used in mantle only inversion) from three different sources are compared for their consistency. In general, the coefficients agree within assigned uncertainty, which suggests that the source of splitting function coefficients will not influence modelling results significantly.

The maximum angular degree s of splitting function coefficients vary from mode to mode ($s \leq 2\ell$), and from source to source. Ritzwoller & Resovsky (1995) extended the maximum value to 12 in an attempt to provide a better constraint on the smaller-scale structure. However, only coefficients up to and including angular degree 6 will be considered in this study: higher degree data are not of sufficient number and quality.

So far, only isolated or self coupled modes have been discussed, but analyses of coupled modes exist (e.g., Resovsky & Ritzwoller, 1995, 1998; Kuo & Romanowicz, 2002). Coupled mode data give some sensitivity to odd degree structure, but the number of available coefficients are still limited. Although the mantle only inversion in Chapter 3 includes splitting function coefficients of coupled modes provided by Resovsky & Ritzwoller (1998), discussion will focus on even degree structure and isolated mode data.

Splitting Function Coefficients and Internal Structure

Because a splitting function is a radial average of internal structure, its coefficients are linearly related to perturbations in properties δm and topography δd by (Woodhouse & Dahlen, 1978; Dahlen & Tromp, 1998)

$$c_{st} = \int_0^a \sum_m \delta m \, K_s^m \, dr + \sum_d \delta d_{st} \, K_s^d, \tag{2.5}$$

where K_s^m and K_s^d denote the degree (s) dependent sensitivity kernel of a given mode to perturbations in m or undulation on a boundary d. These kernels are defined in terms of the eigenfunctions of the mode (Woodhouse, 1980; Li et al., 1991a) which are calculated using the reference one-dimensional model PREM (Dziewoński & Anderson, 1981). Examples of sensitivity kernels for mantle and inner core modes are shown in Figure 2.5. The first term on the right hand side of equation (2.5) is the volumetric contribution with an integration over radius from the center to the surface of the Earth with radius a. Therefore δm and K_s^m are both dependent on radius. The summation over m represents a sum over material properties, such as lateral variations in wave speed or anisotropy. The second term is a contribution from topography δd on various boundaries represented by a sum over these boundaries, e.g., the core-mantle boundary and Moho. The sensitivity kernel for undulations, K_s^d, tends to be small compared to K_s^m, and this term is often neglected (e.g., Giardini et al., 1987; Ritzwoller et al., 1988; Resovsky & Ritzwoller, 1999a; Masters at al., 2000b). The topography term is included in the mantle only inversion in Chapter 3, because free air gravity data are strongly sensitive to boundary undulations. Because the trade off between topography and density turns out to be not significant (Ishii & Tromp, 2001), the topography term is ignored in the inversions where only seismic data are included.

In studies of mantle structure, modes with no sensitivity to the inner core are often selected. With the assumption that the outer core is seismologically homogeneous (Stevenson, 1987), the integration in equation (2.5) becomes one from the core-mantle boundary with radius b to the surface a. In a seismic wave parametrisation, the equation becomes

$$c_{st} = \int_b^a \left[(\delta \upsilon_S/\upsilon_S)_{st} \, K_s^{\upsilon_S} + (\delta \upsilon_P/\upsilon_P)_{st} \, K_s^{\upsilon_P} + (\delta \rho/\rho)_{st} \, K_s^{\rho} \right] dr + \sum_d (\delta d/a)_{st} \, K_s^d. \tag{2.6}$$

Figure 2.3: Comparison of Splitting Function Coefficients at Degree 2

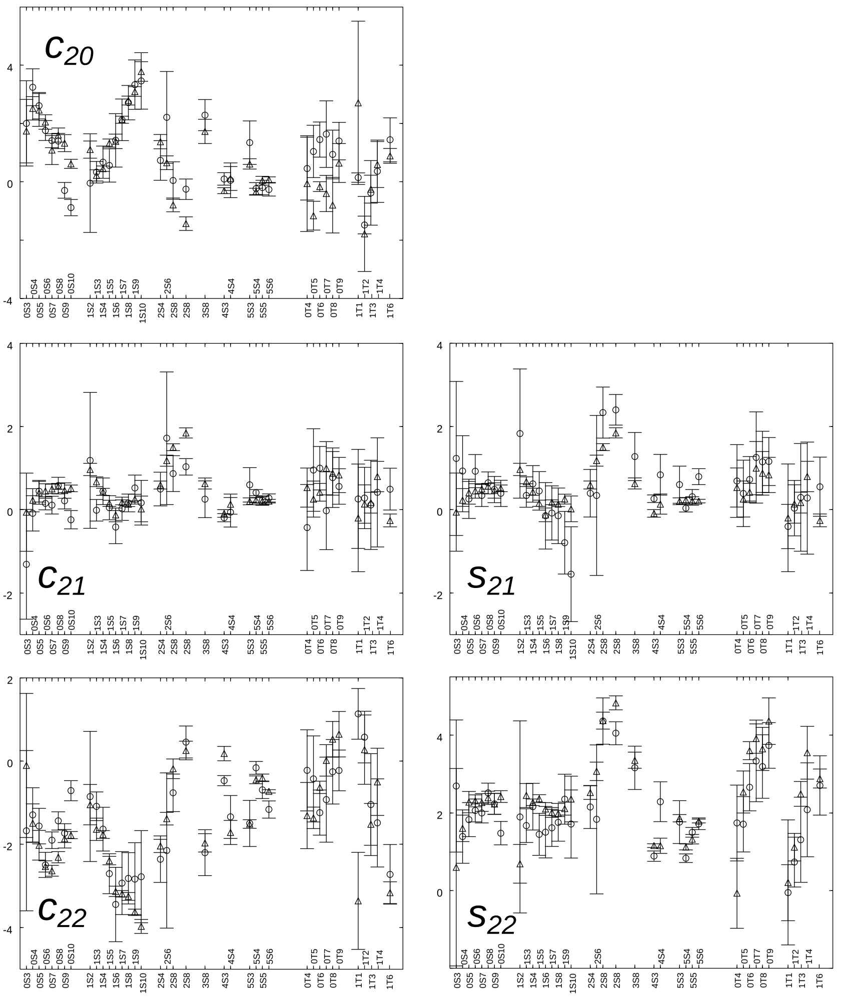

Comparison of degree 2 splitting function coefficients from two different groups. Those denoted by circles are measurements made by He & Tromp (1996) for spheroidal modes and by Tromp & Zanzerkia (1995) for toroidal modes. Measurements shown by triangles were made by Resovsky & Ritzwoller (1998). The coefficients are those of fully normalized spherical harmonics (Edmonds, 1960), *c* denotes the real part and *s* denotes the imaginary part; coefficients have been corrected for crustal structure using model Crust5.1 (Mooney et al., 1998).

Figure 2.4: Comparison of Splitting Function Coefficients at Degree 4

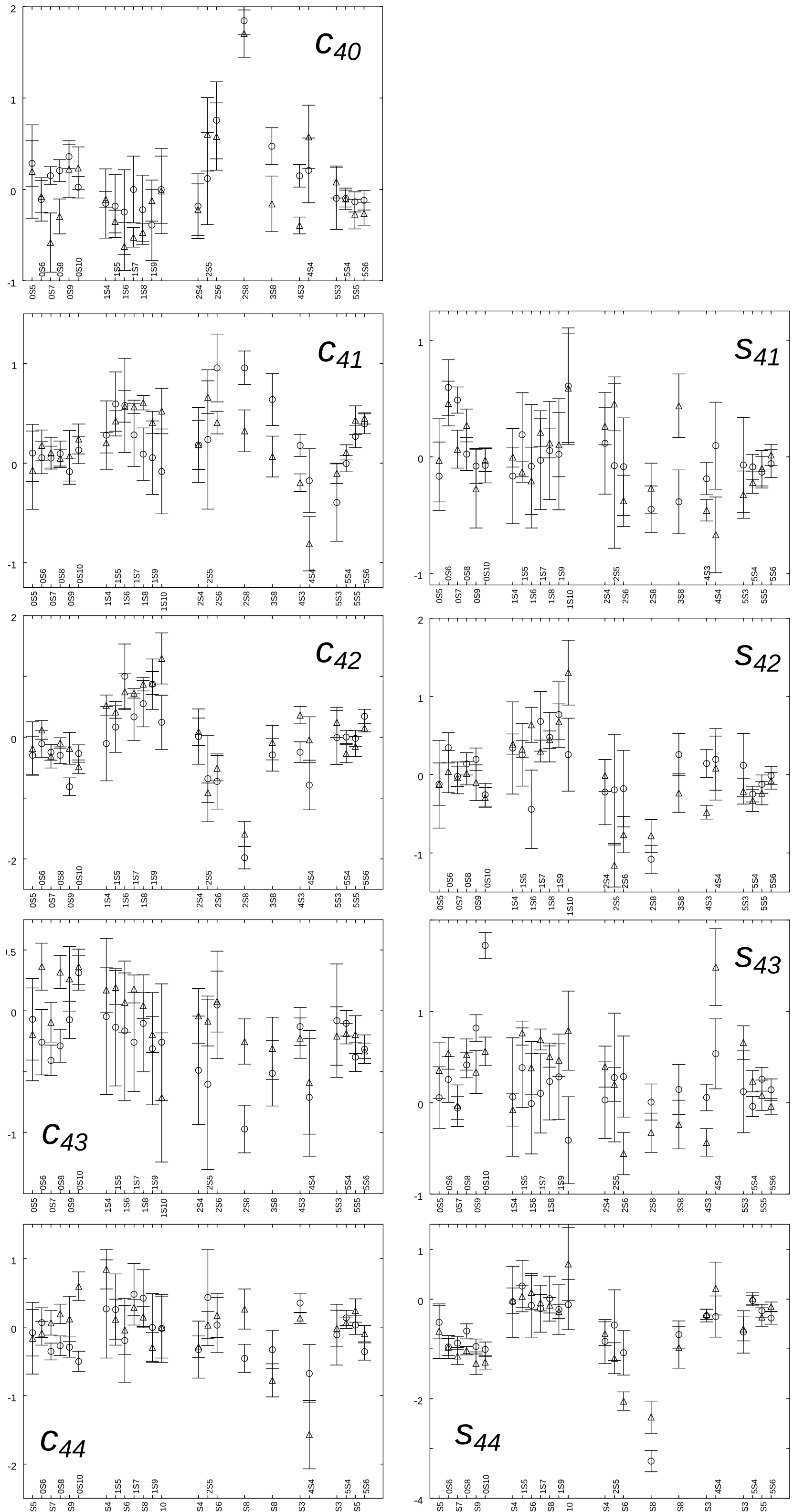

Figure 2.5: Normal Mode Sensitivity Kernels for Isotropic Variations

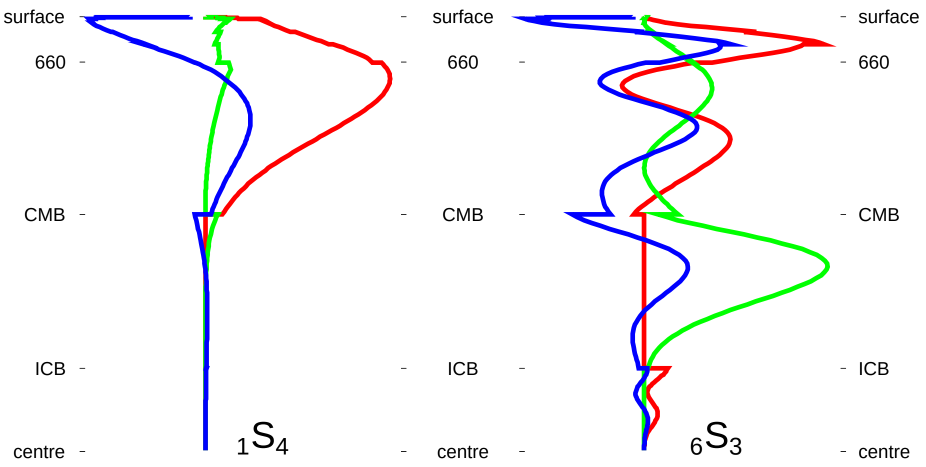

Sensitivity kernels (K_2) for isotropic variations in shear wave speed (red), compressional wave speed (blue) and density (green) for modes ${}_1S_4$, a mantle sensitive mode (left), and ${}_6S_3$, an inner core sensitive mode (right). Internal discontinuities, inner core boundary (ICB), core-mantle boundary (CMB), and 660-km discontinuity (660), are indicated.

The summation over discontinuities includes the free surface, the 410-km discontinuity, the 660-km discontinuity, and the core-mantle boundary. Initially, topography on the 410-km discontinuity was also included, but it was found to be not well resolved, presumably because it is dominated by degree 1 variation (Gu et al., 1998; Flanagan & Shearer, 1998). Therefore, a model of topographic variations on the 410-km discontinuity by Gu et al. (1998) is used to calculate a correction whenever topography is included in the inversion.

Equation (2.6) can also be written in terms of relative perturbations in the mineralogical parameters as

$$c_{st} = \int_b^a \left[(\delta\mu/\mu)_{st}\, K_s^\mu + (\delta\kappa/\kappa)_{st}\, K_s^\kappa + (\delta\rho/\rho)_{st}\, K_s^\rho\right] dr + \sum_d (\delta d/a)_{st}\, K_s^d, \tag{2.7}$$

or in terms of relative perturbations in shear wave speed, bulk sound speed, and density as

$$c_{st} = \int_b^a \left[(\delta\upsilon_S/\upsilon_S)_{st}\, K_s^{\upsilon_S} + (\delta\upsilon_\phi/\upsilon_\phi)_{st}\, K_s^{\upsilon_\phi} + (\delta\rho/\rho)_{st}\, K_s^\rho\right] dr + \sum_d (\delta d/a)_{st}\, K_s^d. \tag{2.8}$$

All three representations will be used in mantle modelling.

Most mode studies reduce the number of unknown parameters by neglecting the effects of boundary topography, and also by relating different parameters through scaling factors. For example, relative variations in density can be related to shear wave speed by a scaling factor ν_ρ, such that $\delta \ln \rho = \nu_\rho \delta \ln \upsilon_S$, and compressional and shear wave speed variations can be related by another scaling factor ν_α, $\delta \ln \upsilon_P = \nu_\alpha \delta \ln \upsilon_S$. These relationships are expected to exist if lateral variations in elastic properties are a result of temperature variations. The factors ν_ρ and ν_α can be constant or depth dependent, and are obtained from studies of minerals (e.g., Anderson et al., 1968; Karato, 1993a), comparison of compressional and shear wave data (e.g., Souriau & Woodhouse, 1985), or modelling of gravity data (e.g., Forte et al., 1994). Using these scaling relationships, equation (2.6)

Figure 2.6: Normal Mode Sensitivity Kernels for Transverse Isotropy

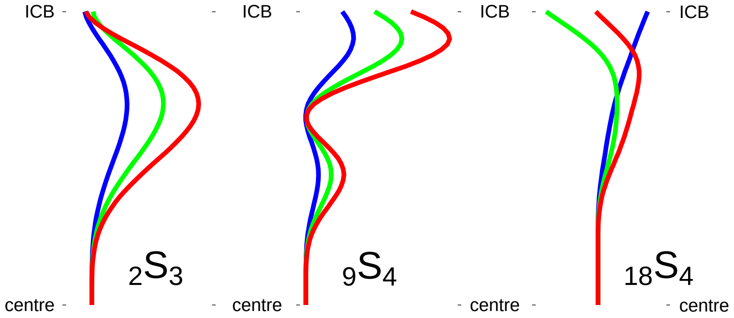

Examples of K_2^α (blue), K_2^β (red), and K_2^γ (green) for three inner core modes.

reduces to

$$c_{st} = \int_b^a \left[(\delta v_S/v_S)_{st}\; \mathcal{K}_s^{v_S}\right] dr, \tag{2.9}$$

where $\mathcal{K}_s^{v_S} = K_s^{v_S} + \nu_\alpha K_s^{v_P} + \nu_\rho K_s^\rho$. This approach has been used in early normal mode studies of shear wave speed variations within the mantle (Ritzwoller et al., 1988; Li et al., 1991a), and also recently by Resovsky & Ritzwoller (1999a). Alternatively, splitting coefficients can be inverted for shear wave structure and scaling factors (e.g., Li et al., 1991b).

For a data set consisting of both mantle and inner core modes, the contribution due to the inner core anisotropy cannot be neglected. Ignoring the topography term and representing variations in the mantle by $\delta m/m$, the splitting function coefficients relate to structure by

$$c_{st} = \int_b^a \left[(\delta m/m)_{st}\, K_s^m\right] dr \qquad \text{for} \quad t \neq 0 \quad \text{or} \quad s > 4, \tag{2.10}$$

and

$$c_{st} = \int_b^a \left[(\delta m/m)_{st}\, K_s^m\right] dr + \int_0^c \left(\alpha K_s^\alpha + \beta K_s^\beta + \gamma K_s^\gamma\right) dr \quad \text{for} \quad t = 0 \quad \text{and} \quad s = 0, 2, 4. \tag{2.11}$$

The parameter m represents v_S, v_P, and ρ, and α, β, and γ are depth dependent transversely isotropic parameters as defined in equation (2.1). The first term on the right hand side of equations (2.10) and (2.11) gives the contribution from the mantle, and the second term in equation (2.11) is the inner core contribution with integration from the center of the Earth to the inner core boundary c. The conditions of t and s associated with the two equations are due to cylindrical anisotropy with the symmetry axis aligned with the rotation axis: this type of anisotropy affects only the zonal splitting coefficients with angular degrees 0, 2, and 4 (Tromp, 1995b). Some examples of sensitivity kernels to transverse isotropy within the inner core are shown in Figure 2.6. Note that the sensitivity peak in the middle to top part of the inner core. Because sensitivity kernels are calculated using eigenfunctions, they must always vanish at the centre of the Earth.

Crustal Corrections

The crust, although very thin compared to the mantle, produces considerable splitting due to its strong heterogeneity, especially for surface wave equivalent modes. Therefore, before splitting coefficients are inverted for mantle or inner core structure, it is essential to remove the crustal contribution. This is achieved by predicting splitting due to crust using a crust model Crust5.1 (Mooney et al.,

Figure 2.7: EGM96

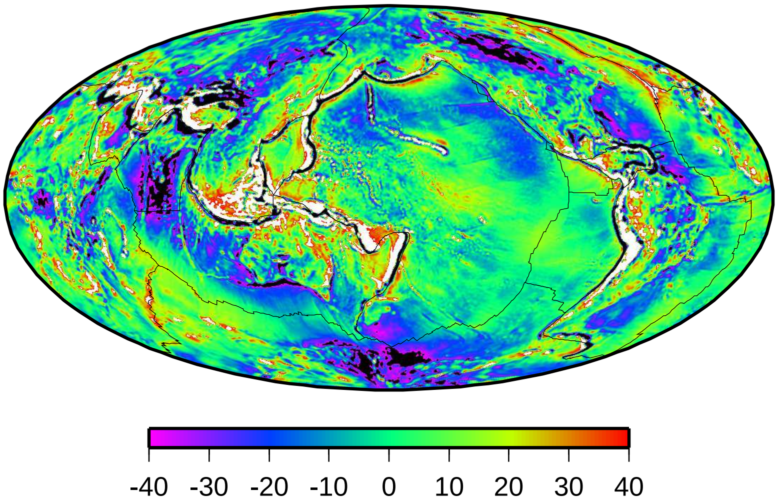

Geoid (deviations from gravitational equipotential surface) distribution obtained from the model EGM96 (Lemoine et al., 1997, 1998a,b). The scale is in meters.

1998) and the sensitivity of each mode between the Moho and the surface. Consequently, the integration for the mantle term, in equations relating splitting coefficients to the internal structure, is from the core-mantle boundary to the Moho discontinuity.

2.2.2 Free Air Gravity

To complement normal mode data in constraining the large-scale density variations within the mantle, free air gravity data are included in mantle only inversion data set. Free air gravity is the gravitational acceleration without surface topographic effects. This data is therefore sensitive to mantle density distribution as well as topography on internal boundaries.

Free Air Gravity Variation

Surface gravity data used in this study is obtained from the Earth Gravitational Model 1996 (EGM96, Lemoine et al., 1997, 1998a,b). This is a surface geopotential model expanded to spherical harmonic degree 360, which corresponds to $\sim$ 55 km resolution. It is developed by combined analysis of surface gravity data, satellite tracking data, and satellite altimetry measurements of the ocean surface (Lemoine et al., 1997). The geopotential model is shown in Figure 2.7. Although spherical harmonic coefficients are available up to degree 360, only those up to degree 6 are used in the inversion to be consistent with the mode data.

Free Air Gravity and Internal Structure

The perturbed gravitational potential, $\delta\Phi$, satisfies Poisson's equation

$$\nabla^2 \delta\Phi = 4\pi G\, \delta\rho,$$

where G is the gravitational constant and $\delta\rho$ denotes variations in density. Solving Poisson's equation, we obtain

$$\delta\Phi(\mathbf{r}) = -G \int_V \frac{\delta\rho(\mathbf{r}')}{|\mathbf{r}-\mathbf{r}'|}\, d^3\mathbf{r}' + G \sum_d \int_S \frac{[\rho]_-^+\, \delta d(\hat{\mathbf{r}}')}{|\mathbf{r}-\mathbf{r}'|}\, d^2\mathbf{r}',$$

where $\mathbf{r} = r\hat{\mathbf{r}}$ is the position vector, $[\rho]_-^+$ is the density jump at a discontinuity d, and δd is the topography on that discontinuity. Using the relationship (Forte & Peltier, 1987; Dahlen & Tromp, 1998)

$$\frac{1}{|\mathbf{r}-\mathbf{r}'|} = \sum_{s=0}^{\infty} \frac{4\pi}{2s+1} \frac{[\min(r,r')]^s}{[\max(r,r')]^{(s+1)}} \sum_{t=-s}^{s} Y_{st}(\hat{\mathbf{r}}) Y_{st}^*(\hat{\mathbf{r}}'),$$

and expanding $\delta\rho$, δd and $\delta\Phi$ in spherical harmonics as

$$\delta\rho(\mathbf{r}') = \sum_{s,t} \delta\rho_{st}(r') Y_{st}(\hat{\mathbf{r}}'), \quad \delta d(\hat{\mathbf{r}}') = \sum_{s,t} \delta d_{st}\, Y_{st}(\hat{\mathbf{r}}'), \quad \text{and} \quad \delta\Phi(\mathbf{r}') = \sum_{s,t} \delta\Phi_{st}(r') Y_{st}(\hat{\mathbf{r}}'),$$

the spherical harmonic coefficients of the gravitational potential at the surface a is related to density and topographic variations by

$$\delta\Phi_{st}(a) = -\frac{4\pi G}{2s+1} \int_b^a \delta\rho_{st}(r) \frac{r^s}{a^{s+1}}\, r^2 dr + \frac{4\pi G}{2s+1} \sum_d [\rho]_-^+ \frac{d^{s+2}}{a^{s+1}}\, \delta d_{st}\ .$$

In this study the free air gravity anomaly is used instead of the gravitational potential. The free air gravity anomaly coefficients f_{st} are related to the gravitational potential coefficients $\delta\Phi_{st}$ by

$$f_{st}(a) = -\frac{3g(s-1)}{4\pi a^2 G\bar{\rho}}\, \delta\Phi_{st}(a),$$

where g is the gravitational acceleration at the Earth's surface and $\bar{\rho}$ is the average density of the Earth. This relationship demonstrates the advantage in choosing the free air gravity over geopotential. The latter is dominated by spherical harmonic degree 2 component, but the free air gravity, due to $(s-1)$ factor, has a whiter spectrum.

The relationship between the gravity coefficients and the relative variations in density and boundary topography, is then, in a linear form much like for splitting function coefficients:

$$f_{st} = \int_b^a (\delta\rho/\rho)_{st}\, K_s^{'\rho}\, dr + \sum_d (\delta d/a)_{st}\, K_s^{'d}\ , \tag{2.12}$$

where $K_s^{'\rho}$ and $K_s^{'d}$ are the density and discontinuity sensitivity kernels of the free air gravity anomaly given, respectively, by

$$K_s^{'\rho} = -\frac{3g(s-1)}{2s+1} \left(\frac{\rho}{\bar{\rho}}\right) \left(\frac{r^s}{a^{s+1}}\right), \qquad \text{and} \qquad K_s^{'d} = \frac{3g(s-1)}{2s+1} \left[\frac{\rho}{\bar{\rho}}\right]_-^+ \left(\frac{d}{a}\right)^{s+2}.$$

The kernels at various degrees are illustrated in Figure 2.8. Note that as the angular degree increases, the sensitivity of the free air gravity coefficients are more concentrated near the surface.

The gravity modelling described above is based upon a static approach, and relates lateral variations in density and boundary topography directly with gravity variations observed at the surface. An alternative, more popular, approach is to consider the problem dynamically. Assuming that mantle convection driven by lateral density heterogeneity dictates the topographic variations, the topography term in equation (2.12) is replaced by a term involving density and viscosity of the mantle. With the introduction of viscosity, equation (2.12) is changed to a non-linear form. Such analyses of gravity field lead to models of radial viscosity profile (e.g., Hager & Clayton, 1989).

Figure 2.8: Free Air Gravity Sensitivity Kernels

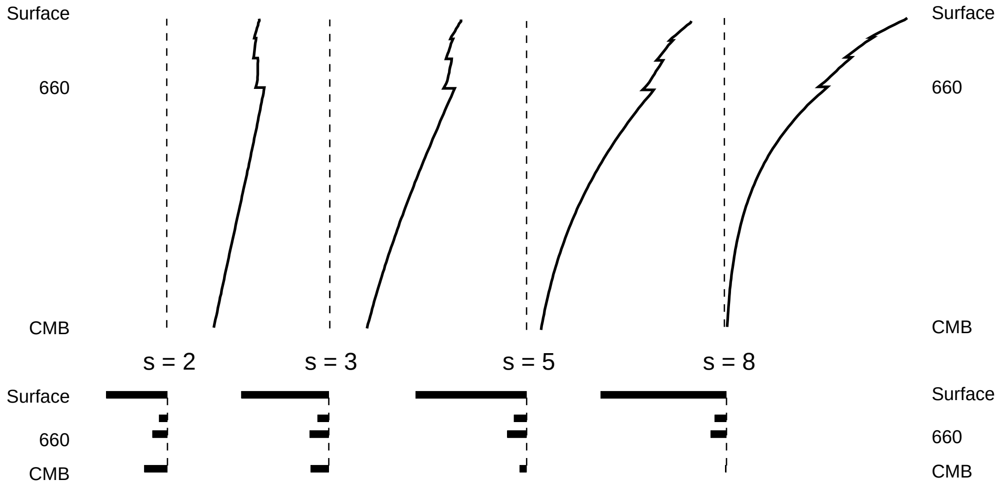

The sensitivity of free air gravity to variations in mantle density (top, solid curve) and topography (bottom, horizontal bars) on internal boundaries (free surface, 410-km and 660-km discontinuities, and core-mantle boundary) at various degrees *s*.

Corrections

The model EGM96 contains signals which are not a result of mantle structure; the effects due to crust and Earth's ellipticity. A hydrostatic correction based upon Nakiboglu (1982) is applied to gravity coefficients before they are analysed for mantle structure. The crust, on the other hand, is mostly in isostatic equilibrium and produces only a small contribution to the gravity field. In an early study of the joint inversion of normal mode and gravity data for mantle density heterogeneity, crustal effects on gravity has been ignored (Ishii & Tromp, 1999). Careful comparison of inversion results with and without the crustal correction to free air gravity confirmed that it is negligible, and its influence is within the uncertainty of the inversion process (Ishii & Tromp, 2001). No further correction, such as the effect due to lithosphere, is made to the free air gravity anomaly.

2.2.3 Body Wave Travel Times

In studying inner core anisotropy, travel times of compressional waves are included in the data set to complement the mode splitting data. The PKIKP phase, observed between 120° and 180° epicentral distance, is the only phase readily available for analysis of the inner core (Figure 2.9). This phase is also referred to as $\mathrm{PKP_{DF}}$, and along with other PKP phases, $\mathrm{PKP_{AB}}$, $\mathrm{PKP_{BC}}$, and $\mathrm{PKP_{CD}}$, define the PKP branch. $\mathrm{PKP_{CD}}$, also called PKiKP, is a ray that is reflected at the inner core boundary, and because it is not analysed in later Chapters, its discussion is omitted. $\mathrm{PKP_{BC}}$ and $\mathrm{PKP_{AB}}$ turn in the lower and upper parts of the outer core, respectively, and do not sample the inner core. In the inner core study, deviations of arrival times of PKP phases from those predicted by a radial model are interpreted as due to transverse isotropy. In the following sections, the relationship between the travel time residuals and transverse isotropy is described in detail, followed by a discussion on two types of travel time data.

Figure 2.9: Geometry and Travel Times of the PKP Branch

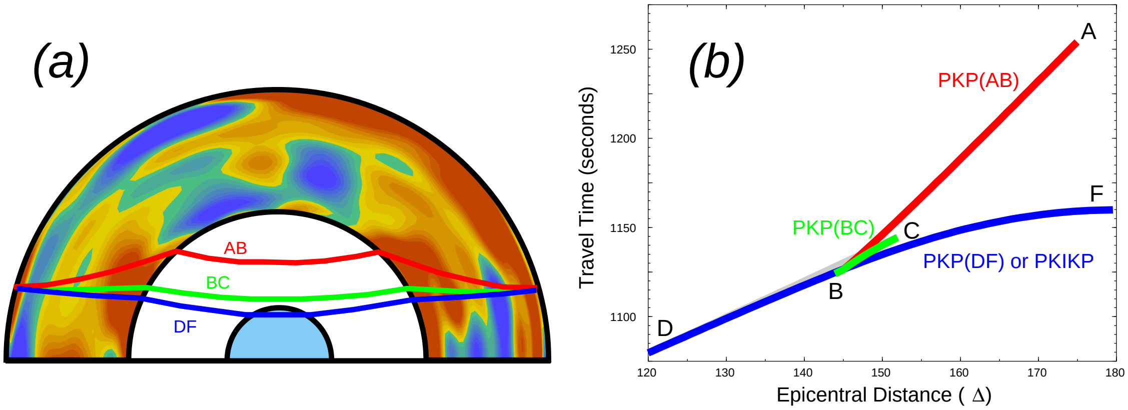

(a) Cross section of the Earth with ray paths for $\mathrm{PKP_{AB}}$ (red), $\mathrm{PKP_{BC}}$ (green), and $\mathrm{PKP_{DF}}$ or PKIKP (blue) at an epicentral distance of 150° and based upon PREM (Dziewoński & Anderson, 1981). The mantle is illustrated with a shear wave heterogeneity model of Gu et al. (2001) with red and colours for slower and faster than average speeds, respectively. The cross section is along a great circle between Africa (left) and the southwestern Pacific (right), crossing under Eurasia. The outer core is shown by the white region, and the inner core is indicated by pale blue.
(b) A travel time table for PKP branch based upon PREM and an earthquake with a source depth of 300 km.

Figure 2.10: Geometry of the $\mathrm{PKP_{DF}}$ in the Inner Core

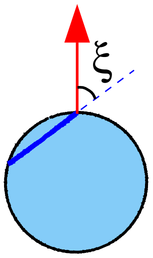

A section of $\mathrm{PKP_{DF}}$ ray path (blue) within the inner core (pale blue). Note that the $\mathrm{PKP_{DF}}$ path is practically a straight line, supporting the assumption used in the travel time calculation. The angle this ray makes with the symmetry axis (arrow in red) is the ray angle ξ. At high values of $\cos^2\xi$, the ray is travelling parallel to the symmetry axis, and at small values of $\cos^2\xi$, the ray is travelling perpendicular to the symmetry axis.

Effects due to Transverse Isotropy

The relationship between seismic wave speed and the elastic tensor is given by the Christoffel equation

$$\rho\upsilon^2 = \hat{\mathbf{k}}\hat{\mathbf{p}} : \Lambda : \hat{\mathbf{k}}\hat{\mathbf{p}}, \tag{2.13}$$

where υ is the speed of body waves, and unit vectors $\hat{\mathbf{k}}$ and $\hat{\mathbf{p}}$ give the direction of propagation and polarisation of the wave, respectively. For a material with cylindrical symmetry, equation (2.13) gives (Backus, 1965; Crampin, 1977)

$$\rho\upsilon_P^2 = A - 2(A - F - 2L)\cos^2\xi + (A + C - 2F - 4L)\cos^4\xi,$$

where ξ is the angle between the direction of wave propagation and the symmetry axis (Figure 2.10). For weak anisotropy, $\rho\upsilon_P^2$ can be written in terms of a reference value $\rho\upsilon_r^2$ and a small perturbation due to anisotropy $\rho\,\delta\upsilon_P^2$. Letting $\rho\upsilon_r^2 = A$, then

$$2\rho\upsilon_P^2\delta\upsilon_P/\upsilon_P = -2(A - F - 2L)\cos^2\xi + (A + C - 2F - 4L)\cos^4\xi. \tag{2.14}$$

Note that equation (2.14) includes terms involving A and F associated with compressional waves, but also the parameter L which is related to shear waves travelling parallel to the symmetry axis. This equation can be written in terms of associated Legendre functions P_s^t such that

$$2\rho\upsilon_P^2\delta\upsilon_P/\upsilon_P = \frac{4}{21}(-4A + F + 2L + 3C)P_2^0(\cos\xi) + \frac{8}{35}(A + C - 2F - 4L)P_4^0(\cos\xi),$$

which illustrates why only zonal splitting function coefficients at degrees 2 and 4 are sensitive to transverse isotropy with a symmetry axis in the z-direction.

Using equation (2.2), perturbations in compressional wave speed is written

$$\delta\,\upsilon_P/\upsilon_P = \epsilon\,\cos^2\xi + \sigma\,\sin^2\xi\,\cos^2\xi + \eta_0, \tag{2.15}$$

where the term η_0 is introduced to account for inadequacy of the reference inner core model (the assumption that $\rho\upsilon_r^2 = A$). It also arises from uncertainties in the one-dimensional models outside the inner core such as the mantle and the crust. Because the values of η_0 may contain effects other than inner core anisotropy, this parameter is ignored in discussion even though it is included as an inversion parameter.

Using trigonometry, equation (2.15) can be written in variety of ways. For example,

$$\delta\, \upsilon_P/\upsilon_P = (\epsilon + \sigma)\, \cos^2 \xi - \sigma\, \cos^4 \xi + \eta_0, \tag{2.16}$$

which is convenient when plotting travel time residuals as a function of $\cos^2 \xi$, or

$$\delta\, \upsilon_P/\upsilon_P = \frac{1}{2}\,(\epsilon + 2\,\sigma)\, \cos(2\xi) - \frac{1}{8}\,\sigma\, \cos(4\xi) + \eta_1, \tag{2.17}$$

which may be appealing when comparing results with parameters of azimuthally anisotropic materials. Note that in equation (2.17), the baseline shift includes contributions from both ϵ and σ, i.e.,

$$\eta_1 = \eta_0 - \frac{1}{2}\,\epsilon - \frac{1}{8}\,\sigma.$$

Travel time anomalies δt are related to small perturbations in compressional wave speed by

$$\delta t = -\int_s \frac{\delta \upsilon_P}{\upsilon_P^2}\, ds, \tag{2.18}$$

where s is the ray path. It is assumed to be a straight line within the inner core, because compressional wave speed varies only slightly with radius in the reference model (Figure 2.10). Combining equations (2.17) and (2.18), δt depends linearly upon ϵ, σ, and η_0 as

$$\delta\, t\,(\cos^2 \xi) = -\cos^2 \xi \int_s (\epsilon + \sigma)\, \frac{1}{\upsilon_P}\, ds + \cos^4 \xi \int_s \sigma\, \frac{1}{\upsilon_P}\, ds - \int_s \eta_0\, \frac{1}{\upsilon_P}\, ds. \tag{2.19}$$

Travel Times as a Function of Two Variables

Instead of averaging only by values of $\cos^2 \xi$, travel times can be grouped by their ray angle ξ and another variable ϕ (e.g., bottoming longitude). Such averaging is desirable when investigating if the material is transversely isotropic or when determining the location of the symmetry axis. Using equations (2.16) and (2.18), and writing $\cos^2 \xi$ and $\cos^4 \xi$ in spherical harmonics,

$$\begin{aligned} \delta\, t\,(\xi, \phi) \quad = \quad & \left\{ -\int_s \frac{1}{V} \left[\frac{4}{21} \sqrt{\frac{\pi}{5}}\, (7\,\epsilon + \sigma) \right] ds \right\} Y_2^0\,(\xi, \phi) + \left[\int_s \frac{1}{V} \left(\frac{16\,\sqrt{\pi}}{105}\, \sigma \right) ds \right] Y_4^0\,(\xi, \phi) \\ & + \left\{ -\int_s \frac{1}{V} \left[2\,\sqrt{\pi} \left(\gamma_0 + \frac{1}{3}\,\epsilon + \frac{2}{15}\,\sigma \right) \right] ds \right\} Y_0^0\,(\xi, \phi). \end{aligned} \tag{2.20}$$

This equation illustrates that the travel time distribution, plotted with colatitude ξ and east-longitude ϕ, must be purely zonal if the inner core is transversely isotropic. Data distribution in the ξ-ϕ space therefore tests whether the data are consistent with transversely isotropic material. Two different parameters for ϕ are considered in this study, bottoming longitude ϕ_b and translated surface intercept longitude ϕ_c. The former parametrisation is appropriate for verifying whether the material has a transversely isotropic property, and the latter is suited for the search of the symmetry axis.

For averaging data on the ξ-ϕ unit sphere, it is divided into 362 nearly equal area triangles by triangular tessellation (Wang & Dahlen, 1995) whose nodes are used as the centres of 10° caps (Figure 2.11). These caps are advantageous in that they are nearly equally spaced. On the other hand, node distribution is not symmetric across the equator, implying that even when data are symmetric, the cap averages may exhibit a pattern that is slightly different between the northern and southern hemispheres. This definition of caps imply that data are smoothed considerably, because the cap size (10° radius) is almost equivalent to the distance between nodes (11°). Nonetheless, this smoothing preserves variations at spherical harmonic degree 10 or less. Since signals of interest are at degrees 0, 2, and 4 (equation 2.20), cap overlap and subsequent smoothing do not prejudice the investigation. Caps with less than 3 measurements are excluded.

Figure 2.11: Centres of 362 Caps

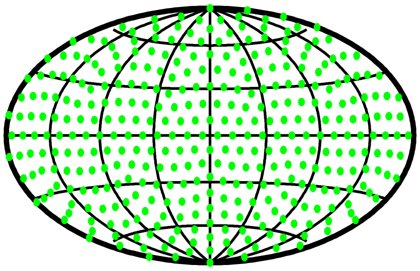

Nodes of triangular tessellation (green circles) with frequency 6 that are used as the centres of 10° caps for averaging data in the ξ-ϕ space.

Absolute Travel Times

The arrival time of the $\mathrm{PKP_{DF}}$ can be measured and used for an investigation of the inner core. This type of data are called absolute travel times. The absolute travel time data used in this study were collected by the International Seismological Centre (ISC) between 1964 and 1996. Observations range from the epicentral distances between 120° and 180°, but between 140° and 150°, the arrival of precursors (140° to 145°) and $\mathrm{PKP_{BC}}$ (145° to 150°) are often mis-identified as the arrival of $\mathrm{PKP_{DF}}$ (e.g., Shearer, 1994). This results from the proximity of the $\mathrm{PKP_{BC}}$ branch to $\mathrm{PKP_{DF}}$ (Figure 2.9), and also from larger amplitude of the precursors and $\mathrm{PKP_{BC}}$ compared to $\mathrm{PKP_{DF}}$. Without these dubious data, the ISC data set consists of ~ 325000 measurements in the distance ranges 120°–140° and 150°–180°.

The $\mathrm{PKP_{DF}}$ arrival time is influenced by many factors, since it travels to and from the surface through various regions of the Earth (Figure 2.9). To extract the signal due to the inner core, the ISC data are corrected for the Earth's ellipticity (Dziewoński & Gilbert, 1976), crust, mantle, and earthquake locations. The mantle contribution is calculated using a degree 12 compressional wave speed model (Su & Dziewoński, 1993), and the earthquakes are relocated using arrival times of P, S, $\mathrm{PKP_{DF}}$, $\mathrm{PKP_{BC}}$, and $\mathrm{PKP_{AB}}$, in conjunction with the compressional wave model and a shear wave speed model (Su et al., 1994).

The disadvantage of the ISC data set is its poor quality. The travel time picks are made by different station operators, resulting in a considerable range in the reported arrival times. Treatment of large travel time values (those with more than two standard deviations away) produce models of the inner core with significant differences (e.g., Shearer et al., 1988; Shearer, 1994). Following Su & Dziewoński (1995), a weight, w, is assigned to each travel time residual δt such that

$$w = 1.0 \qquad \text{for} \qquad |\delta t| \leq 5\,;$$

$$w = \exp\left[1 - 0.04(\delta t)^2\right] \qquad \text{for} \qquad 5 < |\delta t| \leq 10\,; \quad \text{and}$$

$$w = 0.0 \qquad \text{for} \qquad |\delta t| > 10\,.$$

In addition, data are averaged to overcome individual quality problem. The data are first divided into eight epicentral distance ranges: 120°–130°, 130°–140°, 150°–153°, 155°–160°, 160°–165°, 165°–173°, and 173°–180°. Each range is chosen by considering the balance between the number of measurements and the size of the range. Within a given distance range, the data are then averaged according to their ray angle ξ, in bins of 0.1 in $\cos^2\xi$. The number of data in each bin is plotted for the eight epicentral distances in Figure 2.12.

Figure 2.12: Number of the ISC Data for each Average

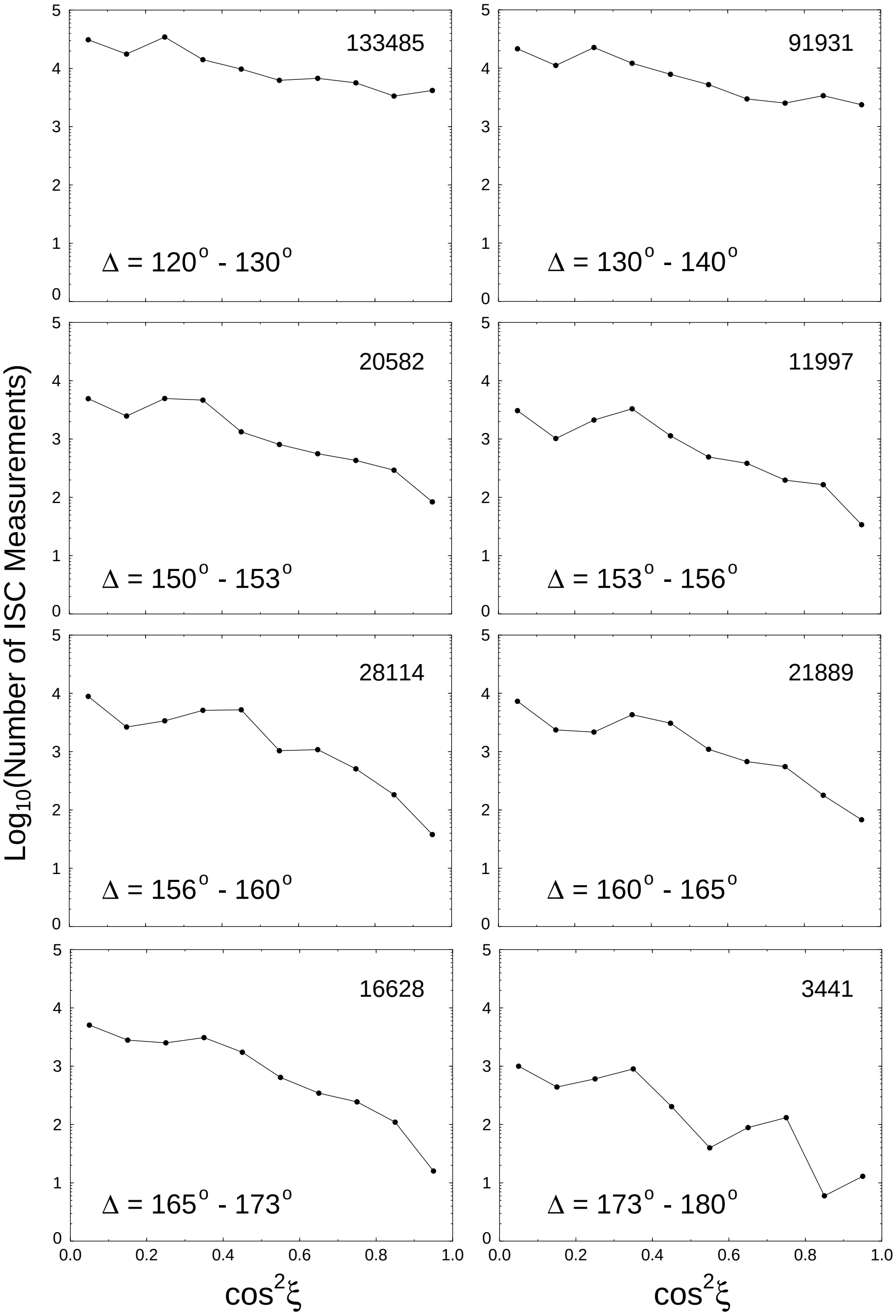

Logarithm of the number of each average obtained from the ISC data set is plotted against $\cos^2\xi$ for the eight distance ranges. The number at the top right corner of each panel is the total number of data in that distance range.

Differential Travel Times

Most of the inner core studies analyse the differential travel times rather than the absolute travel times. The differential travel times are obtained by differencing the arrival times of $\mathrm{PKP_{BC}}$ or $\mathrm{PKP_{AB}}$ and $\mathrm{PKP_{DF}}$. The advantage in using $\mathrm{PKP_{BC}}-\mathrm{PKP_{DF}}$ or $\mathrm{PKP_{AB}}-\mathrm{PKP_{DF}}$ comes from the similarity in the ray paths (Figure 2.9): effects due to earthquake location, crust, and mantle are significantly reduced. In fact, in differential travel time studies of the inner core, data are assumed to contain signals only due to the inner core.

The differential travel times can be obtained from reports of $\mathrm{PKP_{DF}}$, $\mathrm{PKP_{AB}}$, and $\mathrm{PKP_{BC}}$ arrivals from the ISC Bulletin, but simultaneous reports of the three phases are rare and often unreliable. Instead, the differential travel times are determined through careful waveform analysis (correlating $\mathrm{PKP_{DF}}$ waveform with that of $\mathrm{PKP_{BC}}$ and $\mathrm{PKP_{AB}}$). The resulting data are of high quality, but are limited in number. The differential travel time data set used in this study has been compiled by Creager (1999, 2000) from measurements made by various researchers. This data set uses the relocated earthquake catalogue of Engdahl et al. (1998), and the data are corrected for ellipticity (Dziewoński & Gilbert, 1976). The predicted differential travel time based upon PREM is also removed to enhance the travel time anomaly originating in the inner core.

There are 851 $\mathrm{PKP_{BC}}-\mathrm{PKP_{DF}}$ measurements taken collected from studies by Creager (1992), McSweeney (1995), Creager (1997), McSweeney et al. (1997), Tanaka & Hamaguchi (1997), and Creager (1999). The data come from earthquakes between 1965 and 1995, and cover a distance range from 145° to 160°. $\mathrm{PKP_{BC}}-\mathrm{PKP_{DF}}$ data with an epicentral distance greater than $\sim 153°$ use diffracted $\mathrm{PKP_{BC}}$ rays ($\mathrm{PKP_{BC}^{diff}}$), travelling along the inner core boundary. These data involving the diffracted $\mathrm{PKP_{BC}}$ are removed from the differential travel time database, which reduces the number of $\mathrm{PKP_{BC}}-\mathrm{PKP_{DF}}$ data to 512. $\mathrm{PKP_{BC}^{diff}}-\mathrm{PKP_{DF}}$ data are treated separately, and used only in an argument for anisotropy near the inner core boundary. To follow the averaging scheme for the absolute travel times, the remaining $\mathrm{PKP_{BC}}-\mathrm{PKP_{DF}}$ are grouped into 2 distance ranges, 145° to 150°, and 150° to 153°, and averaged for each 0.1 increment in $\cos^2\xi$. Note that $\mathrm{PKP_{BC}}-\mathrm{PKP_{DF}}$ data provide information between 145° and 150° that is not available with the absolute travel times. The narrow distance range of $\mathrm{PKP_{BC}}-\mathrm{PKP_{DF}}$ observations, however, implies that the data are only sensitive to the upper few hundred kilometers of the inner core. To extend the sensitivity, $\mathrm{PKP_{AB}}-\mathrm{PKP_{DF}}$ data are introduced.

There are 967 $\mathrm{PKP_{AB}}-\mathrm{PKP_{DF}}$ measurements from five studies that span a distance range from 149° to 177° (Vinnik et al., 1994; McSweeney, 1995; Song, 1996; McSweeney et al., 1997; Creager, 1999). $\mathrm{PKP_{AB}}$ rays propagating along the core-mantle boundary, instead of diving into the outer core (i.e., diffracted $\mathrm{PKP_{AB}}$), are excluded from the database, reducing the number of data to 963. These $\mathrm{PKP_{AB}}-\mathrm{PKP_{DF}}$ measurements are divided into 4 distance range groups, 149° to 153°, 153° to 160°, 160° to 165°, and 165° to 180°. $\mathrm{PKP_{AB}}-\mathrm{PKP_{DF}}$ observations at large epicentral distances allow modelling of the inner core to the centre of the Earth. However, the two ray paths differ significantly within the mantle, especially as the epicentral distance increases. The $\mathrm{PKP_{AB}}$ path traverses the lower-most mantle at a very shallow angle, and therefore is very sensitive to the strong heterogeneity known to exist in this region (e.g., Julian & Sengupta, 1973; Dziewoński, 1984; Bréger et al., 2000; Ritsema et al., 1998). In fact, there are studies of the D" region using $\mathrm{PKP_{AB}}-\mathrm{PKP_{DF}}$ explaining much of the signal without consideration of the inner core (e.g., Song & Helmberger, 1997; Tkalčić et al., 2002). Because of the possible contamination by mantle heterogeneity, the $\mathrm{PKP_{AB}}-\mathrm{PKP_{DF}}$ data are down-weighted compared to $\mathrm{PKP_{BC}}-\mathrm{PKP_{DF}}$ or $\mathrm{PKP_{DF}}$ data in inversions.

Advantages and disadvantages of PKP data are summarised in Table 2.2 along with those for the normal mode data.

Table 2.2: Comparison of Inner Core Data

Data	Advantages	Disadvantages
Normal Mode	• global sampling	• poor depth resolution • not sensitive to the central inner core • includes effects from crust/mantle • only for large-scale variations
$\mathrm{PKP_{DF}}$	• numerous measurements → good coverage • constrains the entire inner core	• poor quality • includes signal from structures outside the inner core
$\mathrm{PKP_{BC}}-\mathrm{PKP_{DF}}$	• high quality • free from crust, mantle, & earthquake location effects (?)	• limited number → laterally biased sampling • constrains only shallow inner core
$\mathrm{PKP_{AB}}-\mathrm{PKP_{DF}}$	• high quality • free from crust, mantle, & location effects (?) • constrains the entire inner core	• limited number • contamination from mantle

Summary of advantages and disadvantages associated with different data types used in inner core modelling.

2.3 The Linear Inverse Problem

A radially dependent model δm can be expanded with radial basis functions $B_k(r)$ as

$$\delta m(r) = \sum_{k=0}^{k_{max}} \delta m^k \, B_k(r).$$

For example, mantle shear wave variation coefficients $(\delta v_S/v_S)_{st}$ and inner core anisotropy parameter α are expressed, respectively, as

$$(\delta v_S/v_S)_{st} = \sum_{k=0}^{k_{max}} (\delta v_S/v_S)^k_{st} \, B^M_k(r), \qquad \text{and} \qquad \alpha = \sum_{p=0}^{p_{max}} \alpha^p \, B^I_p(r),$$

where superscripts M and I on the basis functions identify different basis functions used for mantle and inner core. Using these representations, the model coefficients, e.g., $(\delta v_S/v_S)^k_{st}$, can be taken out of the integration over radius or ray path. The linear relationship between splitting coefficients, free air gravity anomaly, or travel times and internal structure can then be written in matrix notation as

$$\mathsf{d} = \mathsf{K}\mathsf{m}.$$

The vectors d and m contain data and model parameters, respectively, and the matrix K relates the two vectors based upon the sensitivity kernels.

For mantle only inversion, the model vector contain lateral variations in elastic parameters, density, and topography such that

$$\mathsf{m} = \left[\ (\delta v_S/v_S)^k_{st} \ \ (\delta v_P/v_P)^k_{st} \ \ (\delta\rho/\rho)^k_{st} \ \ (\delta d/a)_{st}\ \right]^{\mathsf{T}},$$

where T denotes the transpose. The dimension of this vector M is determined by the maximum radial expansion and spherical harmonic degrees considered (note that there are $2s+1$ independent angular orders for a given degree s). The data vector d includes splitting and free air gravity coefficients at various values of s and t as well as from different normal modes so that

$$\mathsf{d} = \left[\ {}_nc_{st}\quad f_{st}\ \right]^{\mathsf{T}},$$

where the subscript n is used as a mode label. This is an N-dimensional vector where the value N is the sum of the number of splitting function coefficients and free air gravity coefficients in the database. The two vectors m and d are related by an $N \times M$-dimensional matrix

$$\mathsf{K} = \begin{bmatrix} {}^n_kK_s^{v_S} & {}^n_kK_s^{v_P} & {}^n_kK_s^{\rho} & {}^nK_s^{d} \\ 0 & 0 & {}_kK_s'^{\rho} & K_s'^{d} \end{bmatrix},$$

where the subscript k indicates that the element is obtained from integration of the product between radial basis function and the sensitivity kernel. The model parameters may be changed or combined as discussed in section 2.1.1. When the model vector does not include density and topography variations, the free air gravity coefficients are removed from the database.

The vectors and matrix are similar for simultaneous inversion of mantle and inner core structure. Expressing three volumetric perturbations of the mantle as $\delta m/m$,

$$\mathsf{m} = \left[\ (\delta m/m)^k_{st}\quad \alpha_p\quad \beta_p\quad \gamma_p\ \right]^{\mathsf{T}}.$$

The data vector includes travel time data instead of gravity anomaly

$$\mathsf{d} = \left[\ {}_nc_{st}\quad \delta t_q\ \right]^{\mathsf{T}},$$

where the subscript q identifies the each travel time datum. The sensitivity kernel K takes the form

$$\mathsf{K} = \begin{bmatrix} {}^n_kK_s^{m} & {}^n_pK_s^{\alpha} & {}^n_pK_s^{\beta} & {}^n_pK_s^{\gamma} \\ 0 & {}^q_pK^{\alpha} & {}^q_pK^{\beta} & {}^q_pK^{\gamma} \end{bmatrix}.$$

The second row of K describes how δt_q is related to α, β, and γ, although the three parameters are not linearly independent for these data.

The model vector is obtained by minimising the objective function

$$f(\mathsf{m}) = [\mathsf{d} - \mathsf{Km}]^{\mathsf{T}}\,\mathsf{W}\,[\mathsf{d} - \mathsf{Km}] + [\mathsf{m} - \mathsf{m}_0]^{\mathsf{T}}\,\mathsf{D}\,[\mathsf{m} - \mathsf{m}_0],$$

where W is a diagonal matrix with dimensions $N \times N$ that assigns a weighting to each datum, D is an $M \times M$ damping matrix, and m_0 is an M-dimensional starting model vector. The damping matrix D determines the degree to which the model vector m is forced towards the starting model m_0. A combination of norm, first, and second derivative damping is used to define elements of the matrix D. A particular set of values is chosen such that the resulting model provides high variance reduction with least amount of damping.

The diagonal elements of the data weighting matrix W are given by ω/σ_i^2, where σ_i is the estimated uncertainty of each datum d_i, and ω describes the relative weights assigned to differing types of data. The values of σ_i for mode splitting coefficients are obtained from estimates of uncertainty given by individual studies, some of which are illustrated as error bars in Figure 2.3. The free air gravity coefficients are given a constant uncertainty, because they are expected to have similar precision at low degrees considered in this study. Because average travel times are used in inversion instead of individual measurements for both absolute and differential travel times, the standard deviations of the mean are used as error estimates. The prescribed values of ω dictates the importance of one type of data with respect to mode splitting data set. So $\omega = 1$ for splitting coefficients with different values assigned to the free air gravity, $\mathrm{PKP_{DF}}$, $\mathrm{PKP_{BC}}-\mathrm{PKP_{DF}}$, and $\mathrm{PKP_{AB}}-\mathrm{PKP_{DF}}$ data sets. The values of ω for each data set is determined by a balance between the fit to mode data and the fit to non-modal data, and in some cases, it is varied to explore the effects on the inversion results.

To take advantage of models based mainly upon travel time and waveform data, such models are used as starting models, defining m_0. The choice of models is shear wave speed model SKS12WM13 (Dziewoński et al., 1997), compressional wave model P16B30 (Bolton, 1996), and the 660-km discontinuity model of Gu et al. (1998). A density starting model is either zero or SKS12WM13 scaled by a factor of 0.2, and the free surface has zero starting topography. The topography of the starting core-mantle boundary is zero except for the excess ellipticity determined by Very Long Baseline Interferometry (Gwinn et al., 1986). Because there is a considerable variation between models of inner core anisotropy (e.g., Shearer & Toy, 1991; Song & Helmberger, 1993; Tromp, 1993), no starting model is included for model parameters of the inner core.

Minimising the objective function, the model vector becomes

$$\mathsf{m} = \left(\mathsf{K}^\mathsf{T}\mathsf{W}\mathsf{K} + \mathsf{D}\right)^{-1}\left(\mathsf{K}^\mathsf{T}\mathsf{W}\mathsf{d} + \mathsf{D}\mathsf{m}_0\right). \tag{2.21}$$

Neglecting the starting model term, and replacing data vector with $\mathsf{K}\mathsf{m}^{true}$, there is a relationship between a model obtained from the inversion m and the true model m^{true},

$$\mathsf{m} = \left(\mathsf{K}^\mathsf{T}\mathsf{W}\mathsf{K} + \mathsf{D}\right)^{-1}\mathsf{K}^\mathsf{T}\mathsf{W}\mathsf{K}\,\mathsf{m}^{true}.$$

The matrix relating m and m^{true}, $\mathsf{R} = \left(\mathsf{K}^\mathsf{T}\mathsf{W}\mathsf{K} + \mathsf{D}\right)^{-1}\mathsf{K}^\mathsf{T}\mathsf{W}\mathsf{K}$ is called the resolution matrix. In an ideal case, the resolution matrix is the identity matrix, but introduction of damping causes the resolution matrix to deviate from it. Analysis of the resolution matrix provides an insight into the effects of damping, especially in terms of the trade offs between different parameters (e.g., between shear wave and density variations). The trace of this matrix represents the number of resolved parameters, and is an useful indicator of model reliability.

The covariance matrix for the model parameters is given by (Menke, 1989)

$$\mathsf{C} = \left(\mathsf{K}^\mathsf{T}\mathsf{W}\mathsf{K} + \mathsf{D}\right)^{-1}\mathsf{K}^\mathsf{T}\mathsf{W}\mathsf{K}\left(\mathsf{K}^\mathsf{T}\mathsf{W}\mathsf{K} + \mathsf{D}\right)^{-1}. \tag{2.22}$$

The square root of a diagonal element of the covariance matrix $\sqrt{C_{ii}}$ defines the standard error associated with the ith model parameter m_i. However, in a damped least squares inversion, the uncertainty associated with the model parameters is highly dependent upon the damping matrix D and may not provide a realistic error estimate. For example, strongly damped parameters, i.e., parameters for which the corresponding elements in the damping matrix is large, are confined to a small portion of the model space. These parameters cannot vary much from their starting values, and hence the uncertainty calculated from the covariance matrix is very small. This does not mean that these parameters are well constrained. Actually, they are given strong *a priori* damping, because there are reasons to believe that these parameters cannot be modelled reliably with the available data set.

Chapter 3

Mantle Heterogeneity

3.1 Introduction

Collection of seismic data at global stations by International Seismological Centre (ISC) began in the 1960's. They provided information needed for mapping lateral variations within the mantle. The first seismic tomography of the mantle was thus developed (Dziewoński, 1975), and the impact of the tomographic model on Earth's dynamics was quickly recognised (Dziewoński et al., 1977; Hager et al., 1985). The initial model showed compressional wave speed heterogeneities within the lower mantle (Dziewoński, 1975,1984), but this was soon followed by development of shear wave variations (Woodhouse & Dziewoński, 1984; Nataf et al., 1986).

Because these tomographic models have significant implications and applications to the Earth Science community, and because high quality and quantity data become available with time, generation of whole mantle tomographic models is now a standard practice. There are numerous models of compressional wave speed (e.g., Inoue et al., 1990; Pulliam et al., 1993; Bolton, 1996; Robertson & Woodhouse, 1996; Zhou, 1996; Su & Dziewoński, 1997; van der Hilst et al., 1997; Bijwaard et al., 1998; Vasco & Johnson, 1998; Boschi & Dziewoński, 1999; Kárason & van der Hilst, 2001; Antolik et al., 2003) and shear wave speed (e.g., Ritzwoller et al., 1988; Li et al., 1991a; Zhang & Tanimoto, 1993; Forte et al., 1994; Su et al., 1994; Li & Romanowicz, 1996; Masters et al., 1996; Robertson & Woodhouse, 1996; Grand et al., 1997; Kennett et al., 1998; Liu & Dziewoński, 1998; Vasco & Johnson, 1998; Ishii & Tromp, 1999; Resovsky & Ritzwoller, 1999a; Mégnin & Romanowicz, 2000; Gu et al., 2001) models and the number of models continue to increase. There are variations between models, but some common features also exist.

Near the surface, the strongest lateral variations are observed. These variations are dominated by large-scale structures which correlate with surface tectonics. For example, continents and mid-ocean ridges are characterised by faster and slower wave speeds, respectively. The strength of the heterogeneities diminishes in the middle mantle. Moreover, heterogeneities of varying sizes are observed, i.e., the power spectrum of lateral variation is whiter compared to that near the surface. As the depth increases to the bottom of the mantle, both the size and strength of heterogeneities increase. In particular, fast anomalies are observed in a ring around the Pacific, and there are two large slow regions underneath the central Pacific and Africa which are interpreted as superplumes. Modelling for bulk sound speed variations has a shorter history (e.g., Su & Dziewoński, 1997; Kennett et al., 1998; Masters et al., 2000c), but one common and striking feature of the bulk sound model is its strong global anti-correlation with the shear wave anomaly in the lower-most mantle.

Because body wave data are insensitive to lateral variation in density, attempts to determine the density structure of the mantle have been made using the history of plate motion and subducted slabs (Ricard et al., 1993; Lithgow-Bertelloni & Richards, 1998). Using surface waves, Tanimoto (1991) has determined an upper mantle density model which is dominated by high degree components. There is also an attempt to obtain density variations directly from gravity anomalies and the surface plate velocity field (Ye, 1989). However, this is a highly non-unique problem, and its resolution with depth is nearly non-existent.

Free oscillations, unlike body waves, are sensitive to the density distribution in the entire mantle, because the gravitational restoring force is important for long period waves. Despite this theoretical sensitivity, most normal mode studies consider only lateral variations in shear wave speed, under the assumption that variations in compressional wave speed and density are related to shear wave structure (e.g., Ritzwoller et al., 1988; Li et al., 1991a; Resovsky & Ritzwoller, 1999a). The currently available normal mode database is large enough to allow for independent modelling of elastic parameters and density. The aim of this Chapter is to construct models of wave speeds or elastic moduli and density mainly from normal mode data. Although the mantle modelling presented here relies on mode data, two different data sets are considered. Data from mantle sensitive modes are combined with free air gravity coefficients to better constrain density structure in the first analysis. In contrast, the second analysis uses only seismic data. It analyses both mantle and inner core sensitive modes to obtain mantle and inner core structure simultaneously. This inversion includes travel time data for a better constraint on inner core anisotropy which is discussed in following Chapters.

Because only splitting coefficients up to and including spherical harmonic degree 6 are included in the data vector d, the mantle models obtained from inversions are also truncated at this degree. Moreover, the mode database is dominated by isolated modes, hence the models consist solely of even degrees. Chebyshev polynomials (Su, 1992) up to and including radial order 13 are chosen as the radial basis functions unless otherwise noted.

3.2 Data Set 1: Free Air Gravity, and Mantle Sensitive Normal Mode

Inversions are performed with various parametrisations; seismic parametrisation, in terms of seismic wave speeds; with mineralogical parametrisation, in terms of elastic moduli; and with hybrid parametrisation, in terms of shear wave and bulk sound speeds. In addition, models are obtained for cases where scaling between parameters are assumed (Section 2.2.1). The scaling factors are constant throughout the mantle and take values of 0.55 for ν_α, 0.2 for ν_ρ, and 0.5 for relating variations in shear wave speed to bulk modulus κ. There are many possibilities for defining the model vector m, and a scheme to refer to different inversion results becomes necessary. To describe the model set, an alphabet is assigned to each parameter: S for shear wave speed, P for compressional wave speed, M for shear modulus, K for bulk modulus, B for bulk sound speed, R for density, and D for topography on boundaries. Models are identified by which parameters are considered in the inversion. The full parametrisation, i.e., without any scaling assumptions, are therefore named SPRD, MKRD, or SBRD. When there are fewer than four letters in a name, the missing volumetric model has been scaled to be part of shear wave or shear modulus model, and topography on boundaries are ignored. For example, a model MK indicates that the model vector is defined in terms of shear and bulk moduli; the density variations are scaled into shear modulus and boundary undulations are ignored.

Throughout the inversions presented in this Chapter, the same damping is applied to the two elastic parameters, and the damping of the density model is required to be the same as, or slightly greater than, that of the other two volumetric models. In order to obtain reasonable topography on the free surface, the amplitude of topography on this boundary has been damped to a size which is between the observed dynamic topography (Cazenave et al., 1989; Gurnis, 1990) and that predicted from mantle flow calculations (Forte & Woodward, 1997). The 660-km discontinuity model has also been damped strongly towards the model of Gu et al. (1998). Finally, damping on the core-mantle boundary is determined by requiring that the peak-to-peak amplitude is in agreement with that of Morelli & Dziewoński (1987).

Table 3.1: Summary of Variance Reductions and χ^2 Tests

Model	$\mathrm{VR_m}$ (%)	χ^2/N	$\chi^2/(N-M)$	$\mathrm{VR_g}$ (%)
Starting Model	74	6.6		
S	89	2.7	3.1	NA
M	89	2.7	3.1	NA
SP	90	2.5	3.3	NA
SB	90	2.5	3.4	NA
MK	90	2.5	3.3	NA
SPRD	92	2.0	3.5	96
SBRD	92	2.1	3.6	95
MKRD	92	2.1	3.6	95

Variance reduction of mode data $\mathrm{VR_m}$, gravity data $\mathrm{VR_g}$, χ^2/N, and $\chi^2/(N-M)$, where $N = 2850$ is the number of even degree data and M is the number of even degree model parameters, achieved for starting and various model parametrisations. The starting model is the full starting model with two seismic waves, scaled density, and topography models.

3.2.1 Results

It would take up too much space to discuss results from every single inversion, so they have been summarised in terms of statistical values. In Figures 3.1*a* and *b*, mode-by-mode improvements in χ^2/N are illustrated when the fit achieved by model SKS12WM13 is compared to the fit based upon model S. Fundamental spheroidal modes ($_0$S branch), which are sensitive to shear wave structure in the middle mantle, show large improvements, indicating that mid-mantle shear wave heterogeneity in model S is different from that in SKS12WM13. Improvements in fit to the toroidal modes are not as obvious as for the spheroidal modes. When independent lateral variations in compressional wave speed are introduced, spheroidal modes of low angular degree show the largest improvements in fit (Figure 3.1*c*). These modes, particularly the fifth overtone branch, are generally more sensitive to compressional wave heterogeneity. Because toroidal modes do not have any sensitivity to compressional waves, it is counter-intuitive to see improvements in fit to fundamental toroidal modes (Figure 3.1*d*). In model S, the shear wave model is forced to accommodate compressional wave variations in order to fit the well-determined spheroidal modes, many of which have considerable sensitivity to compressional wave structure. On the other hand, model SP allows for independent variations in two seismic waves, such that modes sensitive to compressional wave structure no longer alias this structure into shear wave structure. Hence the shear wave speed model is available to fit the toroidal modes. The improvements in fit going from SP to SPRD are most evident in the low degree, higher frequency spheroidal modes with significant sensitivity to density (Figure 3.1*e*). In contrast, allowing for independent variations in density and topography does not affect the fit to toroidal modes significantly (Figure 3.1*f*).

The statistical results of the different inversions and parametrisations are summarised in Table 3.1. Ideally, $\chi^2/(N-M)$ decreases as M is increased, if the additional number of model parameters is warranted by the data. The models are over-parametrised in radius, therefore $\chi^2/(N-M)$ does not necessarily improve when the number of model parameters is increased. The statistical validity of the increased number of model parameters from S to SPRD is investigated in Table 3.2. The $\chi^2/(N_e - M_e)$ test is not useful when the models are over-parametrised, as in inversions with Chebyshev polynomials up to order 13 (Table 3.1). Over-parametrisation with strong damping on higher-order polynomials is preferred to allow data to dictate the radial variations in the models, rather than parametrising the models with fewer degrees of freedom. To determine the number of radial parameters that can be resolved by the data, the maximum Chebyshev polynomial order is decreased until an effect on $\chi^2/(N-M)$ is observed; this occurs at about order 7. When the models

Figure 3.1: Mode-by-Mode Improvements in Fit

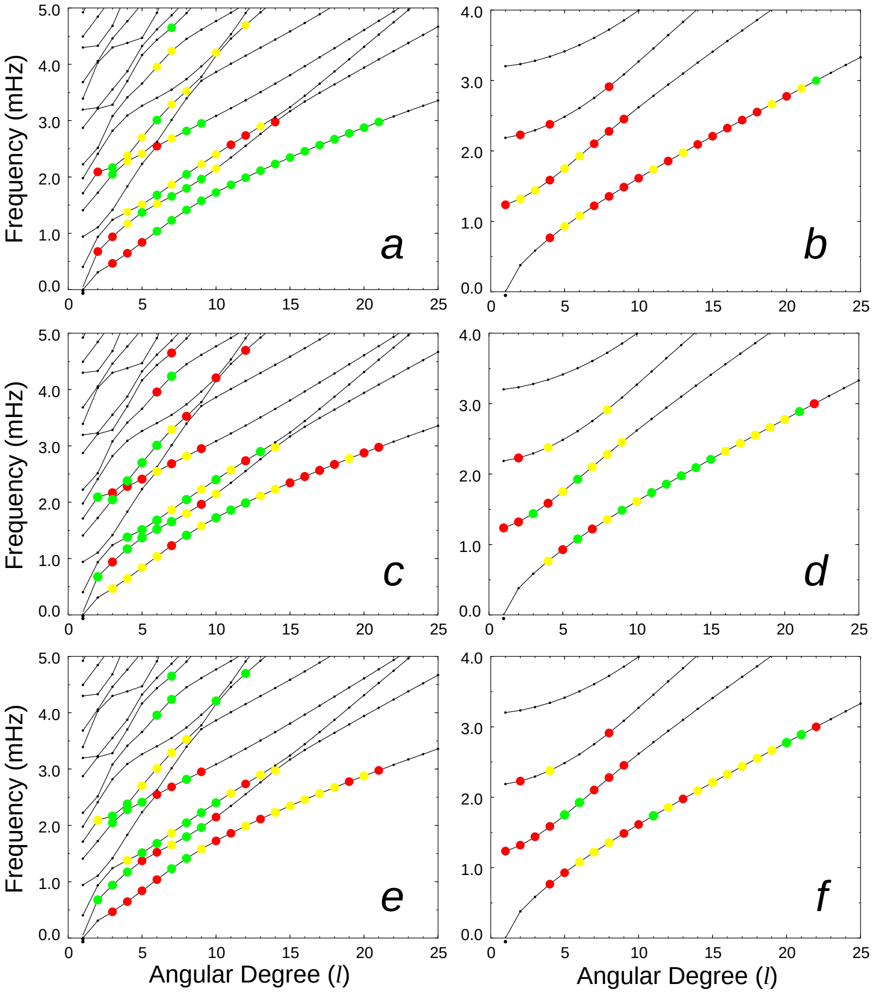

Illustration of mode-by-mode improvements in fit when going from starting model SKS12WM13 to model S (Figures *a* and *b*), from S to SP (Figures *c* and *d*), and from SP to SPRD (Figures *e* and *f*). Values of χ^2/N', where N' denotes the number of splitting function coefficients for that mode, is monitored for each individual spheroidal (left) or toroidal (right) mode. The modes are binned into 3 groups of equal size: modes denoted by green circles show the most improvement in fit, modes indicated by yellow circles are average, and modes denoted by red circles show the least improvement.

(*a*) Improvements in χ^2/N' for isolated spheroidal modes from SKS12WM13 to S.

(*b*) Same as in (*a*) but for toroidal modes. Note that the fit to these modes does not improve very much compared to the spheroidal modes.

(*c*) Same as in (*a*) but for improvements in fit from S to SP. Compared to (*a*), modes with low angular degrees improve in fit.

(*d*) Same as in (*b*) but for improvements in fit from S to SP. The fundamental toroidal modes show large improvements in fit.

(*e*) Same as in (*a*) but for improvements in fit from SP to SPRD.

(*f*) Same as in (*b*) but for improvements in fit from SP to SPRD. Density heterogeneity does not affect the fit to toroidal modes significantly.

Table 3.2: Statistical Results with Different Number of Chebyshev Polynomials

Model	VR (%)	χ^2/N	$\chi^2/(N-M)$
S (K13)	89	2.7	3.1
SP (K13)	90	2.5	3.3
SPRD (K13)	92	2.0	3.5
S (K7)	88	3.0	3.2
SP (K7)	90	2.5	2.9
SPRD (K7)	92	2.1	2.8

Comparison of statistical results for a variety of model and radial parametrisations. K13 indicates that models are expanded radially in Chebyshev polynomials up to and including order 13 (over-parametrised inversion), and K7 models use Chebyshev polynomials up to and including order 7.

are expanded radially up to order 7, $\chi^2/(N-M)$ improves with the addition of compressional wave speed, and again when density and boundary topography are added. Masters et al. (2000b) find that the fit to their data set does not improve when an independent density model is allowed for in their inversions, leading them to conclude that density inversions are premature. This may have arisen from the difference in mode database, or from the *a priori* damping used in the analysis.

Because individual models do not vary significantly with changes in the number of model parameters (for example, the shear wave speed model from S is virtually identical to that of SB), discussion will be focused on models SPRD, MKRD, and SBRD. These three models, obtained from different inversions, are compatible with one another. As an example, the density models obtained from the three inversions SPRD, MKRD, and SBRD are compared in Figure 3.2. It illustrates the consistency of the density models both in pattern and amplitude. In what follows, illustrations of the seismic wave speeds, density and discontinuity models are those of SPRD, the bulk sound model is that of SBRD, and shear and bulk modulus models are from MKRD, unless noted otherwise.

Volumetric Models

Figure 3.3 shows map views of even degree shear wave speed models from inversion and SKS12WM13, and compressional wave speed models from SPRD and P16B30. Recall that the models obtained from these inversions are not readily comparable to existing mantle models because they consist only of the even degrees 2, 4, and 6. For example, the ocean-continent distribution observed in all tomographic models near the surface is difficult to see with only even degrees. The models from SPRD and starting models agree well in the upper mantle with slight differences in the mid-mantle depths (Figure 3.4*a*). As noted in Figure 3.1*a*, some splitting data are particularly sensitive to structure in this depth range. In addition, the correlation of the compressional wave models decreases slightly near the core-mantle boundary, even though the correlation of the shear wave models increases towards the core-mantle boundary. The power, or root-mean-square (RMS) amplitude, of the models is very similar throughout the mantle, except in the transition zone (Figure 3.4*b*,*c*). Note that the RMS amplitude is about half of that shown for a typical model, such as S12WM13 (Su et al., 1994), because only the even degree part of the models is considered.

The correlation between the two seismic wave models of SPRD is high in the upper mantle and around 2500 km depth, but a poorer correlation characterises the middle mantle (Figure 3.5*a*). Towards the core-mantle boundary, the correlation also drops, something that has been noted in other studies (e.g., Robertson & Woodhouse, 1995; Bolton, 1996; Masters et al., 2000c). Both models have high amplitudes in the upper mantle, and relatively small amplitudes in the mid-mantle region (Figure 3.5*b*). The shear wave model increases in amplitude near the core-mantle boundary, whereas the RMS amplitude of the compressional wave model is practically constant throughout the lower

Figure 3.2: Density Models from Different Model Parametrisations

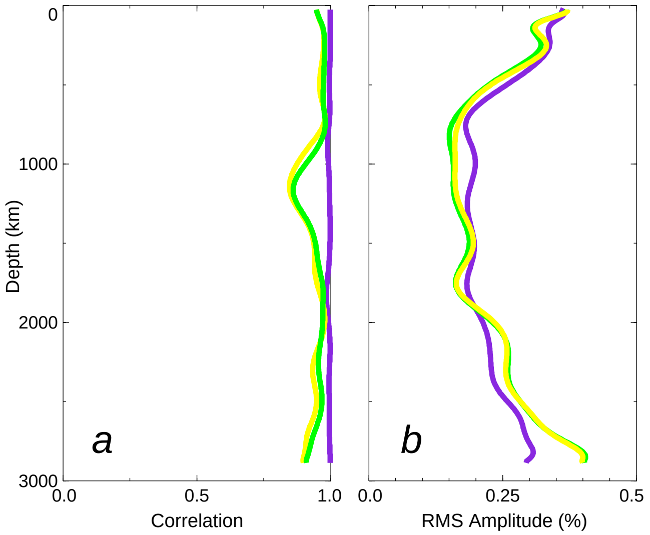

(a) Correlation between density models of SPRD, SBRD, and MKRD. The purple curve is the correlation between SPRD and SBRD, the yellow curve is the correlation between SPRD and MKRD, and the green curve is the correlation between SBRD and MKRD.
(b) RMS amplitude of the density part of SPRD (green), SBRD (yellow), and MKRD (purple) as a function of depth.

mantle.

The most striking feature of the bulk sound speed model is its anti-correlation with shear wave in the lower-most mantle (Figure 3.6). This strong anti-correlation is consistent with models from other studies constrained by shear and compressional wave travel time and waveform data (Su & Dziewoński, 1997; Masters et al., 2000c). In general, the correlation between shear and bulk sound speed models is poor, with significant negative values near the core-mantle boundary (Figure 3.7a). Compared to the shear wave model, the RMS amplitude of bulk sound speed is smaller near the surface and the core-mantle boundary, but similar in the mid-mantle range (Figure 3.7b).

The shear and bulk modulus models shown in Figure 3.6 are also significantly anti-correlated near the core-mantle boundary (Figure 3.7c). Note that the amplitude of the heterogeneity is much larger for the shear modulus model than for the shear wave model (Figure 3.7d). This is an expected result since perturbation in shear modulus $\delta\mu/\mu$ is related to the shear wave speed perturbation $\delta v_S/v_S$ as $\delta\mu/\mu = 2\delta v_S/v_S + \delta\rho/\rho$. Because lateral variations in density are small, the correlations between $\delta\mu/\mu$ and $\delta v_S/v_S$ and between $\delta\kappa/\kappa$ and $\delta v_\phi/v_\phi$ are generally high. However, correlations drop near the core-mantle boundary, suggesting that the density model in the lower-most mantle has different characteristics with larger amplitude.

The laterally heterogeneous whole mantle density model resembles little of either of the two seismic wave models (Figure 3.8a). In fact, the correlation between density and seismic speeds approaches zero as the depth increases towards the core-mantle boundary (Figure 3.8b). Another interesting feature of the density model in mid-mantle range is that there is strong power in degree 4, even though high degree coefficients are discouraged to be large by the smoothness constraints. Near the core-mantle boundary, dense regions roughly correspond to the locations of slow shear wave anomalies, which are traditionally interpreted as mantle upwellings. In contrast, density is reasonably well correlated with the bulk sound anomalies. The amplitude of density heterogeneity

Figure 3.3: Shear and Compressional Wave Speed Models

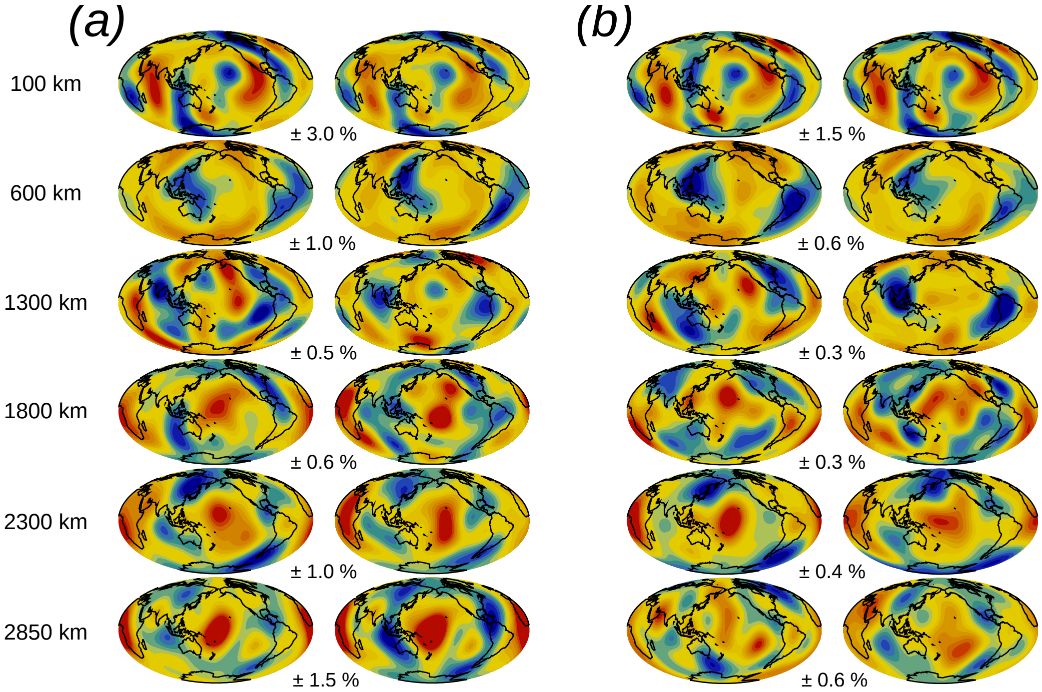

(a) Relative perturbations in shear wave speed models, SPRD (left) and SKS12WM13 (right), at six discrete depths throughout the mantle (using even degree coefficients up to and including degree 6). Blue colours indicate regions of higher than average speeds and red colours indicate slower than average regions. For each depth, the scale for the maps is indicated between the two models.
(b) Same as in (a) except that the compressional wave speed models of SPRD (left) and P16B30 (right) are plotted.

Figure 3.4: Correlation and Power of the Seismic Wave Models

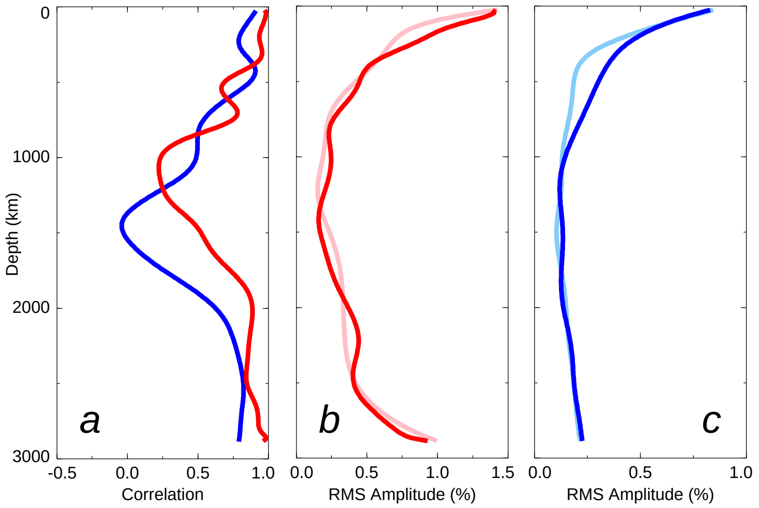

(a) Correlation between the even degree coefficients of the shear wave model of SPRD and SKS12WM13 (red) and the compressional wave model of SPRD and P16B30 (blue) as a function of depth. The 95 % significance level for this number of parameters is 0.32.
(b) Root-mean-square (RMS) amplitude of the shear wave part of SPRD (red) and SKS12WM13 (pink).
(c) RMS amplitudes of the compressional wave part of SPRD (blue) and P16B30 (pale blue).

Figure 3.5: Comparison of the Seismic Wave Models

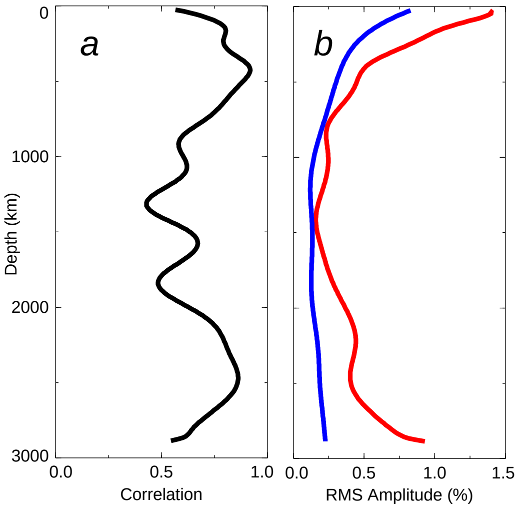

(a) Correlation between the even degree part of the shear and compressional parts of SPRD.
(b) RMS amplitudes for shear (red) and compressional (blue) wave models.

Figure 3.6: Bulk Sound Speed, Shear Modulus, and Bulk Modulus Models

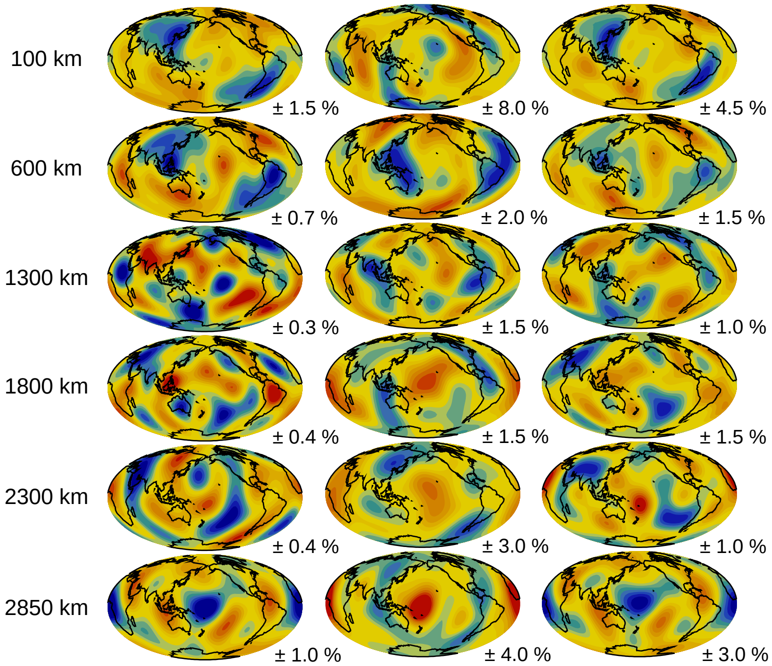

Relative perturbations in bulk sound speed (left), shear modulus (centre), and bulk modulus (right) at six discrete depths. Blue colors indicate regions of higher than average values and red colors indicate lower than average regions. The scale of the maps is indicated at each depth for each model.

Figure 3.7: Comparison of the Shear Wave and Bulk Sound Speeds, and Elastic Moduli

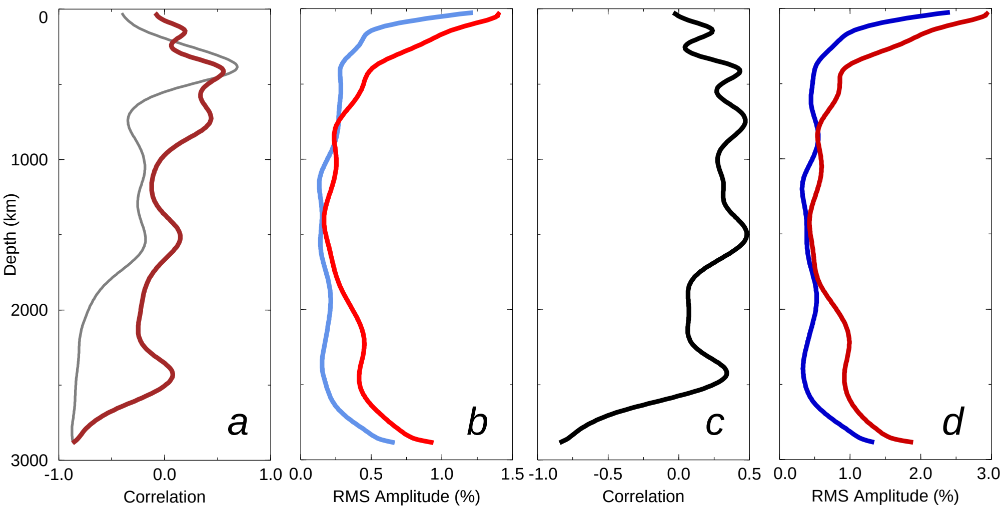

(*a*) Correlation between the shear and bulk sound speed models from SBRD (brown) and the body wave inversion by Su & Dziewoński (1997) (grey). This correlation plot is calculated using only the even degree coefficients.
(*b*) RMS amplitudes of shear wave speed (red) and bulk sound speed (light blue) using even degrees up to and including degree 6. (*c*) Correlation between the shear and bulk moduli.
(*d*) RMS amplitudes of the shear modulus (dark red) and bulk modulus (dark blue) parts of SBRD.

Figure 3.8: Density Model

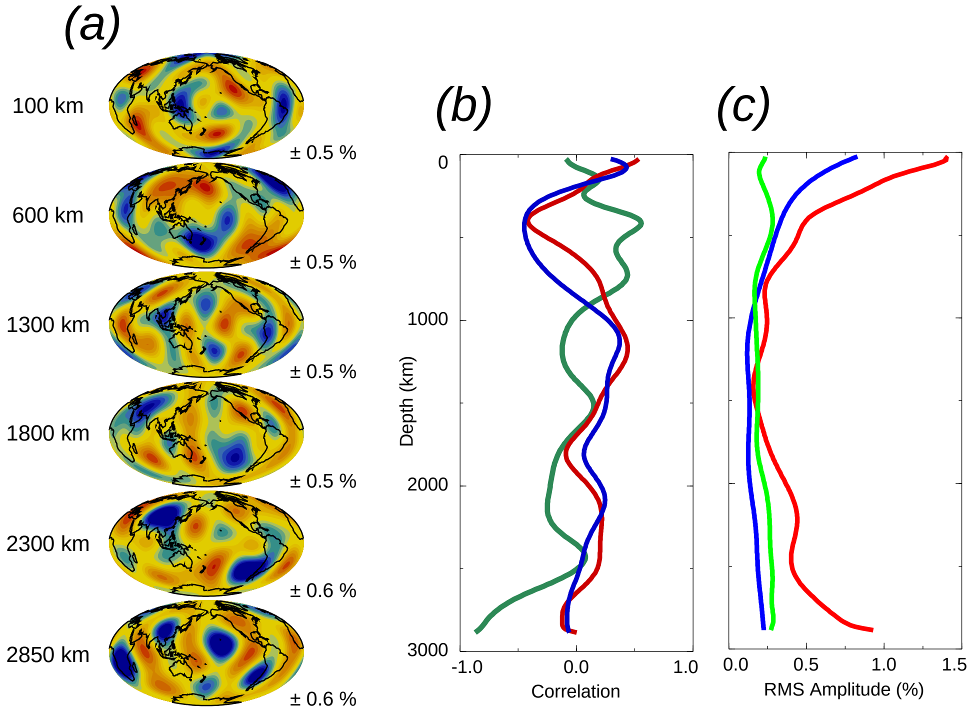

(a) Relative perturbations in density at six discrete depths. Blue regions denote higher than average density and red regions denote lower than average density. The scale of the maps is indicated at each depth. (b) Correlation between the density and shear wave speed (dark red), compressional wave speed (dark blue), and bulk sound speed (dark green) models.
(c) RMS amplitude of shear wave speed (red), compressional wave speed (blue) and density (green) heterogeneity.

Figure 3.9: Models of Topography on Boundaries

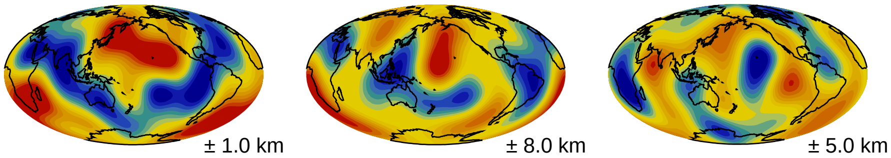

Undulations of the dynamic free surface (left), the 660-km discontinuity (centre), and the core-mantle boundary (right). These maps are plotted using only the even degree coefficients. The scale for the map is indicated beside the model. Blue colours indicate areas of depression and red colours indicate areas of elevation.

is relatively small near the surface and the core-mantle boundary but is compatible to the seismic wave models in the mid-mantle region.

Topographic Models

The models of boundary topography are poorly resolved in inversions, and of the three topographic models the free surface is the least constrained. There is a wide range of acceptable topography on various boundaried with very minor amplitude changes to the density model, and little change in the fit to the free air gravity data.

The surface topography plotted in Figure 3.9 is not related to the continent-ridge distribution as in Forte & Woodward model (1997). This boundary is the least constrained of all the models. Although constraints on the 660-km discontinuity are better, the sensitivity to this discontinuity is still poor, and the strong damping forces the model to be close to that of the starting model (Figure 3.9). The topographic model of the core-mantle boundary (Figure 3.9) is the best constrained of all the boundaries. Interestingly, even though various models of the core-mantle boundary are dominated by power in degree 2, the model from SPRD has the most power in degree 2 order 1, whereas models by Morelli & Dziewoński (1987) and Forte et al. (1995b) have leading power in the second order.

3.2.2 Robustness of the Models

In any non-unique inverse problem, one of the main questions is the reliability of the models. Before interpreting the models, one must identify which parts of the model reflect the true Earth and which parts are artificial. In this section, resolution and the degree of uniqueness of the SPRD inversion are discussed. First, the effects of damping and truncation of radial basis functions are assessed by two different tests. Second, the effects due to *a priori* conditions, such as the data set and starting model, are addressed. The focus will be on the density model, because there are no previous seismically constrained density models to compare results with.

An indication of model robustness can also be obtained by calculating the trace of appropriate part of the resolution matrix, corresponding to the number of resolved parameters. This number for the density model is consistently greater than that of the two wave speed models, regardless of the relative weighting of the gravity data (including mode only inversion).

Resolution Tests

Applying damping to an inverse problem generally reduces the amplitude and smoothes the model. The significance of these effects may be visualised in terms of checkerboard and Backus-Gilbert resolution tests. The checkerboard test investigates how a given model is affected by the inversion process, i.e., smoothed, reduced in amplitude, and contaminated by other models. In contrast, a

Backus-Gilbert resolution test asks how an inverted model is related to the “true” Earth structure (Backus & Gilbert, 1968). These two tests are complementary, and provide an insight into the resolution of various model parameters.

Checkerboard Resolution Tests

To investigate how a given model is influenced by the inversion process, synthetic data are calculated using a given trial model, and are inverted using the same damping as in the real inversion. The comparison of input and output models would then illustrate how the inversion alters the models. In the ideal case, the resulting model is identical to the trial model. Two types of checkerboard tests are performed. The first involves an input model which consists of only one non-zero value for a specific radial order k, angular degree s, and angular order t. This is equivalent to studying the response of the inversion to a δ-function perturbation in the wavenumber domain. The second type of test involves an input model which is a δ-function in a mixed domain: a model with specific angular degree s and order t peaked at a given depth. This type of test examines the radial smearing due to damping.

In Figure 3.10, checkerboard resolution tests are plotted for different input models for the wavenumber case. The most visible result is the reduced amplitude of the recovered models, but leakage of power to other s, t, and k is small. These tests also show that the density model is consistently well recovered, and that it is not a result of contamination from the seismic wave structure as advocated by Kuo & Romanowicz (2002). The shear wave speed is also well resolved, but the recovery of the compressional wave model is relatively poor. The effects of strong damping on higher degree structure manifest itself in terms of a poorer resolution. These tests are also performed with an input in boundary topography to assess the trade off between topographic and volumetric models (Figure 3.11). As discussed earlier, the recovery of topographic models is poor, and some signal is transferred into volumetric models, particularly to density, at depths near the discontinuity. However, the amplitude of heterogeneity introduced by this leakage is much smaller than the amplitude of density model of SPRD.

The radial smearing due to inversion is illustrated in Figure 3.12, where input radial peaks are located in upper, middle, and lower mantle. Note that the truncation of radial basis functions does not allow for a δ-function input and that there is ringing in the input model. Recovered models have smaller amplitude as observed previously, and have structures that are more broadly distributed in radius compared to the input model due to radial smoothness damping. The density model is well resolved near the core-mantle boundary, therefore the peculiar behaviour of density at the lower-most mantle is a reliable result of the inversion.

Backus-Gilbert Resolution Test

To understand which part of the “true” Earth structure is mapped into a given portion of the inverted model, let $m(\mathbf{r}')$ be the model obtained from an inversion at a given position $\mathbf{r}'$, and let $m^{true}(\mathbf{r})$ be the “true” Earth model. Then the Backus-Gilbert resolution kernel is an averaging kernel $A(\mathbf{r}',\mathbf{r})$ relating the inverted and “true” Earth models (Backus & Gilbert, 1968):

$$m(\mathbf{r}') = \int A(\mathbf{r}',\mathbf{r}) m^{true}(\mathbf{r}) d^3\mathbf{r}\,. \tag{3.1}$$

In the ideal case where $m(\mathbf{r}') = m^{true}(\mathbf{r}')$, the Backus-Gilbert resolution kernel is a Dirac-delta function, $A(\mathbf{r}',\mathbf{r}) = \delta(\mathbf{r}-\mathbf{r}')$.

The basis functions $B_i(\mathbf{r})$ have orthogonality of the form

$$\int w(\mathbf{r}) B_i^*(\mathbf{r}) B_j(\mathbf{r}) d^3\mathbf{r} = \delta_{ij},$$

where an asterisk denotes complex conjugation and $w(\mathbf{r})$ is a weighting function. Expanding $m^{true}(\mathbf{r})$ in basis functions, and using the orthogonality relation,

$$m_j^{true} = \int m^{true}(\mathbf{r}) w(\mathbf{r}) B_j^*(\mathbf{r}) d^3\mathbf{r}. \tag{3.2}$$

Figure 3.10: Resolution Tests: Wavenumber Input

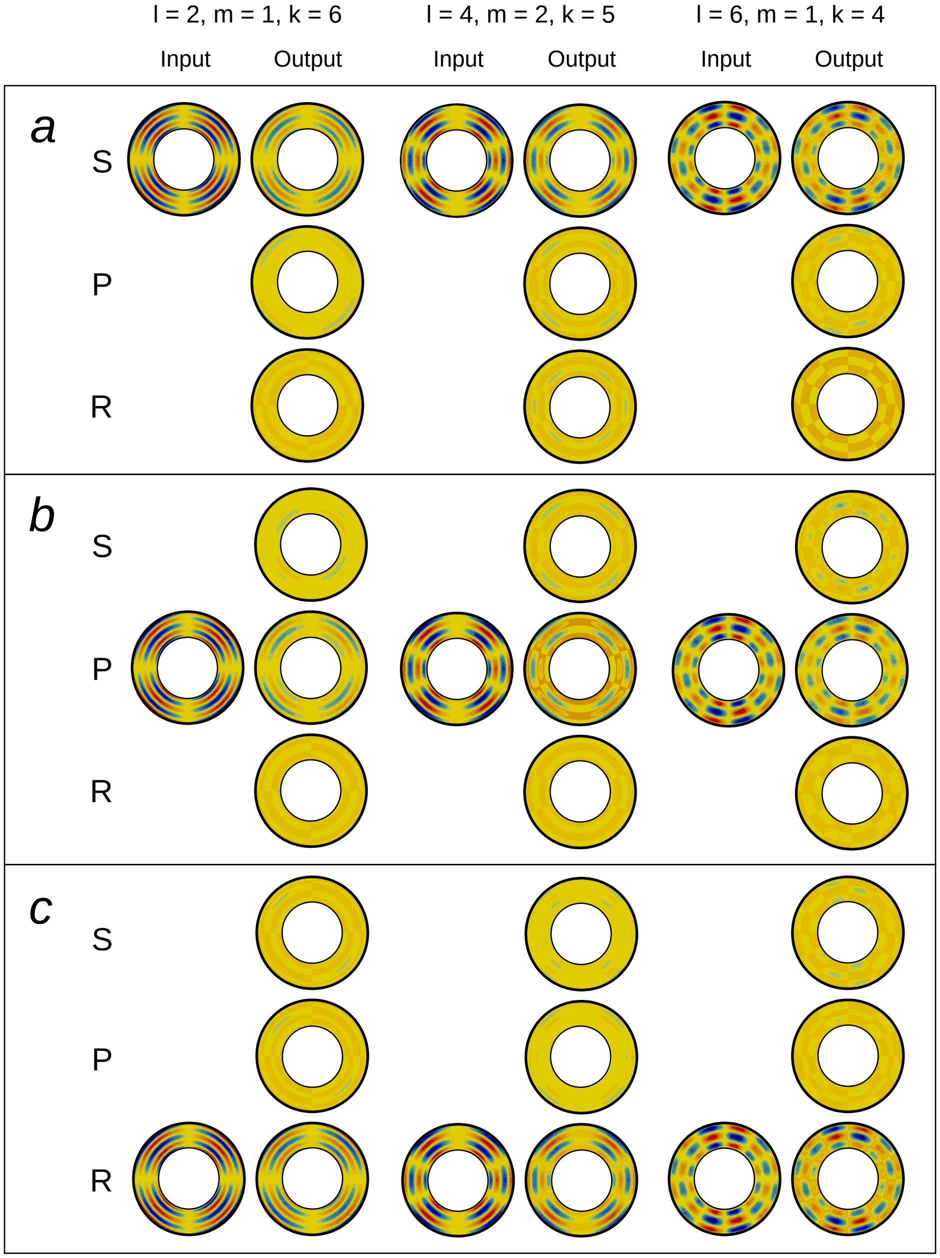

Resolution of shear wave speed (S), compressional wave speed (P), and density (R) with an input at a given spherical degree (s), order (t) and radial order (k).

(a) The input model consists only of shear wave heterogeneity.

(b) The input model consisting only of compressional wave heterogeneity.

(c) The input model consisting only of density heterogeneity.

Figure 3.11: Resolution Tests: the 660-km Discontinuity and the Core-Mantle Boundary

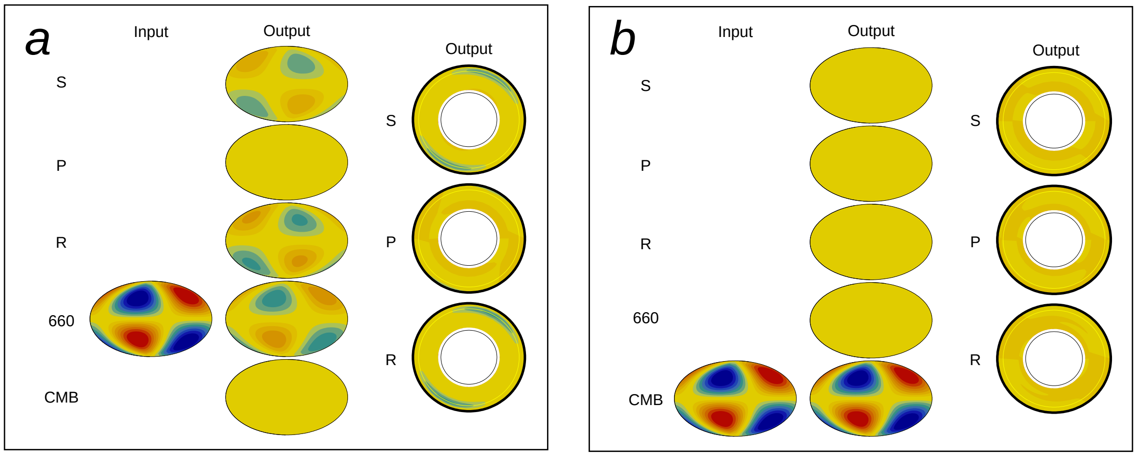

Resolution of shear wave speed (S), compressional wave speed (P), density (R), topography on the 660-km discontinuity (660), and the core-mantle boundary (CMB). Map views of the input and output models are shown on the left, and cross sections of the output volumetric models are shown on the right with the 660-km discontinuity indicated by the yellow circle.
(a) Input model is topography on the 660-km discontinuity with a spike at spherical degree 2 and order 1. Map view of the volumetric models are plotted at 660-km depth.
(b) Input model is topography on the core-mantle boundary with a spike at spherical harmonic degree 2 and order 1. Map views of the volumetric models are plotted at 2850-km depth.

Similarly, the output model $m(\mathbf{r})$ is expanded with basis functions

$$m(\mathbf{r}) = \sum_i m_i B_i(\mathbf{r}).$$

The coefficients m_i are related to the model coefficients m_j^{true} through the resolution matrix, $m_i = \sum_j R_{ij} m_j^{true}$. Substituting this expression for m_i,

$$m(\mathbf{r}) = \sum_{i,j} B_i(\mathbf{r}) R_{ij} m_j^{true}.$$

Combining this expression with equation (3.2),

$$m(\mathbf{r}') = \int \sum_{i,j} w(\mathbf{r}) B_i(\mathbf{r}') R_{ij} B_j^*(\mathbf{r}) m^{true}(\mathbf{r}) d^3\mathbf{r}.$$

Upon comparing the last equation with equation (3.1) the Backus-Gilbert resolution kernel is given in terms of the resolution matrix and the basis functions by

$$A(\mathbf{r}', \mathbf{r}) = \sum_{i,j} w(\mathbf{r}) B_i(\mathbf{r}') R_{ij} B_j^*(\mathbf{r}).$$

Generally, Backus-Gilbert resolution tests are used to determine the averaging in the radial direction. Therefore, they are calculated for specific values of the angular degree s and order t, and the result is plotted as a function of depth.

The Backus-Gilbert resolution kernels are obtained for three depths and at different angular degrees (Figure 3.13). The plots show that structure of models obtained from inversions is originating

Figure 3.12: Resolution Tests: Radial Peak Input

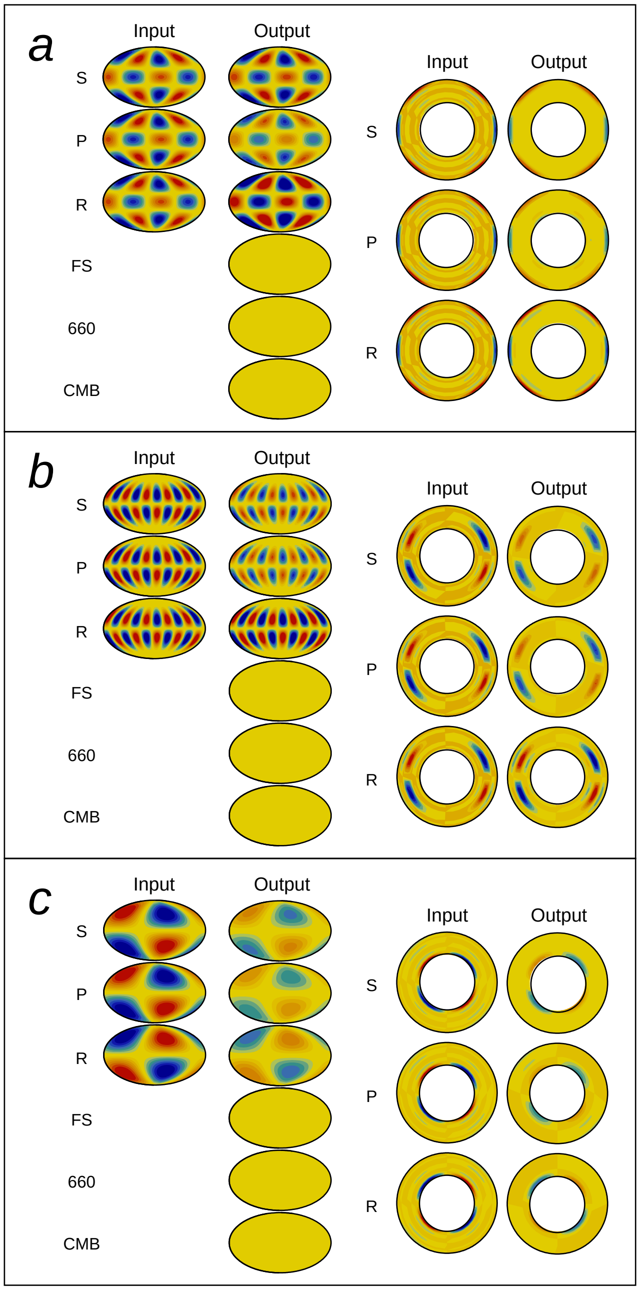

Resolution of shear (S) and compressional (P) wave speeds, density (R), topography on the free surface (FS), the 660-km discontinuity (660), and the core-mantle boundary (CMB). Map views of the models are plotted at the peak depth (left) with cross sections of the volumetric models (right).
(*a*) Radial input with a peak at 200-km depth and lateral input at degree 4 and order 2.
(*b*) Radial input with a peak at 1300-km depth and lateral input at degree 6 and order 5.
(*c*) Radial input with a peak at 2700-km depth and lateral input at degree 2 and order 1.

from averaging the true structure broadly over radius. In addition, they show that contributions from other volumetric models are small. Because of degree dependent damping, the averaging range and effects of other models increase as the angular degree increases. However, the dominant degree 2 signal near the core-mantle boundary is robust and results from relatively narrow averaging and minimal model mixing.

Influence of the *a priori* Conditions and Other Factors

The pattern of density heterogeneity obtained from the mode data alone is stable, but has a range of amplitudes that satisfy the data equally well. Inclusion of the free air gravity anomaly narrows the amplitude range of the density heterogeneity and slightly modifies its pattern in the mid-mantle depths. This has been noted by Forte et al. (1994) when geopotential coefficients were combined with shear wave data to constrain a shear wave model. Because gravity data depend on density and boundary topography in a highly non-unique manner, the addition of gravity data also introduces a trade off between these models. Correspondingly, the inversion is damped to allow for minimal changes to the density and topography models from those obtained from mode only inversion. Influence of boundary topography on density model is investigated in Figure 3.14(a). For this experiment, the free air gravity constraint must be removed from the database, since gravity cannot be modelled without boundary topography. Therefore, two inversions, SPR and SPRD' with only normal mode data are performed. The prime on SPRD' indicates that the models of density and boundary topography are obtained without constraints from the free air gravity anomaly. There is a trade off between density and boundary topography as observed in checkerboard resolution tests, but this does not significantly influence the pattern of density heterogeneity (Figure 3.14a). Introduction of topography, however, does reduce the amplitude of the density model near the boundary (Figure 3.14b). Topography could exist on a mid-mantle boundary (e.g., Kawakatsu & Niu, 1994; Wen & Anderson, 1997) or on discontinuities within D" (e.g., Lay et al., 1998). Because most modes have negligible sensitivity to undulations on internal discontinuities, these additional boundaries are unlikely to alter volumetric models significantly. They are, however, important when calculating the gravity anomaly, but this mainly alters the amplitude of the density model and not its pattern.

Resovsky & Ritzwoller (1999b) argue that *a priori* starting models have significant impact on the resulting density model. To address this concern, the scaling value for the shear wave to density conversion, ν_ρ, is varied to produce different starting models for density, including zero model. The density models are consistent with one another and show patterns similar to those in Figure 3.8(a) (Figure 3.14c). The density model is also relatively insensitive to the compressional wave starting model. As indicated by the lower correlation, the compressional wave speed model is more dependent upon the starting model than the density model. The density model can be influenced by the parametrisation of the inversion such as SPRD or MKRD. However, models obtained from three inversions with different parametrisations are highly compatible with one another (Figure 3.2), indicating that the dependence of density on parametrisation is also limited.

Inversions with various levels of random noise added to the splitting function coefficients are performed to investigate the effects of data quality (Figure 3.15a). The density model is most affected by the addition of random noise, because its amplitude is generally smaller than the seismic wave models. If the data set is of insufficient quality to determine independent lateral variations in density, as suggested by Masters et al. (2000b), models will be affected significantly by the addition of noise. However, the resulting models are highly consistent with the original model, indicating that the data quantity and quality are sufficient to constrain density heterogeneity, even with substantial uncertainties in the splitting functions.

Although splitting coefficients are relatively consistent between various groups (Figures 2.3 and 2.4), inversions are performed with a data set in which the measurements and their associated error estimates are averaged. The models obtained from this data set are virtually identical to those based upon the data set with multiple observations. To further demonstrate the independence of

Figure 3.13: Backus-Gilbert Resolution Kernels

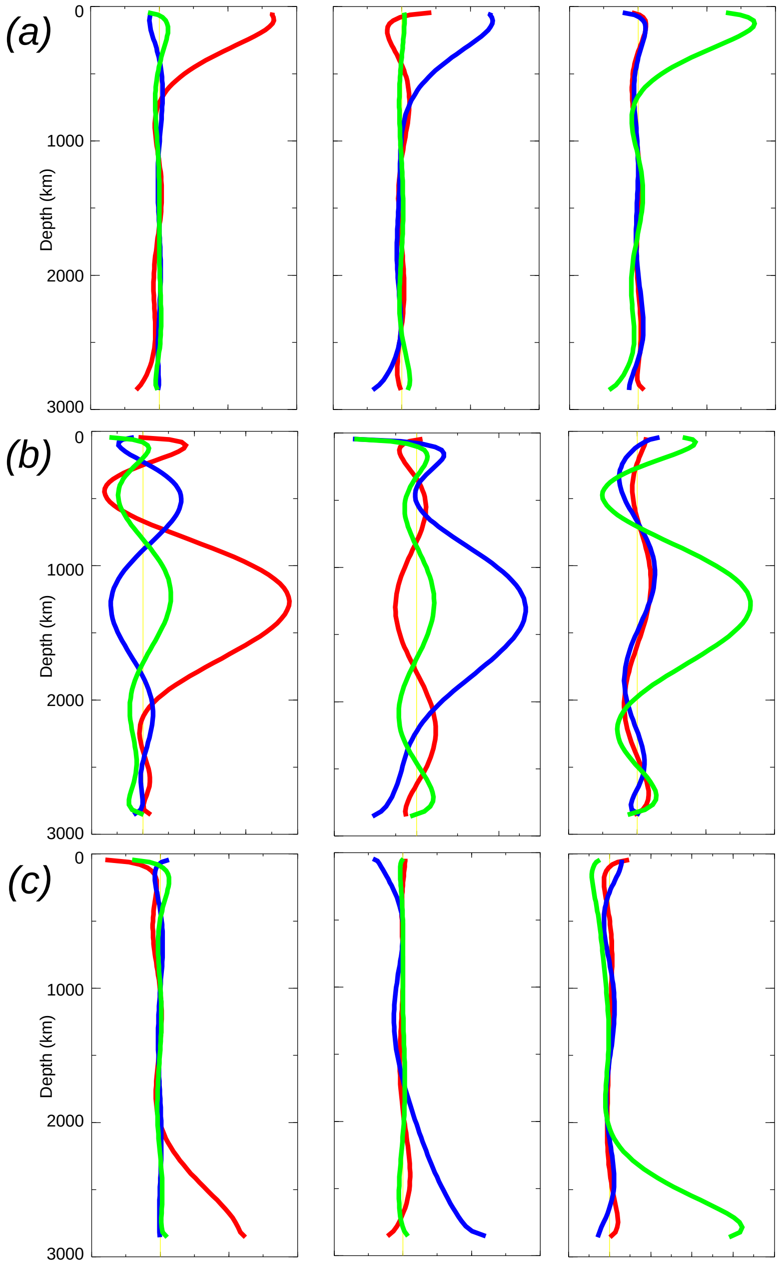

(*a*) Backus-Gilbert resolution kernels for structure at 200-km depth with $s = 4$ and $t = 3$ for shear wave speed (left), compressional wave speed (centre), and density (right). The red curve represents the shear wave speed, the blue curve represents the compressional wave speed, and the green curve represents density. The yellow line is the zero line.
(*b*) Same as in (*a*) but with structure at 1300-km depth with $s = 6$ and $t = 5$.
(*c*) Same as in (*a*) but with structure at 2800-km depth with $s = 2$ and $t = 1$.

Figure 3.14: Comparison of Density Models with Different *a priori* Conditions

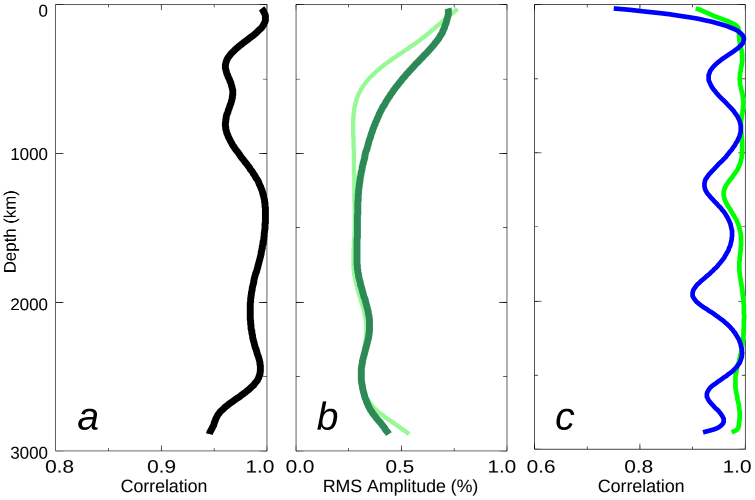

(*a*) Correlation between the density models of SPR and SPRD'.
(*b*) RMS amplitude of the density parts of SPR (pale green) and SPRD' (dark green).
(*c*) Correlation between the compressional wave or density model of SPRD (with starting models P16B30 and scaled SKS12WM13) and those obtained from an inversion with zero starting models. The green curve is the correlation between the two density models and the blue curve is the correlation between the two compressional wave models.

the density model, the data set is divided into two subsets. The first subset consists of data from Resovsky & Ritzwoller (1998) only, and the second consists of data from He & Tromp (1996). Strictly speaking, each subset is not large enough to do an SPRD inversion, nevertheless, this experiment demonstrates the robustness of the density model. Even though changes due to fewer number of data are unavoidable, models are similar to the density model from the complete data set (Figure 3.15*b*), and near the core-mantle boundary, the dense anomalies underneath the central Pacific and Africa appear in each case.

To address the issue of anisotropy, the change in fit of individual modes is monitored as the number of degrees of freedom is increased (Figure 3.1). The fit to the toroidal modes, which are not sensitive to compressional wave heterogeneity, is improved when this model is introduced. To investigate the possibility of mapping anisotropic shear wave structure into the compressional wave model, an inversion with only spheroidal modes is performed. The resulting models are highly consistent with models obtained based upon the entire data set (Figure 3.15*c*), suggesting that isotropic heterogeneity is modelled, rather than aliasing shear wave anisotropic signal into compressional wave model. However, anisotropy is not fully explored in this study.

3.2.3 Depth Dependent Scaling Relationship

One of the applications of the laterally varying models of the mantle is to compare with mineral physics predictions. A common practice is to compare seismically obtained scaling values relating two models, such as shear wave speed and density, with values determined by theoretical calculations or experiments. The depth dependent scaling relationship between shear wave and density, $\nu_\rho(r)$, is particularly important, because it is used in mantle flow calculations, such as modelling of the gravity field and constraining the radial viscosity profile.

Figure 3.15: Effects of Random Noise and the Choice of Data

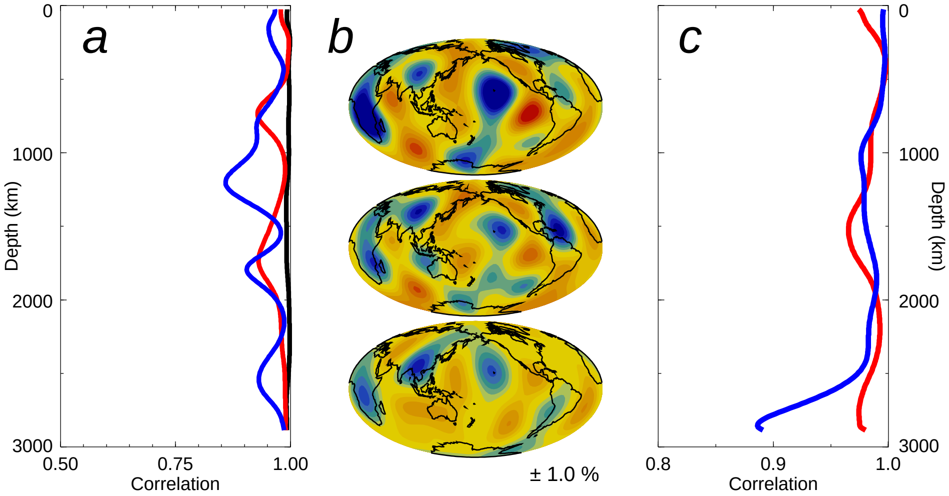

(*a*) Comparison between the density model of SPRD and density obtained from data to which 10% (black curve), 20% (red curve), and 30% (blue curve) random noise is added. Note that the correlation ranges from 0.5 to 1.0 on the x-axis instead of from -1.0 to 1.0. Only the density models are compared because they are affected most by the addition of random noise.
(*b*) Density models at 2850 km depth based upon SPRD (top), modes reported by Resovsky & Ritzwoller (1998; middle), and modes reported by He & Tromp (1996; bottom). Blue regions denote higher than average density and red regions denote lower than average density. The scale of the maps is indicated on the bottom right corner.
(*c*) Correlation of shear (red) or compressional (blue) wave models obtained from full data set and from data set with only the spheroidal modes.

Mineral physicists determine depth dependent relationships between various model parameters, such as seismic wave speeds, by assuming that variations are due to temperature. For example,

$$\nu_\beta = \left(\frac{\delta \ln v_S}{\delta \ln v_P}\right)_P = \frac{v_P}{v_S}\,\frac{(\partial v_S/\partial \mathrm{T})_P}{(\partial v_P/\partial \mathrm{T})_P} \qquad \text{or} \qquad \nu_\rho = \left(\frac{\delta \ln \rho}{\delta \ln v_S}\right)_P = \frac{v_S}{\rho}\,\frac{(\partial \rho/\partial \mathrm{T})_P}{(\partial v_S/\partial \mathrm{T})_P},$$

where T denotes temperature, and the derivatives are determined at constant pressure P. The temperature derivatives can be determined by laboratory experiments, and measurements on mantle minerals provide the value between 1.0 and 1.6 for ν_β (e.g., Anderson & Suzuki, 1983; Isaak et al., 1989; Anderson et al., 1991; Isaak, 1992; Anderson & Isaak, 1995). Values greater than 1.6 are not observed by laboratory studies. Alternatively, mineral properties can be considered theoretically. Determination of ν_β by theoretical calculations, such as lattice dynamic calculation and thermodynamic calculations with anelasticity, provide values that are much larger than those from experimental studies, between 1.4 and 2.5 (e.g., Agnon & Bukowinski, 1990; Reynard & Price, 1990; Isaak et al., 1992; Karato, 1993a; Karato & Karki, 2001). The other scaling factor ν_ρ determined from experiments take values of 0.4 to 1.0 (e.g., Anderson et al., 1968; Isaak et al., 1989; Chopelas & Boehler, 1989; Chopelas, 1992). However, it is significantly reduced to values between 0.2 and 0.4 by theoretical evaluations (e.g., Anderson, 1987; Karato, 1993a). The formulation with temperature derivatives neglects variations due to other factors, such as composition, a phase change, or partial melting. The validity of purely thermal source of lateral variations is debatable, especially when the correlation between two models is low, and this may be the cause of discrepancies between mineral physics and seismic estimates.

Early studies on the relationship between shear and compressional wave variations focused on the arrival times of the two waves. The ratio ν_β in the upper mantle is constrained by comparison of P and S arrivals, giving values which ranged from 1.3 to 2.7 (e.g., Doyle & Hales, 1967; Jeffreys & Singh, 1973; Romanowicz & Cara, 1980; Wickens & Buchbinder, 1980; Souriau & Woodhouse, 1985; Bokelmann & Silver, 1993). The ratio in the lower mantle is obtained using differential travel times PcP−P and ScS−S to give $1.7 \leq \nu_\beta \leq 2.5$ (e.g., Hales & Roberts, 1970; Jordan & Lynn, 1974; Lay, 1983; Pulver & Masters, 1990). Normal mode data have also been used to constrain ν_β mostly for the lower mantle, and the value ranges between 1.7 and 2.5 (e.g., Giardini et al., 1987, 1988; Li et al., 1991b). With arrival of tomographic models, ν_β are calculated from shear and compressional wave models. One can use the ratio of the RMS amplitudes of the two seismic wave models, which gives values between 1.0 and 3.0 (e.g., Dziewoński & Woodhouse, 1987; Ritzwoller & Lavely, 1995; Vasco et al., 1994; Robertson & Woodhouse, 1995; Kennett et al., 1998; Masters et al., 2000c). Alternatively, ν_β can be included as one of the model parameters and jointly inverted with either shear or compressional wave model (e.g., Bolton, 1996; Robertson & Woodhouse, 1996). The range of values obtained in this case is similar to that from the comparison of the RMS amplitudes. These methods rely on a perfect correlation between shear and compressional wave heterogeneity, which has been shown to be questionable, especially in the lower mantle (e.g., Robertson & Woodhouse, 1995; Bolton, 1996; Figure 3.5*a*).

The second factor ν_ρ can be obtained from geodynamic studies. These studies require density distribution within the mantle, and derive such a model by converting seismic wave models using the factor ν_ρ. Investigations to explain data such as gravity anomalies and glacial rebound lead to ν_ρ between 0.0 and 0.4 (e.g., Corrieu et al., 1994; Forte et al., 1994; Forte & Mitrovica, 2001).

In this study, models obtained from inversion are analysed to derive depth dependent ν_β and ν_ρ. Rather than determining scaling factors based upon RMS ratios, least squares fit of a straight line with slope ν to coefficients with uncertainties is applied (York, 1969). At a given depth, a constant value, ν, is sought for, which best relates model X to model Y by minimising the objective function

$$f(\nu) = \sum_i \frac{(y_i - \nu x_i)^2}{(\Delta y)_i^2 + \nu^2 (\Delta x)_i^2}\ . \tag{3.3}$$

The summation, i, is over all coefficients, and x_i and y_i are the coefficients of models X and Y with their associated uncertainties $(\Delta x)_i$ and $(\Delta y)_i$, respectively. The derivation of equation (3.3)

Figure 3.16: Depth Dependent Scaling Relationships

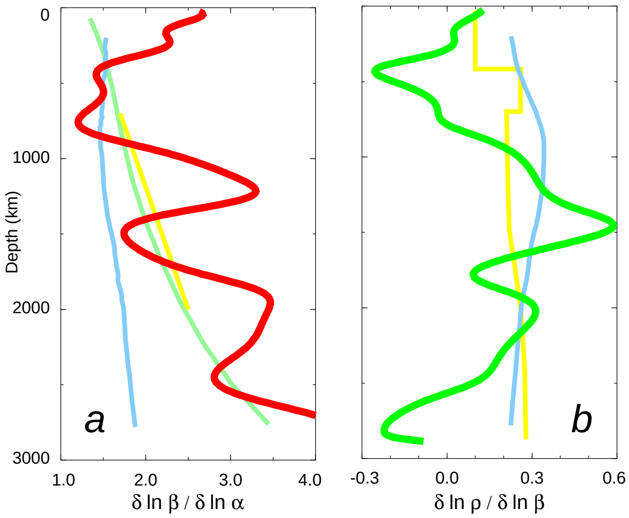

(a) Proportionality between the shear and compressional wave speed models ν_P. The red curve is the estimate based upon the SPRD inversion. The yellow curve represents the model from Robertson & Woodhouse (1996), the pale green curve is from Bolton (1996), and the light blue curve is from Karato (1993a). The former two curves are determined by inverting shear and compressional wave data for shear or compressional heterogeneity and a depth dependent scaling factor, assuming a perfect correlation between the two wave speed models. Karato's profile is based upon mineral physics estimates.
(b) Proportionality between density and shear wave speed ν_ρ. The green curve is obtained from the shear wave and density parts of SPRD, the light blue curve is from Karato (1993a) and the yellow curve is from Forte et al. (1994).

is discussed in Taylor (1997). The uncertainties assigned to each coefficient in this analysis are not taken from the diagonal elements of the covariance matrix. As discussed in Chapter 2, in a damped inversion, the elements of the covariance matrix do not represent realistic error estimates. In this analysis, error estimates based upon data abundance is employed, i.e., the uncertainty is prescribed to be inversely proportional to the square root of the number of observations at a given degree and order.

In Figure 3.16a, the depth dependent scaling parameter ν_β obtained through the regression analysis is shown together with seismic estimates from Bolton (1996) and Robertson & Woodhouse (1996), as well as an estimate from mineral physics (Karato, 1993a). Seismically obtained values for the scaling between shear and compressional waves are highly consistent with one another. However, the result from SPRD and the profile determined by Bolton differ in the upper mantle, even though the correlation between the two seismic wave speed models is relatively high (Figure 3.5a). Other seismic studies, using data such as station corrections, indicate an upper mantle value of around 2 (e.g., Souriau & Woodhouse, 1985), which is in good agreement with the result using SPRD. The high value near the surface is usually attributed to the presence of large-scale partial melting. In the lower mantle, seismically determined values are larger than estimates based upon mineral physics. Subsequently, various mechanisms, such as large scale partial melting (Agnon & Bukowinski, 1990; Isaak et al., 1992), compositional heterogeneity (Jeanloz & Knittle, 1989; Jackson, 1998), and a phase change (Yeganeh-Haeri et al., 1989), have been invoked to explain the discrepancy.

Figure 3.17: Correlation and Scaling Relation

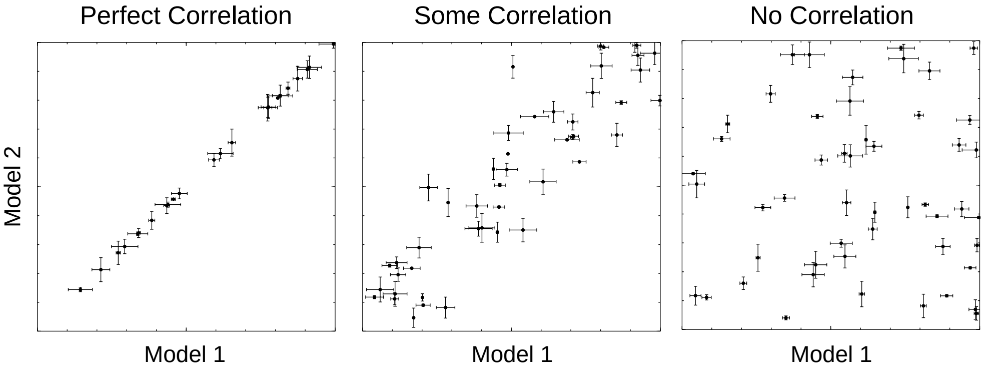

Data from hypothetical models are shown to illustrate the effects of correlation and the validity of scaling assumption.

When two models are perfectly correlated, the problem of finding the slope is well-defined, because the coefficients lie on a straight line. However, when the two models are poorly correlated, the coefficients x_i and y_i are randomly distributed and the best fitting slope is either zero or infinity. As the correlation between two models decreases, the assumption that the two models can be related by a single parameter breaks down (Figure 3.17). Examples of this are the unreasonably large values around 1300 km and beneath 2500 km depth where the correlation between the two seismic speed models is low (Figure 3.5*a*). The particularly large values near the core-mantle boundary are due to the compounded effects of a poor correlation and an increasing RMS amplitude ratio. Here, at the thermal boundary layer, another unknown is the effect of anisotropy, the existence of which has been suggested (e.g., Lay et al., 1998).

In Figure 3.16*b*, the factor ν_ρ based upon the density and shear wave models are compared to those of Karato (1993a) and Forte et al. (1994). The profile by Karato is calculated using thermal derivatives based upon an experimentally determined activation energy and considering the effects of attenuation. On the other hand, the profile by Forte and others has been obtained through an inversion of geopotential and seismic observations. The profiles are in reasonable agreement in the mid-mantle depths where the correlation between density and shear wave speed variations is relatively high. Differences between the profiles occur around the transition zone and in the lowermost mantle, and the scaling values obtained in these regions are often negative. The profile of ν_ρ plus-or-minus one error bar defines a range that includes both Karato's and Forte's models almost throughout the mantle. However, considering the low correlation between density and shear wave speed, it is questionable to use the assumption that a scaled wave speed model characterises the density structure of the mantle.

3.3 Data Set 2: Mantle and Inner Core Sensitive Normal Mode

Thus far, modelling of density variations within the mantle has relied upon mantle sensitive modes (Ishii & Tromp, 1999; Masters et al., 2000b; Kuo & Romanowicz, 2002). Despite their sensitivity to mantle structure, inner core sensitive modes have been ignored in studies of the mantle, because these data exhibit a strong inner core signature. To overcome this dilemma, mantle and inner core sensitive modes are simultaneously inverted for mantle heterogeneity and inner core anisotropy in

Table 3.3: Mode and Travel Time Inversions

Model	χ^2	χ^2_7	VR(modes)	VR(IC)	VR(DF)	VR(BC)	VR(AB)
S	3.3	3.4	90	77	84	71	75
SP	3.0	3.0	91	80	83	72	75
SPR	2.7	2.7	92	83	84	71	74

Table summarising the fit for different number of model parameters within the mantle. Inner core anisotropy is assumed to be uniform. A χ^2 test for the overall fit is given by $\chi^2 = \chi^2/(N - M)$ and $\chi^2_7 = \chi^2/(N - M_7)$, where N denotes the number of data, and M and M_7 are the number of model parameters with $k_{\max} = 13$ and 7, respectively. VR(modes) is the variance reduction of the entire normal mode data set, and VR(IC) is the fit to inner core sensitive modes. VR(DF) is the variance reduction for $\mathrm{PKP_{DF}}$ data, VR(BC) is the variance reduction for $\mathrm{PKP_{BC}}-\mathrm{PKP_{DF}}$ data, and VR(AB) is the variance reduction for $\mathrm{PKP_{AB}}-\mathrm{PKP_{DF}}$ data.

this section. The results for the inner core are discussed in the next Chapter.

In this analysis, only a seismic parametrisation is considered. The same labelling scheme for different model vector set up is used as in the previous section. However, topography, because the data set does not include gravity anomaly, is never included in modelling. The starting models are as discussed in the previous Chapter except that a zero starting model is used for density model. Because inner core modes are strongly sensitive to the compressional wave structure in the mantle, this model is damped twice as hard as shear wave or density model. This is required to avoid putting inner core signal into the mantle. Finally, this section uses Chebyshev polynomials as the basis function, but inversions are also performed with cubic b-splines and layers to investigate the dependence of the density model on the radial basis function.

3.3.1 Results

Statistical results of inversions with different number of parameters within the mantle are presented in Table 3.3. An increase in parameters from an S to SPR inversion is supported by a systematic decrease in $\chi^2/(N-M)$. In the previous section, this decrease in $\chi^2/(N-M)$ is obtained when the maximum radial parametrisation ($k_{\max}$) is 7, but the improved modal database supports a decrease in $\chi^2/(N-M)$ even when $k_{\max} = 13$. The fit to the body wave data does not change more than a couple of percent, suggesting that additional parameters in the mantle do not trade off significantly with inner core anisotropy. On the other hand, the fit to inner core sensitive modes improves with an increased number of mantle parameters, confirming that mantle structure makes a substantial contribution to the splitting coefficients of these modes.

In general, the models obtained in this section are similar to those of SPRD, with average correlation coefficients of 0.9, 0.8, and 0.7 for shear wave, compressional wave, and density, respectively, between SPR of this section and SPRD from the previous section. To test the characteristic behaviour of bulk sound speed in the lowermost mantle, this model is obtained using the two seismic wave speed models and the reference model PREM. The strong anti-correlation of bulk sound and shear wave speeds still exists at the base of the mantle, even when the model of bulk sound speed is not directly from the inversion. Furthermore, the regional anti-correlation of shear wave and density underneath the central Pacific and Africa at these depths remains one of the best constrained features.

The density models from SPR of this section and SPRD are compared in Figure 3.18(a). The models are similar throughout the mantle as the high correlation coefficient of 0.7 indicates. In the previous study based only upon mantle sensitive modes, the amplitude of the density anomaly was difficult to constrain without the gravity data. Here, gravity data are not included, yet the amplitude of the density model is comparable to or smaller than that of the compressional wave model. In

Figure 3.18: Density Models from the Two Different Mode Data Sets

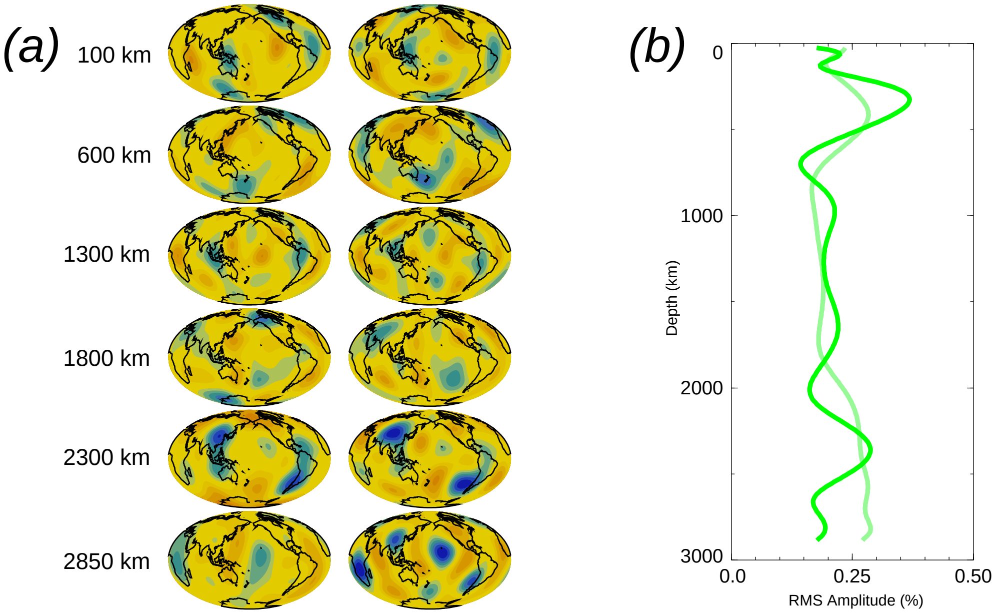

(*a*) Comparison of density models based upon mantle and inner core sensitive modes (left) and SPRD which is constrained only by mantle sensitive modes and gravity data (right). Blue indicates regions where the relative perturbation is higher than average and red indicates values that are lower than average. The scale is fixed at a saturation level of ±1%.
(*b*) Comparison of the RMS amplitude of the density models from SPRD (light green), and SPR of this section (green).

particular, unlike the density model of SPRD, the new model has smaller RMS amplitude near the surface and the core-mantle boundary (Figure 3.18*b*). Small RMS amplitude near the surface is expected from the tectosphere hypothesis, i.e., the density increase due to temperature of the cold cratons is cancelled by chemical effects (e.g., Jordan, 1978; Forte et al., 1995a). It is perceivable that similar cancellation occurs near the core-mantle boundary. As a consequence of low RMS amplitude near the boundaries, the RMS profile as a function of depth contains two peaks: one within the transition zone and another at around 2300 km depth. These characteristics are independent of the radial basis functions used in the inversion.

The choice of Chebyshev polynomials as the radial basis function is somewhat arbitrary, although their gradual variation is consistent with the smoothly varying sensitivity kernels. The disadvantage of global basis functions, such as Chebyshev polynomials, is that the termination of polynomials at some order (in this case, $k_{\max} = 13$) can lead to structure due to "ringing" near the end points (i.e., near the surface and the core-mantle boundary). In what follows, density models are determined using two local basis functions: layers and cubic b-splines (de Boor, 1978; Lancaster & Salkauskas, 1990). In these inversions, the number of unknowns in the radial direction is kept constant (i.e., $k_{\max} = 13$) and both layers and b-spline knots are spaced evenly throughout the mantle. Damping parameters in the radial direction are chosen so that the traces of the resolution matrices (i.e., the number of resolved model parameters) are similar, while keeping damping in the lateral directions the same. The fits to data with local basis functions are then similar to that obtained with Chebyshev polynomials. In general, the observed patterns in the density distribution are compatible between

Figure 3.19: Density Models based upon Various Radial Basis Functions

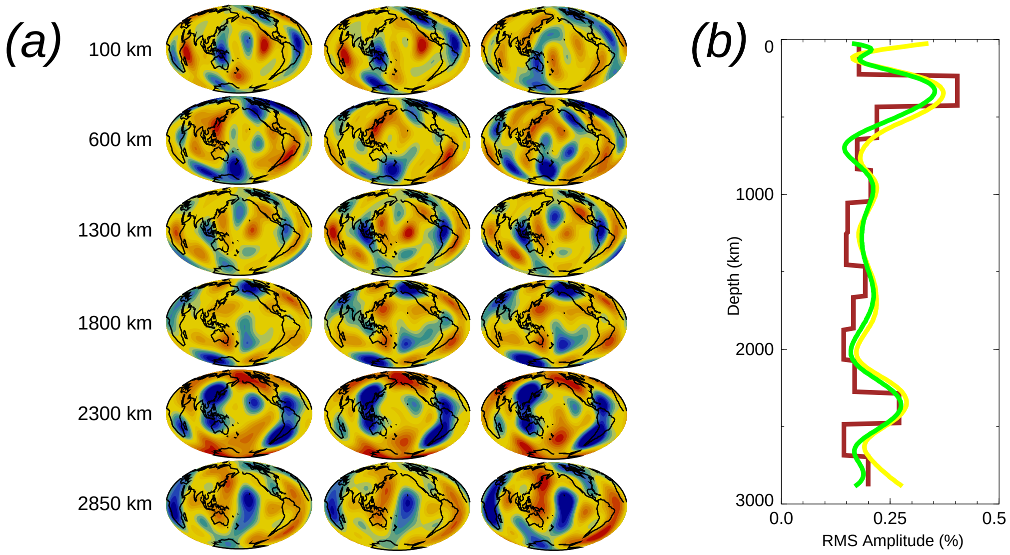

(*a*) Density models using layers (left), Chebyshev polynomials (center), and cubic B-splines (right) at six discrete depths. Blue indicates regions where the relative perturbation is higher than average and red indicates values that are lower than average. The scale is fixed at a saturation level of ±0.5% for all maps.
(*b*) Plot of the RMS amplitudes of density models based upon Chebyshev polynomials (green), cubic B-splines (yellow), and layers (brown) as radial basis functions.

models with different radial bases, including features near the core-mantle boundary (Figure 3.19*a*). The models are least correlated near the surface and the core-mantle boundary, as expected, but the correlation coefficients remain well above the 95% significance level. Furthermore, the radial amplitude profiles of these models are relatively consistent with one another (Figure 3.19*b*). The two peaks in RMS amplitude in the transition zone and around 2300 km depth are present regardless of the choice of basis function or damping scheme, implying that they are robust features and not the results of "ringing".

3.3.2 Robustness of the Models

In the previous section, the question of resolution was investigated in terms of checkerboard and Backus-Gilbert resolution tests, but the resolution of models is most conveniently addressed by looking at the resolution matrix. In Figure 3.20, components of the resolution matrix are shown. Because neither the sensitivity kernels nor the applied damping depend upon angular order t, the resolution for different values of t within the same angular degree is nearly identical. The effect of stronger damping for higher order Chebyshev polynomials is evident, as diagonal elements of the resolution matrix become nearly zero when k is large. In addition, stronger damping on higher spherical harmonic degrees and the compressional wave speed models manifest themselves as poorer resolution of these parameters. Figure 3.20 also shows that there does not appear to be substantial leakage from model to model (indicated by smaller off-diagonal elements in comparison to diagonal components).

Figure 3.20: Resolution Matrix

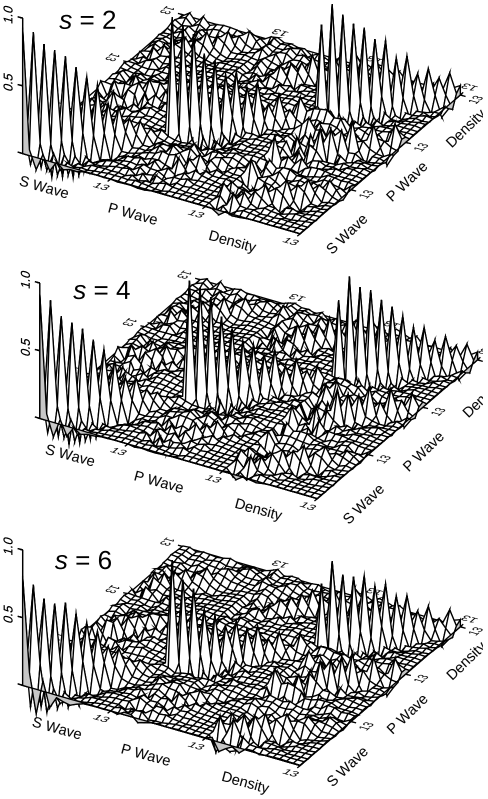

Resolution matrix of the SPR inversion when Chebyshev polynomials are used as the radial basis functions. The elements are arranged by model, shear wave speed (S Wave), compressional wave speed (P Wave), or density (R), and in increasing Chebyshev polynomial order (left to right). Parts of the matrix corresponding to model parameters at degree 2 order 1 (top), degree 4 order 1 (middle), and degree 6 order 1 (bottom).

Figure 3.21: Laterally Varying Scaling Ratios

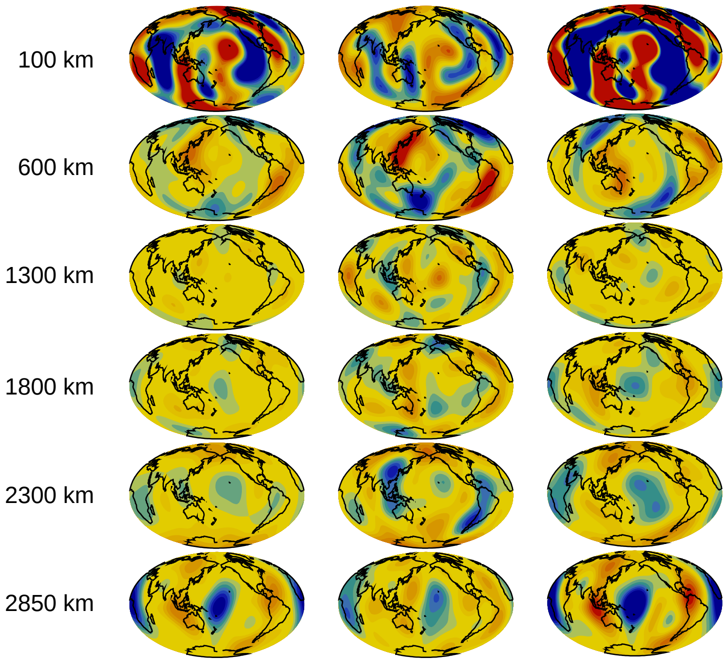

Map views of laterally varying ratios of ν_ρ (left), density to compressional wave speed ν_α (center), and Poisson's ratio (right). Blue indicates regions where the relative perturbation is higher than average and red indicates values that are lower than average. Perturbations from the reference ratio as in PREM (Dziewoński & Anderson, 1981) are shown at 0.05%, 0.02%, and 0.05% levels for the three ratios, respectively.

3.3.3 Laterally Varying Scaling Relationship

In the previous section, it was shown that depth dependent scaling factors between two models are not very useful when models are poorly correlated. Instead of ratios that vary only with radius, one may calculate lateral variations in the scaling ratio to identify anomalous regions. For example, Bolton (1996) notes that beneath the central Pacific, the ratio ν_β is anomalously high in the lowermost mantle. There is, however, a problem. The three-dimensional models represent perturbations from the reference Earth model: there are inevitably regions where the model values are zero, resulting in singularities when a ratio is calculated. To avoid these singularities, lateral variations in the scaling ratio are determined by combining the models with the reference model to obtain the absolute values of velocity and density.

In Figure 3.21, variations in three different ratios are exhibited. The ratios ν_ρ and density to compressional wave speed are generally dominated by the pattern of the seismic wave anomaly since lateral variations in density are weaker (Figure 3.8*c*). Deviations from seismic speed patterns are observed when the correlation between models is low, such as in the transition zone and near the core-mantle boundary.

Another parameter which may be of interest is Poisson's ratio. It describes the ratio of thinning to elongation, or thickening to contraction, and varies between 0.1 and 0.4 for different rocks (Turcotte & Schubert, 1982). In terms of elastic moduli, Poisson's ratio ν_σ is given by $\nu_\sigma = (3\kappa - 2\mu)/(6\kappa + 2\mu)$. This ratio can also be written in terms of the seismic wave speeds as $\nu_\sigma = [(v_P/v_S)^2 - 2]/[2(v_P/v_S)^2 - 2]$, and the distribution of high and low Poisson's ratio obtained from the two seismic models of SPR is illustrated in Figure 3.21. Practically, the pattern of Poisson's ratio is opposite of ν_β, hence laterally varying model of ν_β has been omitted. In general, the various ratios are dominated by the pattern of models with stronger lateral variations. Anomalies associated with superplumes clearly stand out in these plots.

3.4 Discussion and Implications

This Chapter presents results which demonstrates that normal mode data, with or without additional constraints from the Earth's gravity field, can constrain independent even degree lateral variations in seismic wave speeds and density, or, alternatively, elastic moduli and density. The mantle models obtained from the inversion using both mantle and inner core modes do not trade-off significantly with inner core anisotropy, and the improved database supports inversions for seismic wave speeds and density structure with a maximum radial expansion of order 13.

The seismic wave speed models obtained from these data are consistent with existing models based upon body wave data, with the exception in the mid-mantle depth range. This disagreement is mainly due to a relatively small RMS amplitude in the middle mantle. Normal modes provide useful constraint in this region, because some modes are particularly sensitive to structure at this depth range. The models of elastic moduli are well correlated with models of shear and bulk sound speeds, respectively.

One of the main features of the modelling exercise is the introduction of independent density variations. The density RMS amplitude is generally smaller than that of the velocity models, and exhibits two peaks around 600 km and 2300 km depth. Experiments with local radial basis functions demonstrate that the two maxima in the density RMS amplitude are robust, and that the pattern of the density distribution does not depend on the choice of the basis or damping scheme. Contrary to assumptions that density variations can be related to seismic speed variations by a scaling factor, the models are not well correlated in general. The depths of RMS amplitude peaks in the density model correspond with low correlation of density and seismic wave speed variations. Significant de-correlation suggests that lateral heterogeneities in the mantle are not entirely due to variations in temperature. Compositional variations in the transition zone have been suggested previously, for example, based upon the significant de-correlation between topography on the 410-km discontinuity and wave speed at that depth (Flanagan & Shearer, 1999). The most striking observation of the density model appear in the lower-most mantle, where locations of high density anomalies coincide with slow shear wave speed anomalies. Strong global anti-correlation between shear and bulk sound speeds is also observed, further suggesting that compositional, as well as thermal, heterogeneity exists near the core-mantle boundary. This inference is consistent with convection simulations where dense material accumulates beneath upwellings. The lateral flow along the core-mantle boundary collects dense material to these locations, but the material is too heavy to be entrained in the uplift (Christensen, 1984; Davies & Gurnis, 1986; Hansen & Yuen, 1988; Tackley, 1998). Introduction of heavy core material into the mantle beneath upwellings can also produce such density anomalies (Knittle & Jeanloz, 1991).

Chapter 4

Inner Core Anisotropy

4.1 Introduction

Peculiarity of the solid inner core was first reported by Masters & Gilbert (1981) when splitting of inner core sensitive modes were found to exhibit noticeably different pattern from that of mantle modes (Figure 2.1). This observation was soon augmented by measurements of PKIKP arrival times: the travel times depended on the direction of ray propagation (Poupinet et al., 1983). There were four candidates suggested as the cause of these observations. Initially, prolateness of the inner core was offered as the possible source of the anomalous behaviour (Poupinet et al., 1983). However, this shape is dynamically unstable, and analysis of PKiKP indicated that the inner core is elliptical and is close to hydrostatic equilibrium (Rial & Cormier, 1980; Souriau & Souriau, 1989; Roudil & Souriau, 1993). Distribution of heterogeneities, as observed within the mantle, was also proposed, but modelling the inner core with isotropic variations did not provide satisfactory fit to data (Cormier & Choy, 1986).

It was difficult to explain data by placing heterogeneities in the inner core, but putting them in the outer core was more successful, especially for normal mode observations (Ritzwoller et al., 1986, 1988; Widmer et al., 1992). Heterogeneities in the outer core are still championed by some seismologists, both from normal mode and body wave perspectives (e.g., Vasco & Johnson, 1998; Romanowicz & Bréger, 2000; Romanowicz et al., 2003), although there are seismic studies which argue against structure in the outer core (e.g., Roudil & Souriau, 1993). Furthermore, dynamical consideration of a vigorously convecting outer core, generating the magnetic field, predicts heterogeneities that are much below seismically detectable level (Stevenson, 1987).

The final, and most simple, idea was that the inner core was transversely isotropic. In 1986, fifty years after the discovery of the inner core (Lehmann, 1936), observations of both mode and $\mathrm{PKP_{DF}}$ travel times were shown to be compatible with transversely isotropic inner core (Morelli et al., 1986; Woodhouse et al., 1986). Analysis of differential travel times confirmed this result (Shearer & Toy, 1991; Creager, 1992), and fit to various inner core modes with anisotropy (Tromp, 1993) convincingly demonstrated that the source of anomalous observations associated with the inner core is indeed transverse isotropy.

Subsequent investigations produced a wide range of transverse isotropy models, some of which are illustrated in Figure 4.1. The models depend strongly on the kind of data used in the analysis. Those based upon normal mode observations tend to prefer stronger anisotropy near the inner core boundary than in central inner core (e.g., Woodhouse et al., 1986; Tromp, 1993). This trend is not consistent with inferences based upon body waves, which prefer anisotropy that is generally stronger, especially near the centre of the Earth (e.g., Vinnik et al., 1994; Su & Dziewoński, 1995; McSweeney et al., 1997; Ouzounis & Creager, 2001; Song & Xu, 2002), and a very weakly anisotropic (e.g., Shearer et al., 1988; Creager, 2000) or even isotropic (e.g., Song & Helmberger, 1995; Ouzounis &

Figure 4.1: Various Models of Inner Core Anisotropy

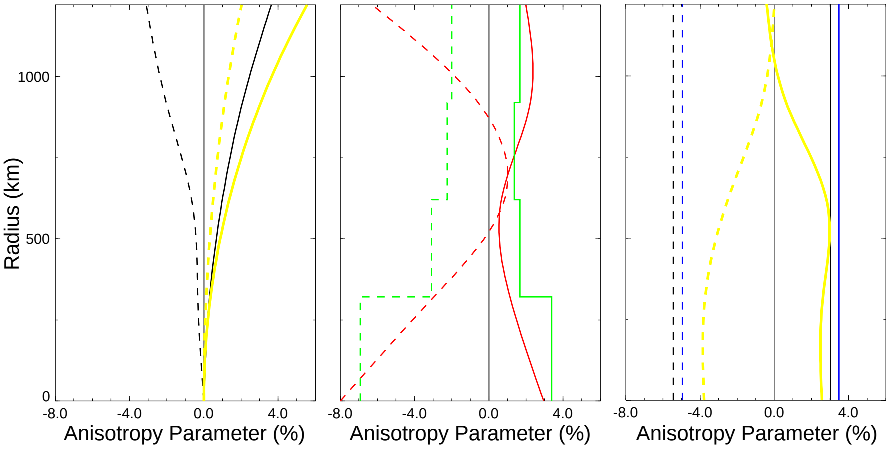

Different inner core anisotropy models are presented in terms of ϵ (solid) and σ (dashed), where they are grouped by data used in the inversion: normal modes (left), absolute travel times (centre), and differential travel times (right). Note that Tromp (1995a) model uses both normal mode and absolute travel times. Colours indicate different studies, Woodhouse et al. (1986; yellow in the left panel), Tromp (1993; black in the left panel), Su & Dziewoński (1995; green), Tromp (1995a; red), Creager(1992; blue), Song & Helmberger (1993; black in the right panel), and McSweeney et al. (1997; yellow in the right panel). The grey line is the zero line.

Creager, 2001; Song & Xu, 2002) layer near the inner core boundary. Romanowicz et al. (1996) have combined differential travel time and normal mode data in their inversion for the inner core, however, their results are strongly controlled by the differential travel times which may contain considerable signal from regions outside the inner core. In order to derive a model that is compatible with a suite of inner core sensitive data, analysis presented in this Chapter simultaneously fits normal mode splitting functions, absolute and differential travel times. Taking advantage of the sensitivity of normal mode data to the inner core as a whole, a simple global model of the inner core is sought for. In addition, a study of body wave data are presented to test whether the data set can constrain more complex structure in the inner core, such as hemispheric variations in anisotropy as suggested by some differential travel time studies (e.g., Tanaka & Hamaguchi, 1997; Creager, 1999; Niu & Wen, 2001).

4.1.1 Radial Basis Function

The choice of radial basis functions for the inner core must meet certain conditions. The bottom-most point in the inner core corresponds to the centre of the Earth, so the radial basis function should be continuous and smoothly varying at this point. Chebyshev and Legendre polynomials, commonly used in mantle models, give a cusp (i.e., a discontinuity in the first derivative) at the centre if any odd degree terms are non-zero. There are 3 other choices for popularly used basis functions in the inner core; cubic b-splines (e.g., Tromp, 1993, 1995a; McSweeney et al., 1997), layers (e.g., Su & Dziewoński, 1995) and even degree polynomials in radius (e.g., Dziewoński & Anderson, 1981; Morelli et al., 1986; Woodhouse et al., 1986). The choice of cubic b-splines is not optimal. In order to impose a smooth variation at the centre of the Earth, all splines near the centre must have the same value or the inner-most spline must vanish, i.e., anisotropy at the centre of the Earth must be zero. The anisotropy at the centre can be finite. For example, if the inner core is a single crystal,

Table 4.1: Models of Anisotropy with Different Mantle Parametrisations and Starting Models

Model	α	γ	β	ϵ	σ
S	3.6	0.93	0.95	1.8	-0.80
SP	3.8	0.83	0.99	1.9	-0.74
SPR(R)	3.5	0.88	0.99	1.8	-0.66
SPR(S)	3.5	0.88	0.99	1.8	-0.66

The values of α, γ, and β in percent for constant anisotropy within the inner core are compared with different parametrisations of the mantle as defined in the previous Chapter. "R" and "S" in brackets indicate that the starting density model is that of SPRD (Ishii & Tromp, 2001) and scaled SKS12WM13 (Dziewoński et al., 1997), respectively. The values of α, γ, and β are converted to ϵ and σ assuming that the term $A_0/(\rho v_P^2)$ in equation (2.2) is unity.

there will be non-zero anisotropy. Furthermore, this parametrisation requires a minimum of 3 splines within the inner core even for constant anisotropy. Therefore, inner core models considered in this Chapter use either even degree polynomials or layers as basis functions. Even degree polynomials are preferred over layers, because the latter introduces artificial discontinuities which may lead to erroneous interpretations.

4.1.2 Inner Core Anisotropy and Mantle Heterogeneity

There is surprisingly little variation in the values of the anisotropic parameters when the mantle parametrisation is changed (Table 4.1). This is a consequence of the consistency of the zonal components of compressional wave speed and density within the mantle. The low frequency inner core modes possess substantial sensitivity to these two variations, but the amplitudes of the zonal components for compressional wave and density of the SP or the SPR models are similar to a scaled shear wave model throughout the mantle. Under the assumption that the symmetry axis of anisotropy is aligned with the rotation axis, only zonal terms at degrees 2 and 4 constrain inner core anisotropy (equation 2.11). Hence the inner core models are relatively insensitive to mantle parametrisation. For referencing purposes, the inner core model obtained with an SPR parameterization for the mantle is denoted as SPRI0.

4.2 Constant Anisotropy

The previous discussion already showed some results for inner core anisotropy that does not vary with radius. In this section, the constant model is analysed in detail: changes with different weights on various types of data, data fits, and uncertainties of the model values.

4.2.1 Models

There are four different types of data (mode, $\mathrm{PKP_{DF}}$, $\mathrm{PKP_{BC}}-\mathrm{PKP_{DF}}$, and $\mathrm{PKP_{AB}}-\mathrm{PKP_{DF}}$) in the inversion which are not necessarily compatible with one another, and it is important to understand the effects of relative weighting on different data subsets. Table 4.2 summarises the results of inversions with various weighting schemes. Regardless of how the absolute travel time data are weighted with respect to normal modes, when a good fit is achieved for $\mathrm{PKP_{DF}}$, the model also explain the mode data. This result indicates that these two data sets are highly compatible. In fact, this consistency is so robust that even an inner core model obtained from an inversion with only normal mode data can fit the absolute travel times.

Table 4.2: Inversion Results with Different Data Weighting

	Variance Reduction				Model Parameters				
ω	IC	DF	BC	AB	α	γ	β	ϵ	σ
1	83	85	71	74	3.5	0.88	0.99	1.7	-0.65
10	83	85	71	75	3.5	1.0	0.93	1.7	-0.85
100	70	79	77	78	4.2	1.1	0.58	2.1	-2.0
1000	66	35	84	84	5.5	1.3	-0.098	2.8	-4.2
$10^\dagger$	83	85	69	73	3.4	0.97	0.99	1.7	-0.67
$100^\dagger$	83	85	66	73	2.9	1.3	0.97	1.5	-0.83
$1000^\dagger$	82	85	67	73	2.9	1.5	0.85	1.4	-1.3

Fit to various data and models obtained from inversions with different body wave data weighting with respect to normal mode data (ω). The variance reductions for inner core sensitive modes, $\mathrm{PKP_{DF}}$, $\mathrm{PKP_{BC}}-\mathrm{PKP_{DF}}$, and $\mathrm{PKP_{AB}}-\mathrm{PKP_{DF}}$ are denoted by IC, DF, BC, and AB, respectively. The relative weighting of mode, $\mathrm{PKP_{DF}}$, $\mathrm{PKP_{BC}}-\mathrm{PKP_{DF}}$, and $\mathrm{PKP_{AB}}-\mathrm{PKP_{DF}}$ are prescribed to be 1:2ω:2ω:ω (values of ω without †) or 1:2ω:2:1 (ω with †). $\omega = 1$ corresponds to SPRI0. Both variance reduction and model values are in percent. Values of ϵ and σ have been determined assuming that the $A_0/(\rho v_P^2)$ term in equation (2.2) is unity.

However, satisfying differential travel time data at the same time as $\mathrm{PKP_{DF}}$ or normal mode data is more difficult. Changing the weighting on body waves improves the differential travel time fit, but the fit to mode and absolute travel time data degrades. In general, differential data (and $\mathrm{PKP_{DF}}$ data to some extent) prefer to have higher values of α and γ and lower values of β than those determined by normal mode data, translating to higher values of ϵ and significantly lower values of σ. If $\sim$ 75% variance reduction is required for the differential data, the model values ϵ and σ are 2.2% and -2.2%, respectively, in contrast to 1.7% and -0.65%, in SPRI0 where the two types of differential data are fit to 70% and 74%. The models obtained with heavier weights on body wave data are more consistent with previous models derived from differential travel time measurements alone. For example, the model of Creager (1992) has $\epsilon = 3.48\%$ and $\sigma = -4.95\%$ which reduces variance in $\mathrm{PKP_{BC}}-\mathrm{PKP_{DF}}$ data by more than 85%. Requiring an $\sim$ 85% fit to differential data in the joint inversion gives results which are compatible with Creager's estimates, $\epsilon = 2.9\%$ and $\sigma = -4.6\%$. However, such requirements reduce the fit to normal mode and $\mathrm{PKP_{DF}}$ data significantly. With a $\sim$ 75% fit to differential data, the fits to the modes and $\mathrm{PKP_{DF}}$ are 70% and 78%, respectively. Because normal mode data constrain global anisotropy, and because there are reasons to believe that differential travel time data are biased or contaminated (detailed arguments are presented section 4.5 and 4.6.2), SPRI0 is chosen as the preferred model.

The fits achieved by model SPRI0 for inner core sensitive modes is 83% variance reduction whereas when mantle models from SPRI0 and inner core model of Tromp (1995a) or Creager (1992) is used, the variance reduction becomes 69% or 20%, respectively. Note that for the calculation of variance reduction using the model of Creager (1992), γ was assumed to be 1.0%. The fits to travel time data using these three models are illustrated in Figure 4.2 and Figure 4.3. The model SPRI0 achieves 85%, 71%, and 74% variance reduction to $\mathrm{PKP_{DF}}$, $\mathrm{PKP_{BC}}-\mathrm{PKP_{DF}}$, and $\mathrm{PKP_{AB}}-\mathrm{PKP_{DF}}$ data, respectively. In comparison, the model of Tromp (1995a) gives 82%, 79%, and 76%. This model is not constant in radius (uses 5 radial basis functions, i.e., there are 15 model parameters), nonetheless the fits are similar to those of SPRI0 whose model vector consists only of 3 elements. In contrast, the model of Creager (1992) over-predicts $\mathrm{PKP_{DF}}$ data for rays penetrating deeply into the inner core (resulting in negative variance reduction for this data set), but fits the large anomalies in $\mathrm{PKP_{BC}}-\mathrm{PKP_{DF}}$ and $\mathrm{PKP_{AB}}-\mathrm{PKP_{DF}}$, giving variance reduction greater than 85%.

Figure 4.2: Fit to Absolute Travel Time Data

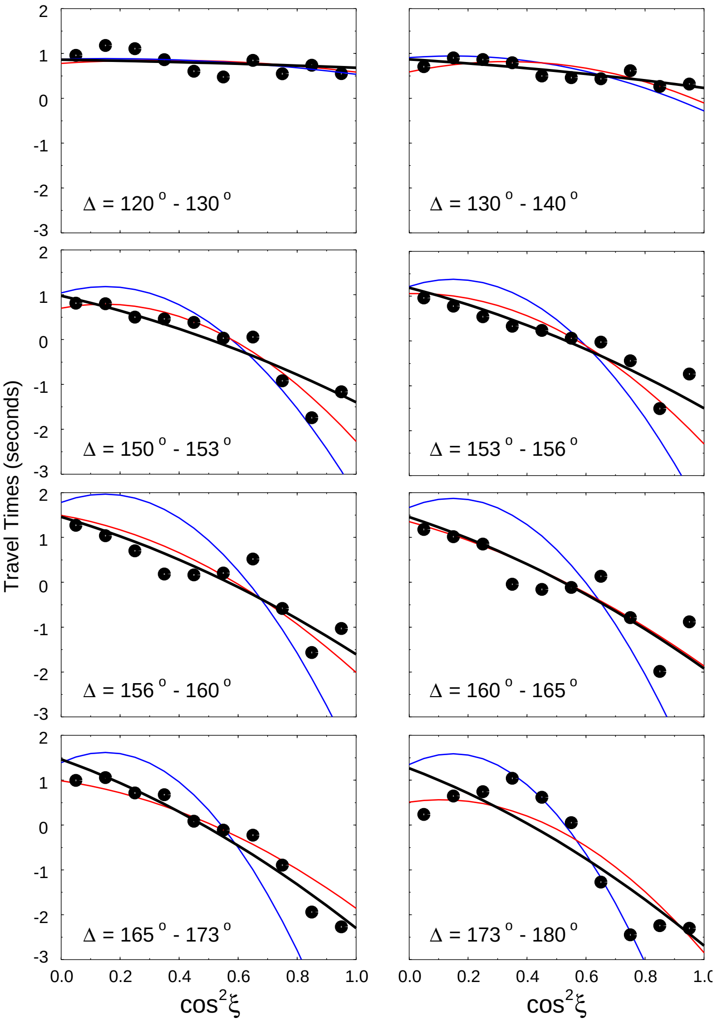

Plots of $\mathrm{PKP_{DF}}$ data (black circles) at different distance ranges, and predictions based upon various models. Black curve is from the constant model SPRI0, the red curve is the depth dependent model of Tromp (1995a), and the blue curve is a constant anisotropy model of Creager (1992). The model of Tromp (1995a) fits the $\mathrm{PKP_{DF}}$ data with a variance reduction of 82%, but the strongly anisotropic model of Creager (1992) over-predicts the data trend (variance reduction of -15%).

Figure 4.3: Fit to Differential Travel Time Data

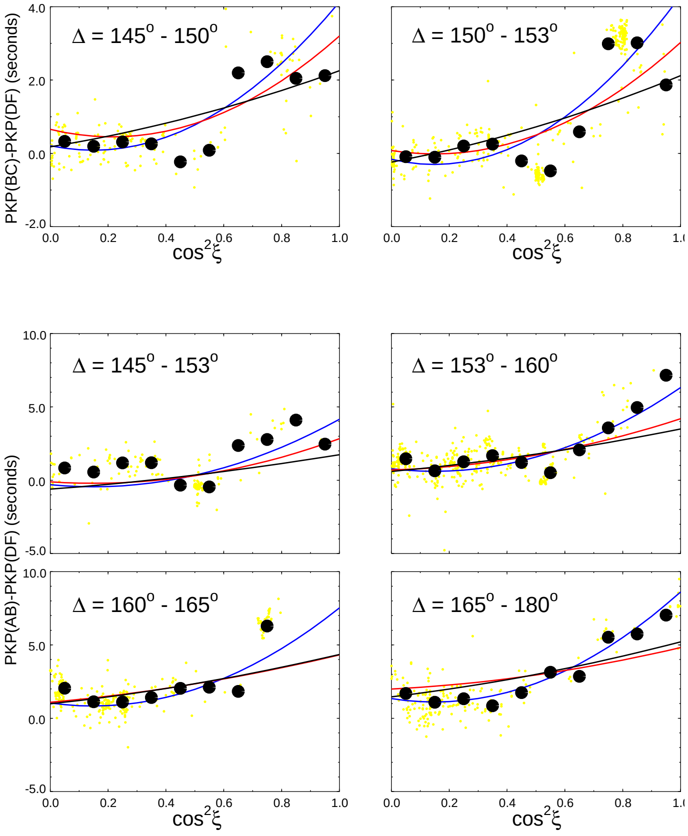

Plot of averaged differential data (black circles) at different distance ranges and predictions based upon the constant anisotropy model SPRI0 (black curve), and models of Tromp (1995a) (red curve), and Creager (1992) (blue curve). The background yellow dots are individual measurements.

Table 4.3: Volumetrically Averaged Inner Core Anisotropic Parameters

Source	$<\alpha>$	$<\gamma>$	$<\beta>$	$<\epsilon>$	$<\sigma>$
Morelli et al. (1986)				1.92	−3.84
Woodhouse et al. (1986)	6.7	−2.7	0.70	3.49	0.781
Shearer et al. (1988)				0.971	−1.73
Shearer & Toy (1991)				0.615	−0.507
Creager (1992)				3.48	−4.95
Song & Helmberger (1993)				3.02	−5.44
Tromp (1993)	4.21	2.33	1.27	2.21	−1.99
Su & Dziewoński (ICA4A) (1995)				1.62	−2.29
Su & Dziewoński (ICA4B) (1995)				1.90	−3.03
Tromp (1995a)	3.55	1.43	0.675	1.86	−1.97
McSweeney et al. (1997)				0.823	−0.965
Durek & Romanowicz (1999)[a]	5.0	−0.5	0.8	2.5	−0.4
SPRI0	3.49	0.881	0.988	1.82	−0.67

Summary of selected models of the inner core. Model values have been volumetrically averaged (denoted by $<\cdot>$) and are in percent.

[a] The values are based upon equations (16) through (18) of Durek & Romanowicz (1999). Note that there is a sign error in equations (16) and (17).

The values of α, γ, and β, and/or ϵ and σ obtained from various research groups based upon different data are compared and summarised in Table 4.3. Many of the models in this table are depth dependent, so the model values have been averaged volumetrically in order to facilitate comparison with SPRI0. The three anisotropic parameters, α, γ, and β cannot be obtained independently in body wave studies, so direct comparisons of these parameters can be made only with previous normal mode studies. Using splitting function measurements for 7 modes, Woodhouse et al. (1986) derived two models of inner core anisotropy, a constant model and a model with an r^2 dependence (where r is radius). The constant model shown in Table 4.3 has stronger anisotropy than SPRI0, but this may be due to uncorrected mantle effects. The volumetric averages of Tromp (1993, 1995a) are similar to those from this study, although Tromp (1993, 1995a) models vary strongly with radius. The values of ϵ and σ derived from the set of α, γ and β can be compared to results from body wave studies. In general, the parameter σ shows large variations from one study to another, but the agreement for ϵ is better. As demonstrated in the next section, the parameter σ is poorly constrained compared to ϵ. As expected, SPRI0 value for ϵ is in good agreement with studies based upon either normal mode data (Tromp, 1993, 1995a) or absolute travel times (Morelli et al., 1986; Su & Dziewoński, 1995).

4.2.2 Robustness

Unlike mantle modelling, the number of model parameters is small for the inner core. The limited number of model elements allows for detailed monitoring of how an individual parameter changes with respect to others while studying how they change with different subsets of data. Therefore the uncertainties associated with each model parameter is assessed using a Monte-Carlo method.

A Monte-Carlo simulation is often used to estimate the uncertainties associated with model parameters (Huber, 1981). The numbers of splitting function coefficients, $\mathrm{PKP}_{\mathrm{DF}}$, $\mathrm{PKP}_{\mathrm{BC}}-\mathrm{PKP}_{\mathrm{DF}}$ and $\mathrm{PKP}_{\mathrm{AB}}-\mathrm{PKP}_{\mathrm{DF}}$ used in the inversion are fixed, but a new data set is defined by randomly picking each datum from the original database, allowing for multiple inclusions. This method replaces approximately 37% of the original data by duplicated data (Press et al., 1992). Variations in model parameters obtained from inversions of such data sets are then associated with uncertainties of

Figure 4.4: Variations in ϵ and σ

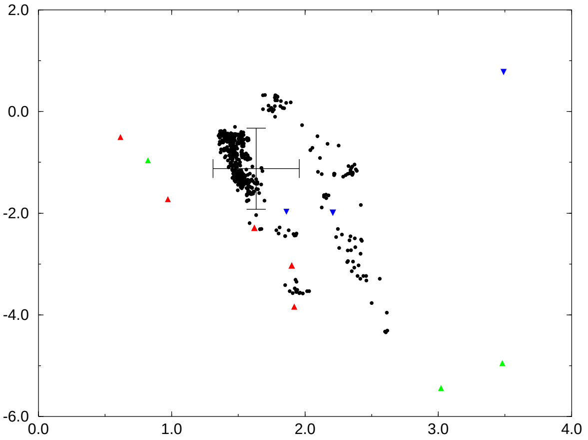

Values of ϵ (x-axis) and σ (y-axis) obtained from Monte-Carlo inversions (black dots) plotted against one another. The black cross indicates the average values of ϵ and σ with one standard deviation. For comparison, volumetric average values of ϵ and σ from normal mode studies are shown by blue triangles, those from absolute travel time studies are shown by red triangles, and those from differential travel times studies are shown by green triangles.

individual parameter. About 600 inversions are performed, and the averages of the parameters α, γ, and β are 3.1, 0.76, and 0.62, respectively, with standard deviation of 0.62, 0.33, and 0.31, respectively. Consequently, ϵ and σ take values of 1.6 and -1.1 with standard deviation of 0.32 and 0.79, respectively. These standard deviations illustrate that α and ϵ are better constrained with the data than other parameters, especially σ.

The frequency distribution of parameter values is skewed, so the standard deviation should be considered only as a guide to the model uncertainty. For example, 80% of the σ values obtained from the Monte-Carlo method lie between -1.5 and -0.14. The skewness is more pronounced for ϵ, where 80% of the results are found between 1.4 and 2.0. Values below 1.4 do not exist, but values above 1.7 constitute a relatively long tail. This distribution indicates that ϵ has a distinct minimum and it must be greater than 1.4 to satisfy the data set.

When the parameters are plotted in ϵ-σ space, many of the results lie along a straight line, with a correlation coefficient of -0.86 (Figure 4.4). This observation suggests that there is a trade off between model parameters, which is unavoidable in under-determined inverse problems. It is interesting to note that most of the volumetrically averaged values of ϵ and σ from various studies (Table 4.3) plot along the straight line ($\sigma \sim -3\epsilon + 4$). There are some deviants such as Woodhouse et al. (1986), Shearer et al. (1988), Shearer & Toy (1991), and McSweeney et al. (1997), but there is no distinction between models based upon modes, absolute or differential travel times.

4.3 Radially Varying Anisotropy

Radial variation in anisotropy is introduced by using more than one radial basis function or by an *a priori* condition. In the inversions, model smoothness is not imposed in the radial direction, i.e., polynomials are damped equally regardless of its order. In general, increasing the number of radial parameters does not improve the fit if only normal mode data are used in the inversions.

Table 4.4: Radially Dependent Models of Inner Core Anisotropy

$p_{\max}$	VR(DF)	VR(BC)	VR(AB)	VR(IC)	$< \alpha >$	$< \gamma >$	$< \beta >$
0	85	71	74	83	3.5	0.88	0.99
1	84	72	73	83	3.3	0.60	1.2
2	84	71	72	83	3.2	0.59	1.2
3	84	70	72	83	3.2	0.60	1.2

Summary of statistical results from inversions with different maximum radial expansions ($p_{\max}$) within the inner core. $p_{\max} = 0$ is for constant anisotropy (corresponding to the model SPRI0). The parameters $< \alpha >$, $< \gamma >$, and $< \beta >$ are volumetrically averaged values of α, γ, and β in percent.

The additional degrees of freedom do improve the fit to body wave data, although it is difficult to improve fits to both $\mathrm{PKP_{DF}}$ and differential travel time data simultaneously.

4.3.1 Models

Table 4.4 summarises the statistical results for radially varying anisotropic models of the inner core. Note that fits do not necessarily improve with an increase in the number of parameters for all data. For example, allowing quadratic variations with radius improves the fits to differential travel times, but not to $\mathrm{PKP_{DF}}$ data. Introduction of variations in the radial direction is barely warranted by data, i.e., $\chi^2/(N-M)$ decreases only when it is considered to three significant digits. The only obvious modification occurs when a quadratic term is added to the constant term. As such, the radial profiles do not change significantly between models using 2 polynomials (Figure 4.5 left panel) and 4 polynomials (Figure 4.5 right panel). Table 4.4 also gives values of volumetrically averaged α, γ, and β which do not change much with increasing number of radial polynomials.

If the weighting for body wave data is increased, it is possible, with the extra degrees of freedom in the radial direction, to fit $\mathrm{PKP_{BC}}-\mathrm{PKP_{DF}}$ data with a variance reduction of more than 80% while maintaining a good fit to modal and $\mathrm{PKP_{DF}}$ data. For example, increasing the weight on the differential travel times by a factor of 40 in a quadratically parametrised inner core inversion achieves variance reductions of 81%, 81%, 76%, and 82% for $\mathrm{PKP_{DF}}$, $\mathrm{PKP_{BC}}-\mathrm{PKP_{DF}}$, $\mathrm{PKP_{AB}}-\mathrm{PKP_{DF}}$, and inner core sensitive modes, respectively. In general, the choice of weighting does change the values of anisotropic parameters, but the relative shape of the radial profiles remains the same. For example, the above model, which fits differential travel times, has volumetrically averaged values of 3.7, 0.65, and 0.82 for α, γ and β, compared to the values 3.3, 0.60, and 1.2 obtained with the weighting scheme used for the models in Table 4.4. However the profiles in these two cases appear the same, with a slight overall shift in the values.

As discussed in the Introduction to this Chapter, layered basis functions are avoided, because such a parametrisation introduces artificial discontinuities. To illustrate this problem, two parameter models using even degree polynomials and layers are compared in Figure 4.6. The position of the layer interface is determined through a systematic search for the best fit to differential data. This results in slightly better fits for layered models (80%, 76%, 77%, and 84% variance reduction for $\mathrm{PKP_{DF}}$, $\mathrm{PKP_{BC}}-\mathrm{PKP_{DF}}$, $\mathrm{PKP_{AB}}-\mathrm{PKP_{DF}}$, and inner core modes, respectively) than polynomial models with the same number of unknowns, although the difference is not significant. However, the models as a function of depth look drastically different. Polynomial models give anisotropy that is smoothly varying, especially for the well determined parameters (α or ϵ, and β to some extent). In contrast, layered models change considerably from one layer to another. Although both types of models explain the observed signals, the interpretation of inner core properties based upon the two models might be quite different. For example, a large jump at the middle of the inner core in layer models might be taken as evidence for a transition zone. In the central portions of the inner core,

Figure 4.5: Radially Varying Models with Polynomial Basis Function

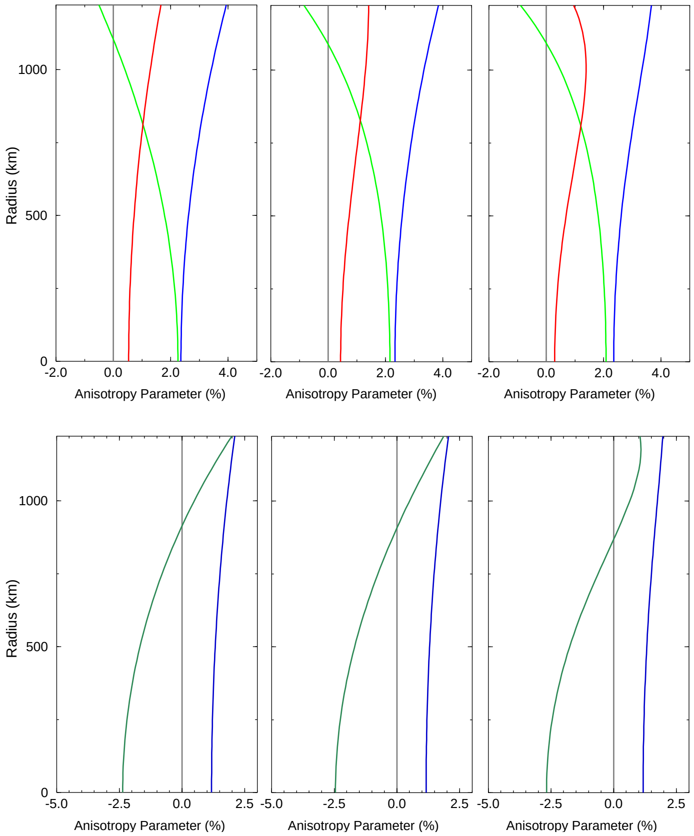

Models of radially dependent inner core anisotropy for two (left), three (centre), and four parameter (right) expansions. The top panel shows the three parameters α (blue), γ (green), and β (red). The same models in terms of ϵ (dark blue) and σ (dark green) are shown in the lower panels. The grey line is the zero line.

Figure 4.6: Models with Layer and Polynomial Radial Basis Functions

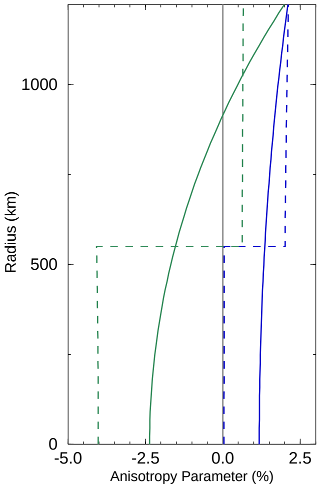

Comparison of models with two degrees of freedom in the radial direction (two layers and quadratic polynomials). The the profiles of ϵ (dark blue) and the σ (dark green) are shown for polynomial basis (solid curves) and layers (dashed lines).

the two parametrisations also yield different results. Layered models suggest that anisotropy is very weak, even close to zero, whereas polynomial models suggest that the anisotropy is weaker at the centre compared to shallower depths, but it remains non-zero.

4.3.2 Isotropic Layer Near the Inner Core Boundary

There have been suggestions that anisotropy in the inner core is weak in the top 50–300 km (e.g., Shearer, 1994; Song & Helmberger, 1995; Creager, 2000), or that this region is isotropic (e.g., Song & Helmberger, 1998). To investigate if the hypothesis of an isotropic layer is compatible with mode and $\mathrm{PKP_{DF}}$ data, inversions are performed in which an isotropic layer of varying thickness is imposed near the inner core boundary. The fit to the mode data and the values of anisotropic parameters as a function of the thickness of the isotropic layer are shown in Figure 4.7. The fit improves marginally as the thickness is increased to about 100 km, although the improvement is not significant. A significant drop in variance reduction starts around 150 km. Normal mode data appear to be consistent with an isotropic layer up to about 150 km thickness, in agreement with an observation of Durek & Romanowicz (1999).

The fit to $\mathrm{PKP_{AB}}-\mathrm{PKP_{DF}}$ and $\mathrm{PKP_{DF}}$ at large epicentral distances change only slightly with the introduction of an isotropic layer and is highly compatible with a layer as thick as $\sim$ 150 km from the inner core boundary. Their sensitivity to shallow structure is small, and the fit is achieved by increased strength of anisotropy in the deeper part. However, $\mathrm{PKP_{DF}}$ data at an epicentral distance range less than 153°, i.e., data most sensitive to shallowest inner core, exhibit a rapid decrease in variance reduction with increasing isotropic layer. Moreover, the introduction of an isotropic layer immediately decreases the variance reduction of $\mathrm{PKP_{BC}}-\mathrm{PKP_{DF}}$ data and the fit degrades rapidly when the thickness is more than $\sim$ 30 km. The degradation of fit contradicts previous differential travel time studies, but it is due to normal mode constraint: modes do not allow for increase in interior anisotropy as quickly as required by differential travel time data (Figure 4.7).

These observations are robust and they do not depend upon the maximum number of radial polynomials or the type of basis functions used. Therefore the existence of an isotropic layer near the

Figure 4.7: Isotropic Layer near the Inner-Core Boundary

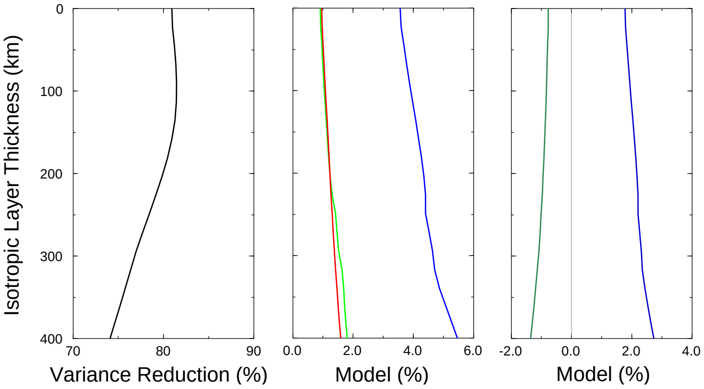

Fit to splitting function coefficients of inner core modes as a function of the thickness of the isotropic layer from the inner core boundary (left). The inversion assumes constant anisotropy below the isotropic layer. The values of the anisotropic parameters, α (blue), γ (green), β (red), ϵ (dark blue), and σ (dark green) beneath the isotropic layer are shown in the central and right panels.

inner core boundary is not warranted by a joint inversion of mode and travel time data. This result should be compatible with data from which inferences of isotropic layer have been made. Shearer's study (1994) rejected a high (3.5%) level of anisotropy using absolute travel time data at short distances (132° to 140°). This observation appears to have been mis-interpreted as an argument for an isotropic layer near the inner core boundary (Song & Helmberger, 1998). Inspection of Shearer's data set shows that the global anisotropy model SPRI0 gives a satisfactory fit (Figure 4.8). In addition, none-zero anisotropy near the inner core boundary is not inconsistent with differential travel time data as it may appear at first. Although isotropy is strongly advocated, differential travel times do not rule out the presence of weak ($\sim 1\%$) anisotropy near the inner core boundary (e.g., Song & Helmberger, 1995; Creager, 2000; Garcia & Souriau, 2000). There is another evidence for finite anisotropy near the inner core boundary: differential travel times using diffracted $\mathrm{PKP}_{\mathrm{BC}}$.

Diffracted $\mathrm{PKP}_{\mathrm{BC}}-\mathrm{PKP}_{\mathrm{DF}}$ Data

Because $\mathrm{PKP}_{\mathrm{BC}}-\mathrm{PKP}_{\mathrm{DF}}$ measurements at distance greater than $\sim 153°$ use diffracted $\mathrm{PKP}_{\mathrm{BC}}$ according to PREM (Dziewoński & Anderson, 1981), these data have not been included in the inner core study. Diffracted $\mathrm{PKP}_{\mathrm{BC}}$ travels along the inner core boundary and would be most sensitive to the shallowest part of the inner core. The measurements of $\mathrm{PKP}^{\mathrm{diff}}_{\mathrm{BC}}-\mathrm{PKP}_{\mathrm{DF}}$ from the 153° to 155° distance range are compared with $\mathrm{PKP}_{\mathrm{BC}}-\mathrm{PKP}_{\mathrm{DF}}$ data at shorter distance ranges (150°–153°) in Figure 4.9. The diffracted data are generally smaller (closer to zero) than $\mathrm{PKP}_{\mathrm{BC}}-\mathrm{PKP}_{\mathrm{DF}}$, except when $\cos^2\xi = 0.85$. Furthermore, they have a smaller slope and curvature as a function of $\cos^2\xi$, indicating that integrated anisotropy sensed by this data set is weaker than that from $\mathrm{PKP}_{\mathrm{BC}}-\mathrm{PKP}_{\mathrm{DF}}$ from a smaller distance range. This is even more evident when the anomalous path from South Sandwich Islands to Alaska is omitted (Figure 4.9*b*).

The average bottoming depth for $\mathrm{PKP}_{\mathrm{DF}}$ in the distance range from 150° to 153° is 250 km, and it is 285 km for data in the range 153° to 155°. If the shallowest part of the inner core is isotropic, then diffracted $\mathrm{PKP}_{\mathrm{BC}}$ would obtain no directional dependence and $\mathrm{PKP}^{\mathrm{diff}}_{\mathrm{BC}}-\mathrm{PKP}_{\mathrm{DF}}$ data from 153° to 155° should have compatible or larger travel time anomalies than $\mathrm{PKP}_{\mathrm{BC}}-\mathrm{PKP}_{\mathrm{DF}}$ from 150° to 153°. A drastic change in anisotropy in the incremental 35 km radius (e.g., negative anisotropy) may allow smaller anomalies for diffracted data, but inversions with layered inner core anisotropy

Figure 4.8: Absolute Travel Times from Small Distance Range

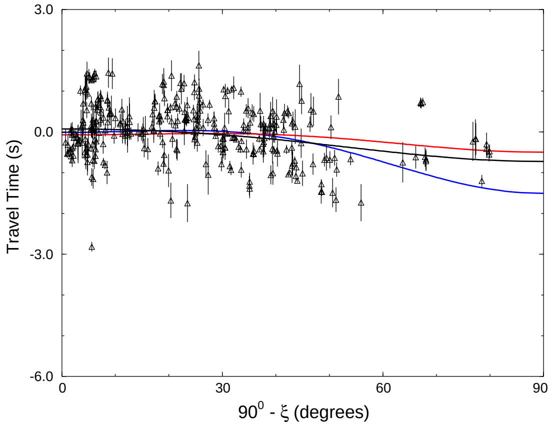

ISC summary ray residuals for the distance range 132° to 140°. The residuals are plotted as a function of $90° - \xi$ rather than $\cos^2 \xi$ to ease comparison with Figure 9 of Shearer (1994). The standard deviation associated with each datum is shown as a vertical bar. Predictions based upon models from Shearer et al. (1988; red curve), Creager (1992; blue curve), and SPRI0 (black curve) are shown. Note that the strong anisotropy in Creager's model overpredicts residuals at high values of ξ. Data courtesy of P. Shearer.

Figure 4.9: Diffracted $\mathrm{PKP_{BC}}-\mathrm{PKP_{DF}}$ Travel Time Data

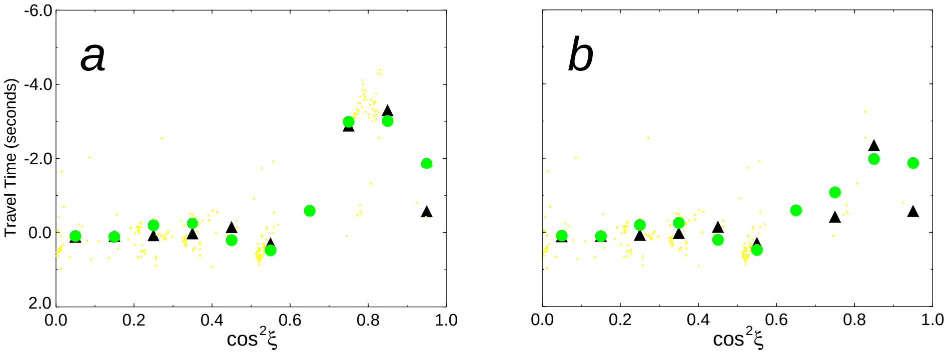

(a) Comparison of $\mathrm{PKP_{BC}}-\mathrm{PKP_{DF}}$ data from 150° to 153° (black triangles) and $\mathrm{PKP_{BC}^{diff}}-\mathrm{PKP_{DF}}$ data from 153° to 155° (green circles). The yellow dots in the background are individual measurements of $\mathrm{PKP_{BC}^{diff}}-\mathrm{PKP_{DF}}$. Most $\mathrm{PKP_{BC}^{diff}}-\mathrm{PKP_{DF}}$ data (209 measurements out of 339) are in this distance range.

(b) Same as in (a), except that the anomalous path from South Sandwich Islands to Alaska has been removed.

or other differential travel time studies do not document such a change. This evidence suggests that the missing signal of anisotropy in $\mathrm{PKP}_{\mathrm{BC}}^{\mathrm{diff}}-\mathrm{PKP}_{\mathrm{DF}}$ is due to the $\mathrm{PKP}_{\mathrm{BC}}^{\mathrm{diff}}$ sampling the uppermost part of the inner core. The evanescent wave does not penetrate deeply into the inner core, but the accumulation of signal along approximately 50 km of the inner core boundary will be significant, and comparable to the signal observed in the 120° to 130° distance range. It appears that anisotropy near the inner core boundary is also required in order to explain the small values of $\mathrm{PKP}_{\mathrm{BC}}^{\mathrm{diff}}-\mathrm{PKP}_{\mathrm{DF}}$ data.

4.4 Hemispherically Varying Anisotropy

Several studies have suggested that anisotropy of the inner core have an east-west hemispherical dependence (e.g., Tanaka & Hamaguchi, 1997; Creager, 1999; Niu & Wen, 2001). The normal mode data are insensitive to such hemispherical difference, since this pattern corresponds to structure at spherical harmonic degree one. Therefore, the focus of this section will be on the body wave data which are divided into subsets based upon their bottoming points for detecting lateral variations in anisotropy. The eastern and western hemisphere data show a clear difference, but such dichotomy is also observed when the inner core is divided into the northern and southern hemispheres. Finally, geometrical argument is presented which suggests that the apparent hemispheric anomalies result from a small number of travel time measurements, and much of the data can be explained by the constant anisotropy model.

4.4.1 Data Analysis

Although investigations of hemispheric dependence of anisotropy concentrated on an east-west difference (e.g., Tanaka & Hamaguchi, 1997; Creager, 1999; Niu & Wen, 2001), the division of the inner core into eastern and western hemispheres is not the only way in which one can obtain subsets with distinct behaviour. This effect is demonstrated by separating data according to whether they bottom in the northern or southern hemispheres. Regardless of the definition of hemisphere, a clear difference between hemispheres is observed for $\mathrm{PKP}_{\mathrm{DF}}$ data (Figures 4.10*a* and *b*). The hemispheric subsets of $\mathrm{PKP}_{\mathrm{DF}}$ agree well with one another in the distance range from 120° to 140°, suggesting that anisotropy near the inner core boundary does not include variations at hemispheric scale.

When $\mathrm{PKP}_{\mathrm{BC}}-\mathrm{PKP}_{\mathrm{DF}}$ data are divided into hemispheres and compared (Figures 4.10*c* and *d*), a smoother variation as a function of $\cos^2\xi$ is observed for the northern hemisphere than the western hemisphere. This is partly due to the separation of two anomalous clusters into different hemispheres, one associated with the south of Africa earthquake to California stations ($\cos^2\xi \sim 0.5$) and another with the South Sandwich Islands events recorded at Alaska ($\cos^2\xi \sim 0.8$). In contrast to $\mathrm{PKP}_{\mathrm{BC}}-\mathrm{PKP}_{\mathrm{DF}}$ data from the 150°–153° distance range, difference between hemispheres is not obvious for data between 145° and 150°. Division of data into northern and southern hemispheres seems to enhance hemispheric differences at this distance range, however, between 145° and 150°, there are only 9 measurements with $\cos^2\xi > 0.2$ for the southern hemisphere, so little significance can be attributed. In addition, there is no clear difference between eastern and western or northern and southern hemispheres for $\mathrm{PKP}_{\mathrm{AB}}-\mathrm{PKP}_{\mathrm{DF}}$ data in general (e.g., Figures 4.10*e* and *f*). The difference appears slightly more pronounced for the north-south division, however, it is difficult to compare the two subsets when the data are so sparse. It is, nonetheless, consistent with $\mathrm{PKP}_{\mathrm{DF}}$ or $\mathrm{PKP}_{\mathrm{BC}}-\mathrm{PKP}_{\mathrm{DF}}$ data in that the stronger anisotropy trend can be associated with the northern or western hemisphere.

In general, there is a good agreement between hemispheres when $\cos^2\xi < 0.7$ at all distance ranges. The travel times diverge rapidly, almost discontinuously, at around $\cos^2\xi = 0.7$, which is inconsistent with transversely isotropy where travel time depends smoothly on $\cos^2\xi$ (equation 2.19). Therefore, a difference in the strength of anisotropy is not sufficient to explain the observed change at high $\cos^2\xi$. The ambiguity of hemispherically dependent anisotropy is demonstrated further when

Figure 4.10: Hemispherical Subsets of Data

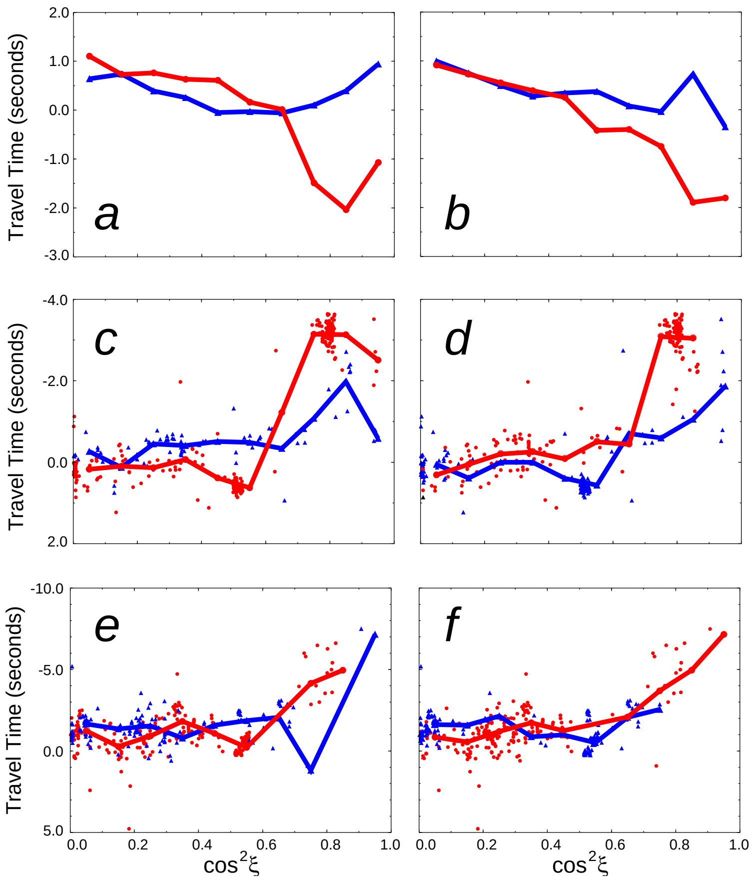

(a) and (b) Comparison of $\mathrm{PKP_{DF}}$ data in the distance range between 153° and 155°. The inner core is divided into eastern (blue triangles) and western (red circles) hemispheres in (a) while it is divided into northern (blue triangles) and southern (red circles) hemispheres in (b).
(c) and (d) Same as (a) and (b) except that $\mathrm{PKP_{BC}}-\mathrm{PKP_{DF}}$ data are compared at the distance range between 150° and 153°. The small triangles and circles are individual measurements. Note that there are no data between $\cos^2\xi$ of 0.2 and 0.4 for the southern hemisphere and between 0.9 and 1.0 for northern hemisphere.
(e) and (f) Same as (c) and (d) except that $\mathrm{PKP_{AB}}-\mathrm{PKP_{DF}}$ data are compared at the distance range of 153° and 160°. There are no data between $\cos^2\xi$ of 0.6 and 0.7, and 0.9 and 1.0 for the western hemisphere, between 0.8 and 0.9 for the eastern hemisphere, between 0.5 and 0.6 for the northern hemisphere, and between 0.8 and 1.0 for the southern hemisphere.

Figure 4.11: Geometry of $\mathrm{PKP_{DF}}$ and Bottoming Latitude

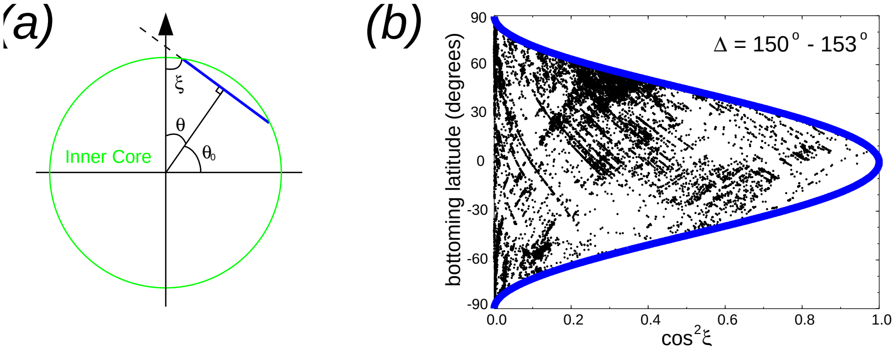

(a) The relationship between the bottoming latitude of the ray (θ_0) and the smallest value of the ray angle with respect to the rotation axis (ξ). The cross section through the inner core (green circle) is made in the north-south direction passing through the centre of the sphere. At the bottoming point, the ray (solid blue line) is perpendicular to the unit vector in radius. This implies that $\xi + \theta = 90°$, where θ is colatitude, and hence $\xi = \theta_0$.
(b) Plot of the ray's bottoming latitude (y-axis) against $\cos^2 \xi$. The blue curve shows the maximum $\cos^2 \xi$ as a function of latitude. The black dots show where individual $\mathrm{PKP_{DF}}$ datum between 150° and 153° distance range plots. Streaks of dots are the results of an earthquake observed at various stations and/or a station observing a suite of earthquakes.

data are binned to make summary rays depending upon the distance range, the ray angle ξ, and the bottoming point. One example from 153°–155°, which is the distance range where hemispheric difference is most prominent, is shown in Figure 4.13. Dependence on hemispheres is not an obvious feature except at high values of $\cos^2 \xi$. This approach also highlights the uneven distribution of data for all values of $\cos^2 \xi$, illustrating the difficulties of assessing lateral variations in anisotropy. Hemispheric dependence, be it east-west or north-south, can not be clearly identified with such sparse data set. Because large differences are observed only at large $\cos^2 \xi$, it is possible that the differences are due to poorer sampling and local structure. For example, biased sampling of an anomalous region of the inner core or mantle heterogeneity not included in the mantle correction can create apparent hemispheric differences. In the following section, the relationship between ray geometry and sampling location is investigated in an attempt to identify the source of hemispheric dichotomy for data with $\cos^2 \xi > 0.7$.

Ray Geometry: Bottoming Latitude and Ray Angle

The relationship between ray's bottoming latitude and angle from the rotation axis ξ can be obtained simply by noting that the smallest angle ξ (hence largest $\cos^2 \xi$) for a ray occurs when it is travelling in the north-south plane perpendicular to the equatorial plane. This implies that the smallest angle ξ is equal to the latitude of the bottoming point (Figure 4.11a). The relationship between the latitude of the bottoming point and the largest $\cos^2 \xi$ is plotted in Figure 4.11(b). Clearly, the data with high values of $\cos^2 \xi$ come only from rays bottoming near the equator while those with small $\cos^2 \xi$ values bottom at all latitudes. To compare anisotropy near the equator, which shows a puzzling discrepancy between hemispheres, with that near the poles, the $\mathrm{PKP_{DF}}$ data set is divided into four subsets: eastern polar, eastern equatorial, western polar and western equatorial regions. The latitudinal division is made so that data with absolute latitude less than 30° are put in equatorial groups and those greater than 30° are included in polar subsets. This analysis must rely upon the absolute travel times, since the number of differential travel time measurements in a given distance range is too scarce to permit a meaningful comparison of data behaviour between the four groups.

To ease comparison between the quadrants, only data between $\cos^2\xi$ of 0.0 and 0.7 are plotted, because values above 0.7 do not exist for polar subsets (Figure 4.12). Data from different quadrants generally agree in their trend (slope and curvature), with good agreement at distance ranges (150°–153°, 153°–155°, and 155°–160°) where a strong east-west hemispheric difference is observed. Moreover, the data trends agree surprisingly well with the prediction from the constant anisotropy model SPRI0. This suggests that a global anisotropy model can explain much of the data even if they are divided into hemispheres or quadrants, and apparent difference comes from a limited number of data. Data with $\cos^2\xi$ greater than 0.7 are inevitably less available than data with small $\cos^2\xi$, and the former data bottom in regions poorly covered by the latter data. This is particularly true for the western hemisphere where large travel time residuals are observed.

These results suggest that the hemispheric discrepancy is due to a smaller-scale phenomenon than hemispheric variations. The apparent hemispheric difference is explained easily if small structures are located in the inner core, however, because of the limited number of paths with $\cos^2\xi > 0.7$ and uneven coverage, the possibility of effects from the mantle cannot be dismissed.

4.5 Comparison of Absolute and Differential Travel Time Data

In this section, the discrepancy between absolute and differential travel time data is revisited. If the correction to absolute travel times and the assumption that the path similarity between the outer core bottoming phase ($\mathrm{PKP_{BC}}$ or $\mathrm{PKP_{AB}}$) and $\mathrm{PKP_{DF}}$ removes all non-inner core signal from differential travel times is valid, the absolute and differential data should agree well with one another. The difficulty in simultaneously fitting these two sets of data suggests that this is not the case.

$\mathrm{PKP_{BC}}-\mathrm{PKP_{DF}}$ data in the range from 150° to 153° are compared with $\mathrm{PKP_{DF}}$ from the same distance range in Figure 4.14(*a*). The two sets of averaged data agree well in general, except for 4 points at values of $\cos^2\xi$ of 0.45, 0.55, 0.75, and 0.85, where the averages of $\mathrm{PKP_{BC}}-\mathrm{PKP_{DF}}$ seem to be well constrained by clusters of measurements around $\cos^2\xi$ of 0.5 and 0.8. However, upon inspection of source-receiver pairs, the cluster about $\cos^2\xi = 0.8$ is found to be due to a path between South Sandwich Islands and Alaska. Data from this path are known to be anomalous (e.g., Su & Dziewoński, 1995; Dziewoński & Su, 1998), although the cause of the anomalies has not been convincingly identified. Many seismologists place the source of these anomalous measurements in the inner core (e.g., Creager, 1997; Dziewoński & Su, 1998), but there are arguments that they originate in the mantle (e.g., Helffrich & Sacks, 1994). When data from the path between South Sandwich Islands and Alaska is removed from the database, both $\mathrm{PKP_{BC}}-\mathrm{PKP_{DF}}$ and $\mathrm{PKP_{DF}}$ values are changed near $\cos^2\xi = 0.8$. The change in $\mathrm{PKP_{BC}}-\mathrm{PKP_{DF}}$ data is greater than in $\mathrm{PKP_{DF}}$, because the data from this path comprises a large part of the entire $\mathrm{PKP_{BC}}-\mathrm{PKP_{DF}}$ data set. The absolute and differential data sets agree now at $\cos^2\xi$ of 0.75 and 0.85 (Figure 4.14*b*).

The cluster at about $\cos^2\xi = 0.5$ is also from a single path, mainly due to a single earthquake south of Africa recorded at 71 stations in California. If this cluster (Figure 4.14*c*) is removed, the agreement between $\mathrm{PKP_{DF}}$ and $\mathrm{PKP_{BC}}-\mathrm{PKP_{DF}}$ data is remarkable, and the constant model of anisotropy SPRI0 fits both sets of body wave data. Inversions constrained only by, or relying heavily upon, the differential travel times are heavily biased by these anomalous data due to the abundance of measurements, and would produce models with strong anisotropy. For example, the model of Creager (1992) based upon differential travel times fits the anomalous data associated with the paths between South Sandwich Islands to Alaska at the expense of poorly fitting the data at higher values of $\cos^2\xi$ (Figure 4.3). Note that the cluster of measurements from the earthquake south of Africa were not included in that study, since the earthquake occurred on March 29, 1993.

One obvious question for the Africa to California measurements is whether the anomalously

Figure 4.12: Four Subsets of $\mathrm{PKP_{DF}}$ Data at Various Distances

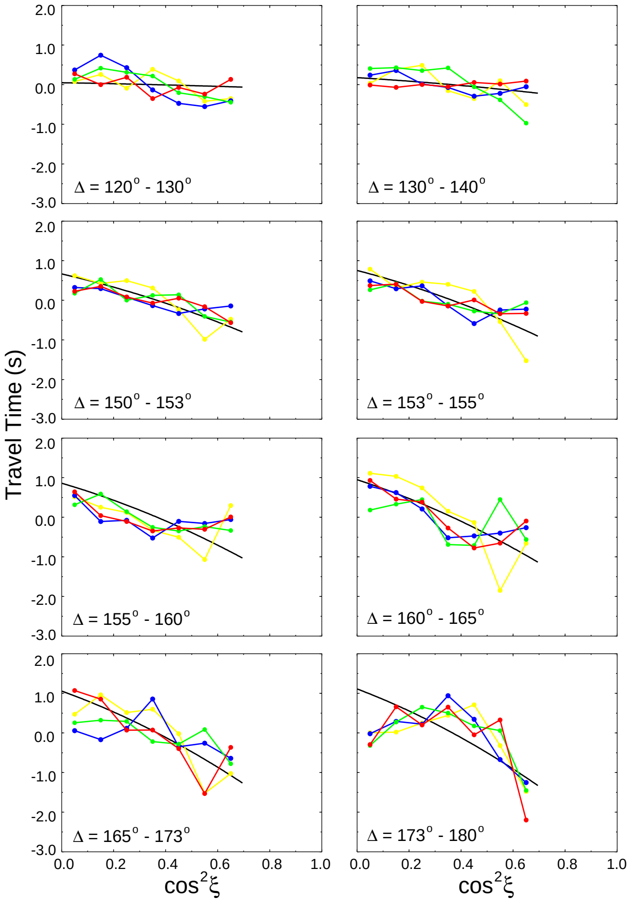

Data with different colors correspond to quadrants: eastern polar region (|latitude| > 30° with 0° ≤ longitude < 180°, green), eastern equatorial region (|latitude| ≤ 30° with 0° ≤ longitude < 180°, blue), western polar region (|latitude| > 30° with 180° ≤ longitude < 360°, yellow), and western equatorial region (|latitude| ≤ 30° with 180° ≤ longitude < 360°, red). Data with $\cos^2 \xi > 0.65$ are available for the two equatorial regions, however, the data are truncated at 0.65 to ease comparison between the four data sets. The black curve is the prediction based upon constant anisotropy model SPRI0.

Figure 4.13: PKP_{DF} Data from 153°–155° as a Function of Ray Angle and Bottoming Location

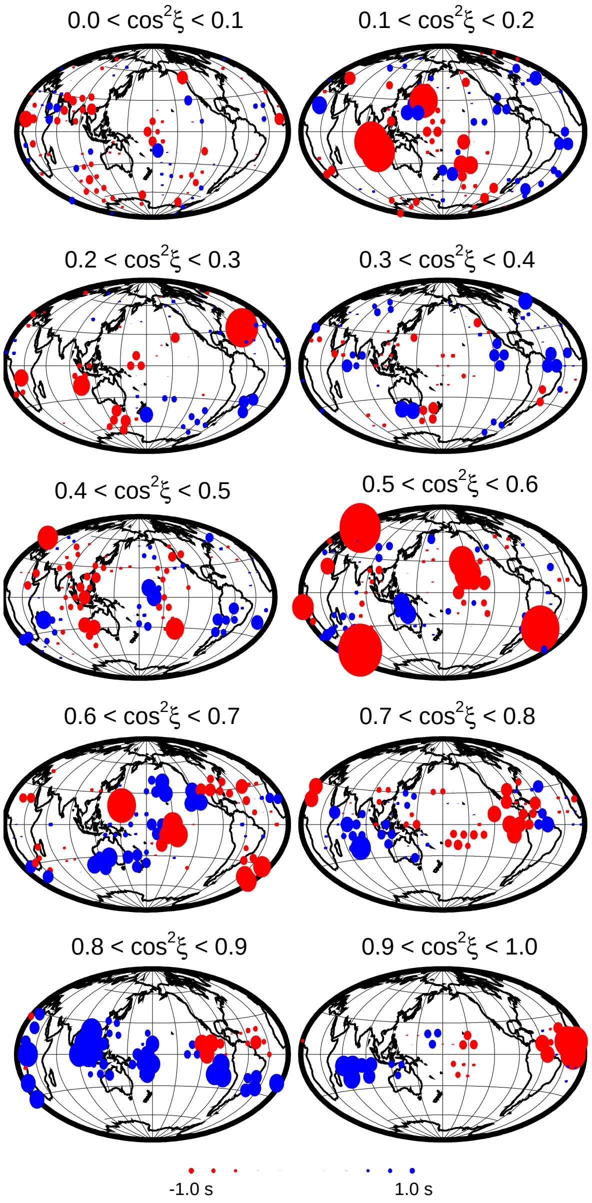
$0.0 < \cos^2\xi < 0.1$ $0.1 < \cos^2\xi < 0.2$

$0.2 < \cos^2\xi < 0.3$ $0.3 < \cos^2\xi < 0.4$

$0.4 < \cos^2\xi < 0.5$ $0.5 < \cos^2\xi < 0.6$

$0.6 < \cos^2\xi < 0.7$ $0.7 < \cos^2\xi < 0.8$

$0.8 < \cos^2\xi < 0.9$ $0.9 < \cos^2\xi < 1.0$

Size and colour of circles represent magnitude and sign of absolute travel time averages at the given ray angle range and bottoming location bin. For each plot, the average has been removed to enhance lateral variations. The center of each bin is obtained from dividing the Earth into 362 nearly equal area triangles using triangular tessellation (Figure 2.11). The radius of each bin is 10°. Unusually large values are due to bins with only one or two measurements.

Figure 4.14: Absolute and $\mathrm{PKP_{BC}}-\mathrm{PKP_{DF}}$ Travel Times

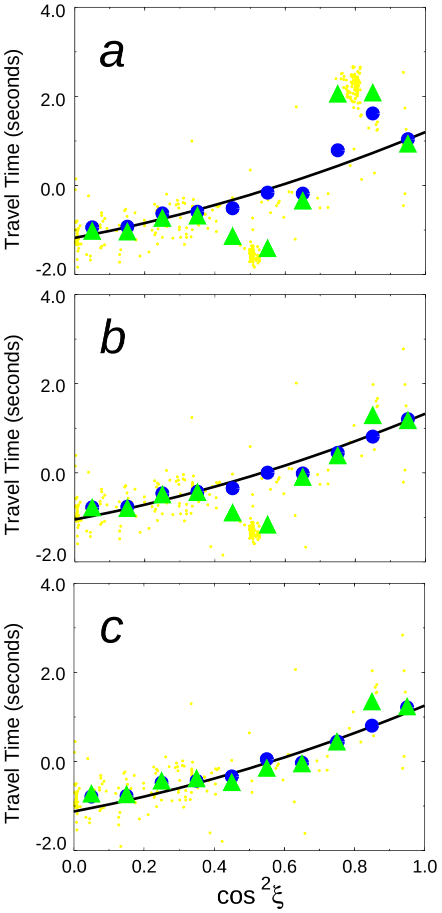

(a) Comparison of $\mathrm{PKP_{DF}}$ data (blue circles) and $\mathrm{PKP_{BC}}-\mathrm{PKP_{DF}}$ data (green triangles) in the distance range 150°–153°. To ease visual comparison, the sign of the $\mathrm{PKP_{DF}}$ data has been reversed, and a baseline shift has been applied. The background yellow dots are individual $\mathrm{PKP_{BC}}-\mathrm{PKP_{DF}}$ measurement, and the solid curve is the prediction based upon the constant anisotropy model SPRI0.
(b) Same as in (a), except that the data from the path between South Sandwich Islands and Alaska have been removed.
(c) Same as in (b), except that data from an earthquakes located south of Africa recorded at stations in California are removed.

Figure 4.15: Effect of Earthquake Mislocation on $\mathrm{PKP_{BC}}-\mathrm{PKP_{DF}}$ Travel Times

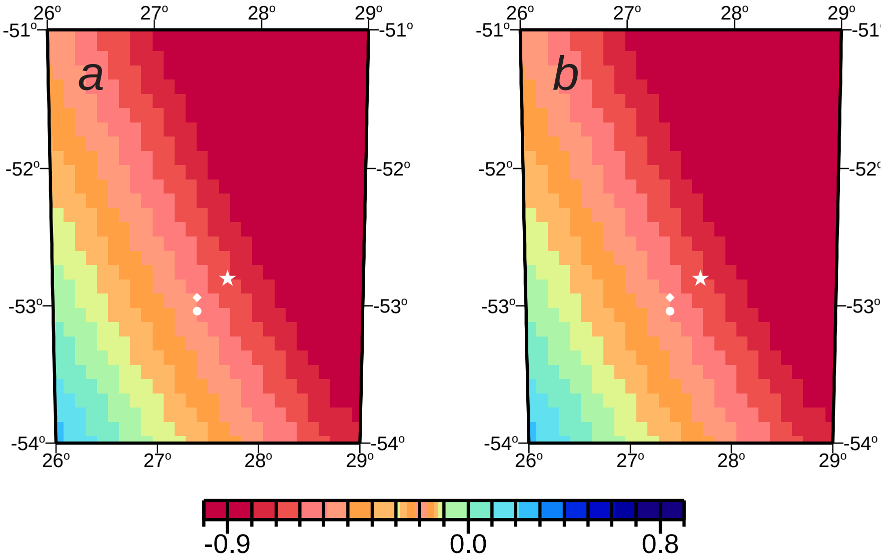

Perturbations to differential travel time as a function of different epicentral locations with respect to travel time calculated with Engdahl et al. (1998) hypocentre. Epicentres determined by three groups, NEIC (circle), Engdahl et al. (1998, diamond), and Harvard CMT catalogue (Dziewoński et al., 1994; star) are shown.
(*a*) Earthquake located at depth of 20 km. This is the depth of the earthquake given by Engdahl et al. (1998).
(*b*) Earthquake located at depth of 100 km.

negative values can be reconciled by earthquake mislocation. This is of particular concern because events in the southern hemisphere, due to poor station coverage, are more likely to be mislocated. Indeed, there are variations in the epicentral locations of this earthquake with Mw 5.7 (Harvard CMT catalogue, Dziewoński et al., 1994) determined by various institutions (Figure 4.15). To investigate if earthquake location can explain the observed data, average $\mathrm{PKP_{BC}}-\mathrm{PKP_{DF}}$ travel time due of the cluster is computed as a function of earthquake location (Figure 4.15). If earthquake mislocation is the source of anomalous data, then there should be a nearby location with travel time that is comparable to the prediction by SPRI0 ($\sim +0.5$ seconds). Comparison of Figure 4.15(*a*) and (*b*) show that the effect due to depth of the earthquake is insignificant, and is not detectable at the scale used in these figures. Varying the epicentral location gives larger changes in the travel times, but because this is differential, rather than absolute, travel time, the changes are small. In order to obtain a value of +0.5 seconds, the earthquake must be mislocated by about 150 km to the west. Mislocations of this magnitude, even in the southern hemisphere, is unlikely. So earthquake location does not appear to be the only source of anomalous $\mathrm{PKP_{BC}}-\mathrm{PKP_{DF}}$ measurements around $\cos^2\xi$ of 0.5.

Comparison of $\mathrm{PKP_{AB}}-\mathrm{PKP_{DF}}$ and $\mathrm{PKP_{DF}}$ in the range 160° to 165° is presented in Figure 4.16(*a*). In general, the two types of data agree well, which is surprising considering the likelihood of contamination from the mantle in $\mathrm{PKP_{AB}}-\mathrm{PKP_{DF}}$ data. The only exception is at $\cos^2\xi = 0.75$, where the $\mathrm{PKP_{AB}}-\mathrm{PKP_{DF}}$ average seems to be well constrained by numerous points between $\cos^2\xi$ values of 0.7 and 0.8. However, examination of these points reveals that they originate, with one exception, from a single earthquake near Bouvet Island recorded at 35 stations in Alaska. Removal of

Figure 4.16: Absolute and $\mathrm{PKP_{AB}}-\mathrm{PKP_{DF}}$ Travel Times

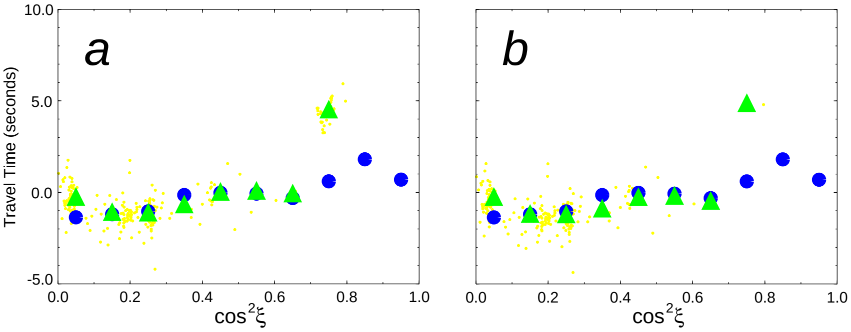

(a) Comparison of $\mathrm{PKP_{DF}}$ (blue circles) and $\mathrm{PKP_{AB}}-\mathrm{PKP_{DF}}$ (green triangles) in the distance range 160°–165°. There are no measurements of $\mathrm{PKP_{AB}}-\mathrm{PKP_{DF}}$ with $\cos^2\xi$ greater than 0.8 in this distance range. To ease visual comparison the sign of $\mathrm{PKP_{DF}}$ has been reversed, and a baseline shift has been applied. The background yellow dots are individual differential $\mathrm{PKP_{AB}}-\mathrm{PKP_{DF}}$ measurement.
(b) Same as in (a), except that the data from an earthquake near Bouvet Island recorded at stations in Alaska are removed.

Figure 4.17: Bottoming Point Coverage of the Inner Core

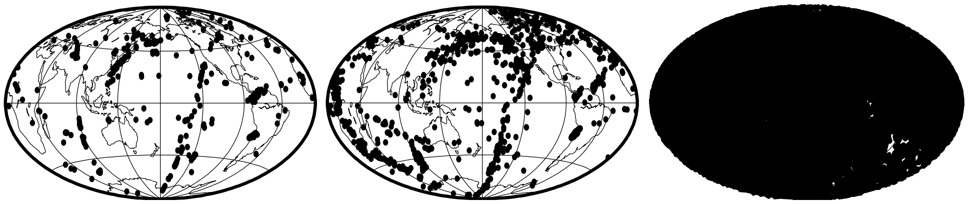

Plot of all bottoming points for $\mathrm{PKP_{BC}}-\mathrm{PKP_{DF}}$ (left), $\mathrm{PKP_{AB}}-\mathrm{PKP_{DF}}$ (centre) and $\mathrm{PKP_{DF}}$ (right) data. This plot is made using all data from all distances and ray angles.

this earthquake (Figure 4.16b) does not improve the compatibility of $\mathrm{PKP_{AB}}-\mathrm{PKP_{DF}}$ and $\mathrm{PKP_{DF}}$, but since the average at $\cos^2\xi = 0.75$ is determined by a single datum, it is possible that this discrepancy reflects either another anomalous path or substantial mantle heterogeneity or source mislocation.

These comparisons demonstrate the sampling bias in the differential travel time data set. Figure 4.17 shows the coverage of the inner core with the entire set of $\mathrm{PKP_{BC}}-\mathrm{PKP_{DF}}$, $\mathrm{PKP_{AB}}-\mathrm{PKP_{DF}}$ and $\mathrm{PKP_{DF}}$ data in terms of bottoming point. This is not a fair comparison in the sense that the epicentral distance covered by the three types of data differ considerably. However, if inner core anisotropy is constant as in SPRI0, all distances are considered equally and thus comparison becomes valid. Most of the inner core is not sampled by the differential travel time measurements, but it is well sampled by $\mathrm{PKP_{DF}}$ data except for some spots in the south Atlantic. This explains why $\mathrm{PKP_{DF}}$ data are highly compatible with normal modes. Additional problem with poor coverage is that it cannot assure the cancellation of effects due to variations within the mantle. These are likely to be the reason why differential data are poorly fit by a simple model of the inner core. The deviation of differential travel times from the constant model is investigated in the next section.

4.6 Residual Data

The model SPRI0 does not achieve a perfect fit to data used in the inversion. This section focuses on the signal that is not explained by SPRI0 to understand why the misfit occurred and if this signal contains useful information for deep Earth structure not considered in the modelling.

4.6.1 Residual Splitting Function Coefficients

In Figure 4.18(*a*), three splitting functions for the inner core sensitive mode ${}_8S_1$ determined by different groups are shown. Before mantle and inner core corrections are applied, the three measurements agree very well with one another, both in terms of amplitude and pattern. After corrections, all residual splitting functions exhibit an almost pure degree 2 order 1 pattern. However, the relative importance of the real and imaginary parts (or sine and cosine parts) of this spherical harmonic component are different, resulting in rotated residual patterns with respect to one another. Perhaps this signal is related to differential rotation of the inner core, since the observed splitting functions are derived from earthquake records spanning different times. He & Tromp (1996) use records from the Bolivia and Kuril events in 1994, Resovsky & Ritzwoller (1998) use records from 33 earthquakes between 1977 and 1995, and Durek & Romanowicz (1999) use records from 8 earthquakes between 1994 and 1996. The rotation rate obtained by comparison of the He & Tromp (1996) and Durek & Romanowicz (1999) residuals would give a large rotation rate, incompatible even with body wave estimates (e.g., Song & Richards, 1996; Su et al., 1996; Creager, 1997). Rather, the differences are within the uncertainties of splitting function measurements. This is more apparent when observations for less well-determined modes are compared (Figure 4.18*b*). The two measurements of the splitting function for mode ${}_{13}S_2$ are similar in their banded signal, but their non-zonal parts are strongly anti-correlated.

To investigate the general pattern of the splitting signal that has not yet been modelled, splitting function residuals are stacked after the removal of mantle and inner core effects (Figure 4.19). Each residual splitting function is normalised, summed, and divided by the number of data available. If individual residuals are random noise, then this averaging process should give a stacked residual that is close to zero. The amplitude of stacked residuals for both mantle and inner core modes are much less than one (Figure 4.18), but the amplitude for mantle modes is lower than for inner core sensitive modes. The residual map of inner core modes has a strong spherical harmonic degree 2 order 2 pattern, but that of mantle modes are dominated by structure at higher degrees. If the residual pattern of inner core modes is coming from inner core properties, then it may require another type of anisotropy or more than one symmetry axis. However, it is also possible that this signal originates in the deep mantle, since many mantle modes (e.g., numerous surface wave equivalent modes) are not strongly sensitive to the lower-most mantle.

4.6.2 Residual Differential Travel Times

The issue of a possible mantle signal in differential travel times is addressed by plotting the individual differential travel time residual (observed travel time minus travel time due to inner core anisotropy) against predicted differential travel time arising from a compressional wave model of the mantle (Antolik et al., 2003). The results for $\mathrm{PKP_{BC}}-\mathrm{PKP_{DF}}$ and $\mathrm{PKP_{AB}}-\mathrm{PKP_{DF}}$ are shown in Figure 4.20. In general, the predicted residuals due to mantle structure is much smaller than the observed residuals, consistent with the results of Bréger et al. (1999, 2000). For $\mathrm{PKP_{BC}}-\mathrm{PKP_{DF}}$, there is no correlation between observed and predicted residuals if the entire data set is considered, but if measurements from the two anomalous paths, from South Sandwich Island to Alaska and from south of Africa to California, are removed, the data are slightly correlated. The large residuals from the two anomalous paths deviate far from the main cluster and clearly stand out in this plot. Although part of this deviation could be due to structure near the core-mantle boundary that is not

Figure 4.18: Residual Splitting Function Coefficients

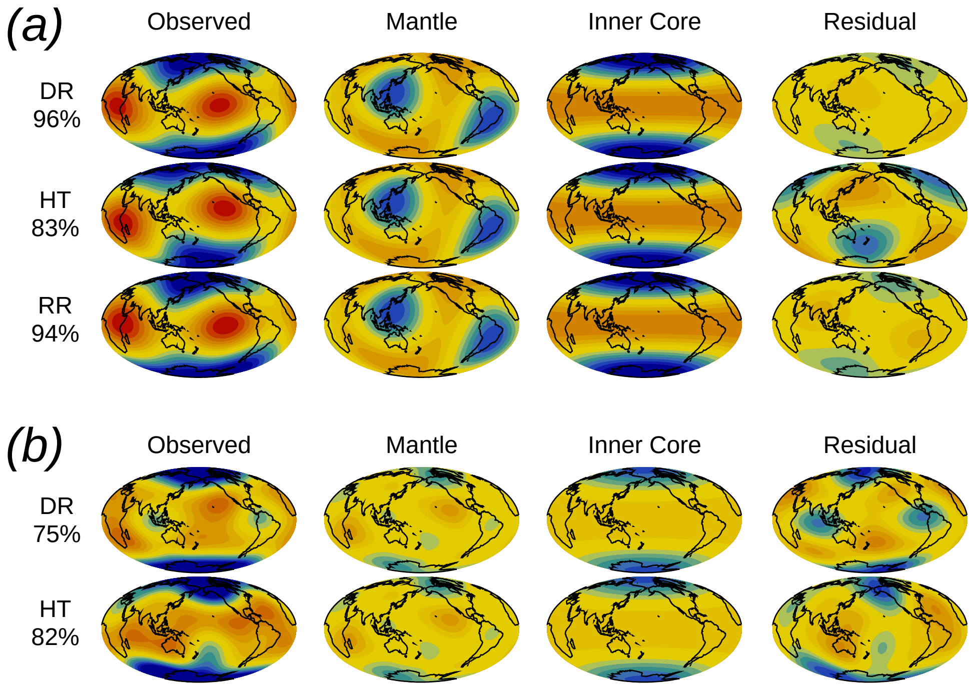

Splitting functions given by Durek & Romanowicz (1999) denoted “DR”, He & Tromp (1996) denoted “HT”, and Resovsky & Ritzwoller (1998) denoted “RR”. Observed splitting functions are plotted in the first column, the second and third columns show predictions based upon the mantle and inner core parts of SPRI0, and the final column is the residual splitting function. The variance reduction for each measurement using SPRI0 are indicated beneath the mode name. The colour scale is fixed for each mode.

(a) Comparison of mode ${}_8S_1$.

(b) Comparison of mode ${}_{13}S_2$.

Figure 4.19: Stacked Residual Splitting Functions

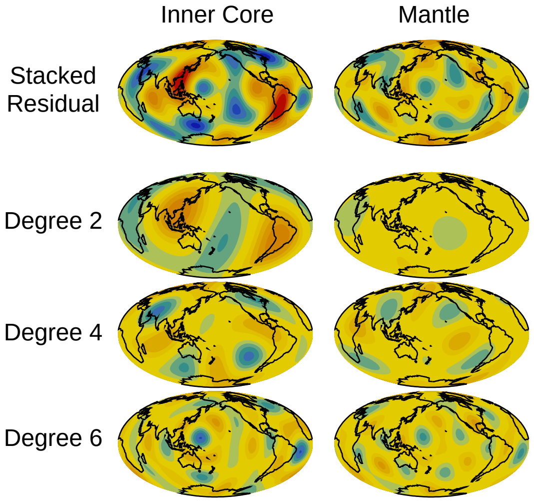

Stacked residuals for inner core sensitive modes (left) and for mantle sensitive modes (right). The top row is the residual pattern using degrees 2, 4, and 6, and the three rows below show residual pattern at individual degrees. The scale is fixed for all plots and is chosen to slightly over-saturate the amplitude of stacked inner core modes with all degrees (±0.2).

in the mantle model, the residuals are too large to be explained completely by mantle heterogeneity, demanding a further analysis in the future.

A similar comparison for $\mathrm{PKP_{AB}}-\mathrm{PKP_{DF}}$ data exhibits a stronger correlation between predictions and observations, indicating that mantle structure is important for this data set. There is high correlation with a correlation coefficient of 0.7, but the range of amplitudes for predictions are much smaller than those of the residuals. It suggests that the compressional wave model in the lower-most mantle is under-estimated as has been documented for shear wave speed models (e.g., Ritsema et al., 1998; Bréger & Romanowicz, 1998). Creager (1999) performed a similar experiment using a mantle model by Kárason & van der Hilst (2001), comparing mantle predictions with $\mathrm{PKP_{BC}}-\mathrm{PKP_{DF}}$ and $\mathrm{PKP_{AB}}-\mathrm{PKP_{DF}}$. He found no significant correlation between data and prediction from the mantle model. This may be due to inner core anisotropy signal obscuring correlation and under-estimation of mantle structure near the core-mantle boundary.

Previous studies have suggested that most of differential travel time signals may be associated with heterogeneity in the lower-most mantle, where the ray paths differ considerably (Song & Helmberger, 1997; Bréger et al., 1999, 2000; Tkalčić et al., 2002). Instead of modelling the mantle with raw differential data, residuals after inner core corrections are considered. These residuals are placed at the outer core entry and exit points of the $\mathrm{PKP_{BC}}$ or $\mathrm{PKP_{AB}}$ ray and the average for each 10° by 10° block is calculated. The inherent assumption in this exercise is that the residuals originate from $\mathrm{PKP_{BC}}$ or $\mathrm{PKP_{AB}}$ sampling the lower-most mantle rather than $\mathrm{PKP_{DF}}$. With this assumption, positive and negative residuals are associated with slower and faster wave speeds, respectively. Note that positive anomalies, if ascribed to the $\mathrm{PKP_{DF}}$ part of the differential data, imply faster than average wave speed and vice versa. This procedure does not spread residuals along the ray path of $\mathrm{PKP_{BC}}$ or $\mathrm{PKP_{AB}}$, nevertheless, the resulting maps give an indication of the importance of mantle structure near the core-mantle boundary.

Figure 4.21(*a*) shows the hitcount and residual map of $\mathrm{PKP_{BC}}-\mathrm{PKP_{DF}}$. The hitcount map shows a very biased distribution, with most of the core-mantle boundary poorly sampled (regions in

Figure 4.20: Residual and Predicted Differential Travel Times due to Mantle Structure

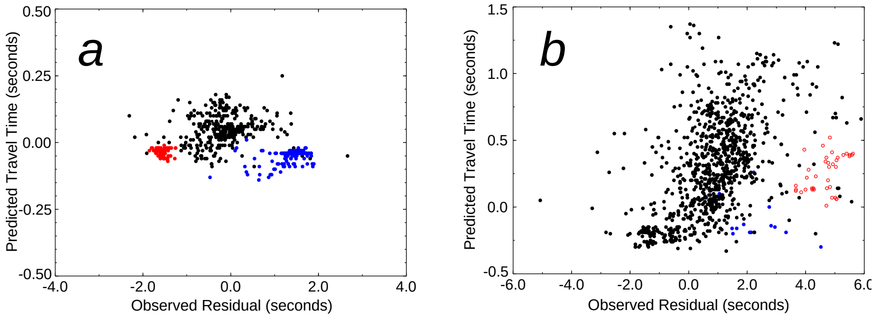

(*a*) Plot of $\mathrm{PKP_{BC}}-\mathrm{PKP_{DF}}$ residuals after correcting for constant anisotropy in the inner core (x-axis) and travel time anomalies predicted by mantle heterogeneity based upon the compressional wave speed model of Antolik et al. (2003) (y-axis). The blue dots are for a path between the South Sandwich Islands and Alaska, red dots are for a path between south of Africa and California and black dots are for other paths.
(*b*) Same as in (*a*) except for the $\mathrm{PKP_{AB}}-\mathrm{PKP_{DF}}$ data. The blue dots are for a path between the South Sandwich Islands and Alaska, and red dots are for a path between Bouvet Island and California.

black) as expected. There are exceptions, for example, the areas under north-western Canada and the southern Atlantic are well sampled by measurements from the South Sandwich Islands events recorded at stations in Alaska. Similarly, the paths from south of Africa to numerous stations in California appear as high counts near Antarctica and the south-western United States. The strongest features in the map of $\mathrm{PKP_{BC}}-\mathrm{PKP_{DF}}$ travel times before inner core corrections is a zonal pattern, i.e., positive anomalies (red to yellow) at high latitudes and negative (blue to green) anomalies near the equator. The map view of $\mathrm{PKP_{BC}}-\mathrm{PKP_{DF}}$ after inner core corrections, in contrast, is highly non-zonal. There are still some strong features, such as a positive (slow if due to $\mathrm{PKP_{BC}}$) anomaly in the south Pacific and a negative (fast) anomaly between South America and Antarctica. However, the amplitude of these anomalies is much lower compared to a map without inner core corrections.

Although there are more $\mathrm{PKP_{AB}}-\mathrm{PKP_{DF}}$ data, Figure 4.21(*b*) shows that they still come from limited source-receiver pairs; the data cover the globe unevenly, with a bias towards the western hemisphere. Therefore, the averaging procedure is insufficient to cancel out the mantle contribution. The zonal pattern observed in the uncorrected map of $\mathrm{PKP_{BC}}-\mathrm{PKP_{DF}}$ is not present for raw $\mathrm{PKP_{AB}}-\mathrm{PKP_{DF}}$ map, and the pattern from raw data looks similar to the corrected $\mathrm{PKP_{BC}}-\mathrm{PKP_{DF}}$ map. The map of $\mathrm{PKP_{AB}}-\mathrm{PKP_{DF}}$ after inner core corrections appears virtually identical to the uncorrected map, although inner core corrections reduce the amplitude of the residuals. $\mathrm{PKP_{AB}}$ is a ray that grazes the core-mantle boundary where strong heterogeneities have been observed (e.g., Garnero et al., 1998). Hence it is not surprising if $\mathrm{PKP_{AB}}-\mathrm{PKP_{DF}}$ contain strong signals from mantle heterogeneity.

The residual patterns for $\mathrm{PKP_{BC}}-\mathrm{PKP_{DF}}$ and $\mathrm{PKP_{AB}}-\mathrm{PKP_{DF}}$ are very similar in regions that are well sampled, suggesting that these signals originate in the lower-most mantle. The difference in amplitude between the two maps arises, because $\mathrm{PKP_{AB}}$ is nearly horizontal in the lower-most mantle, and is affected more strongly by structure near the core-mantle boundary. Some of the features observed in the residual maps agree with compressional wave speed models near the core-mantle boundary, such as the fast anomaly under India and eastern Asia, and the slow anomaly in the southern Pacific ocean. In addition, the fast, linear anomaly in the northern Pacific is also consistent with some models (e.g., Vasco & Johnson, 1998; van der Hilst et al., 1998; Boschi &

Figure 4.21: Residual Differential Travel Times

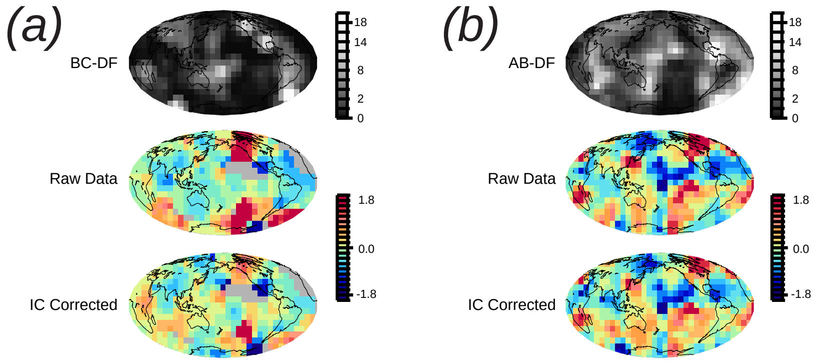

(*a*) Hitcount map for $\mathrm{PKP_{BC}}-\mathrm{PKP_{DF}}$ measurements (top). Black regions indicate poor sampling and white indicate well-sampled regions. Note that the number of data is much smaller compared to conventional seismic tomography of the mantle or $\mathrm{PKP_{DF}}$ measurements from ISC. Accordingly, the scale is the number of rays rather than its logarithm.
Map view of raw (middle) and residual (bottom) $\mathrm{PKP_{BC}}-\mathrm{PKP_{DF}}$ plotted at the entry and exit points of $\mathrm{PKP_{BC}}$. Red regions indicate places with positive travel time anomalies and blue regions indicate negative anomalies.
(*b*) Same as in (*a*) except for $\mathrm{PKP_{AB}}-\mathrm{PKP_{DF}}$ measurements.

Dziewoński, 1999; Kárason & van der Hilst, 2001) and this feature is also observed in some shear wave models (e.g., Gu et al., 2001). Furthermore, the locations of slow anomalies in the residual maps (Figures 4.21) correspond well with observations of ultra low velocity zones, for example, underneath southern Pacific and Africa (e.g., Mori & Helmberger, 1995; Garnero & Helmberger, 1996; Vidale & Hedlin, 1998; Garnero et al., 1998). However, there are structures in the residual maps, such as a slow anomaly under Canada and Alaska, that do not exist in whole mantle models. Most tomographic models are fast in this region, with some exceptions, such as the shear wave model of Su & Dziewoński (1997), which has close to zero value, and the compressional wave model of van der Hilst et al. (1998) with a negative anomaly underneath Alaska. The D" model of Tkalčić et al. (2002), based upon PcP−P and differential data, also shows a negative velocity anomaly under Canada. This anomaly contributes to the large positive $\mathrm{PKP_{BC}}-\mathrm{PKP_{DF}}$ measurements for the path between South Sandwich Islands to Alaska (Figure 4.14).

The residual patterns, especially that of $\mathrm{PKP_{AB}}-\mathrm{PKP_{DF}}$, agree well with the D" model of Tkalčić et al. (2002). The main difference between the maps shown in Figures 4.21 and the structure obtained by Tkalčić et al. (2002) is the strength of the anomalies. The residual maps of $\mathrm{PKP_{BC}}-\mathrm{PKP_{DF}}$ and $\mathrm{PKP_{AB}}-\mathrm{PKP_{DF}}$ generally have an amplitude of ±1.5 seconds, and if the signal is assumed to come from a sampling length of 300 km, then a simple conversion gives approximately ±7% variations. These calculations do not consider the geometry and length of the $\mathrm{PKP_{BC}}$ or $\mathrm{PKP_{AB}}$ ray path, so this is likely to be an over-estimate. Most compressional wave models (e.g., Bolton, 1996; Boschi & Dziewoński, 1999) have amplitudes of ±1% near the core-mantle boundary and so does much of the D" model of Tkalčić et al. (2002), although the latter includes anomalies in excess of ±2.5%. Nonetheless, amplitudes as large as ±7% have been observed in the bottom-most mantle using diffracted P waves (Sylvander et al., 1997).

These observations indicate that most of the differential anomaly that is not explained by the constant inner core anisotropy model can be attributed to heterogeneity deep within the mantle. The strong anisotropy in inner core models derived from differential travel time data is due to local anomalies or structure near D". In particular, the deepest inner core model obtained from differential

Figure 4.22: Set Up for Mantle Convection Simulation

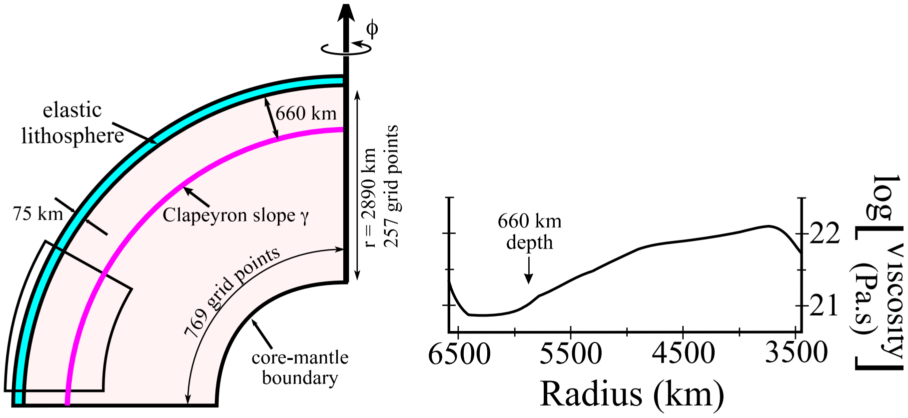

Summary of grid points, and physical parameters used in mantle convection simulation. Figure courtesy of R. Pysklywec.

travel times is constrained only by a heavily contaminated $\mathrm{PKP_{AB}}-\mathrm{PKP_{DF}}$ data, making inferred increase in anisotropy questionable. Inverting for inner core structure using normal mode, absolute, and differential travel time data allows for separation of mantle and inner core effects.

4.7 Small-Scale Mantle Heterogeneity and Differential Travel Times

In order to assess the effects of mantle structure on differential travel times, especially the small-scale features on $\mathrm{PKP_{BC}}-\mathrm{PKP_{DF}}$ data, rays are shot through models of the mantle obtained from mantle convection simulations. The purpose of this study is to see if anomalously large travel times can be generated by mantle heterogeneity, and if so, what kind of structure is responsible for the extreme values. In addition, it will be important to investigate the distribution of travel time values. Multiple measurements or averaging scheme used to reduce the mantle effect is only valid if data follow a Gaussian distribution.

Because of the paths geometry, differential travel time data are thought to be only sensitive to the mantle structure near the core-mantle boundary (e.g., Bréger & Romanowicz, 1998). For much of the mantle, the difference between ray paths is considered too small in comparison to the wavelength of heterogeneities, except in the lower-most mantle. Correspondingly, large values of mantle induced $\mathrm{PKP_{AB}}-\mathrm{PKP_{DF}}$ are expected to occur as the epicentral distance is increased, since the separation of the rays increases with epicentral distance. There is no agreement upon the strength of the mantle contribution to $\mathrm{PKP_{AB}}-\mathrm{PKP_{DF}}$, and the amount of $\mathrm{PKP_{AB}}-\mathrm{PKP_{DF}}$ attributed to mantle heterogeneities ranges from zero (inner core studies) to more than 4 seconds (D" studies). For $\mathrm{PKP_{BC}}-\mathrm{PKP_{DF}}$, the ray paths of $\mathrm{PKP_{BC}}$ and $\mathrm{PKP_{DF}}$ move away from one another as the epicentral distance is decreased, because $\mathrm{PKP_{BC}}$ is a retrograde phase. Nonetheless, the two paths are close at all epicentral distances, and $\mathrm{PKP_{BC}}-\mathrm{PKP_{DF}}$ data are thought to be insensitive to the mantle structure.

Models from Convection Simulations

The convection simulation is performed using an axisymmetric formulation and the finite difference technique (Pysklywec & Mitrovica, 2000). This simulation includes phase transition at the 660-km discontinuity with density jump at the boundary (Figure 4.22), but detailed description can be found in Pysklywec & Mitrovica (2000). The mantle model obtained from the simulation consists of values of absolute density at each grid point, and perturbations in density are derived by removing the average at each depth. To convert density variations to compressional wave speed variations, the depth dependent linear relationship given by Karato (1993a) is used. This conversion factor is defined for most part of the mantle, but values near the Moho and the core-mantle boundary are not available. Therefore, Karato's profile is supplemented with a value of 0.36 which is the depth independent value used in the previous Chapter.

A pair of rays, $\mathrm{PKP_{DF}}$ and outer core bottoming phase, are shot through the mantle model, and the starting point of the rays is moved systematically to sample the model completely. The differential travel times are plotted as a function of the starting point in order to identify mantle structure responsible for the variations. Note that differential travel time is calculated for rays sampling the mantle once, either going down to the core-mantle boundary or coming up to the surface, rather than the full path where rays go down to the core-mantle boundary, travel through the core, and then return to the surface.

Figure 4.23 illustrates the variations of $\mathrm{PKP_{AB}}-\mathrm{PKP_{DF}}$ obtained from one of the simulation models. Although the mantle heterogeneity is relatively smooth, $\mathrm{PKP_{AB}}-\mathrm{PKP_{DF}}$ changes rapidly, often producing cusps and discontinuities which are well correlated with small structures in the upper mantle. The figure also shows that the greatest negative anomaly has larger amplitude than the maximum positive anomaly. This is seen more clearly when the differential travel times are plotted in histograms. The distributions are all skewed with a longer tail in negative travel times. Most Gaussian-like behaviour, with clustering near zero, is observed at the shortest distance, where the ray paths are most similar. At larger distances, the main peak occurs around 1 second, and often, there are multiple peaks. Furthermore, the range of travel times expands as the distance increases.

As expected, the effect of mantle structure on $\mathrm{PKP_{BC}}-\mathrm{PKP_{DF}}$ is much weaker than on $\mathrm{PKP_{AB}}$ $-\mathrm{PKP_{DF}}$ (Figure 4.24). The variations in differential travel times with different starting locations are similar to those of $\mathrm{PKP_{AB}}-\mathrm{PKP_{DF}}$ with fluctuations which are well correlated with upper mantle features, especially the fast anomalies. These fluctuations are quite large at 145°, but it is barely visible at 152°. Although the distributions of $\mathrm{PKP_{BC}}-\mathrm{PKP_{DF}}$ residuals are more Gaussian-like than for $\mathrm{PKP_{AB}}-\mathrm{PKP_{DF}}$ with a peak near zero, there are extreme values even for closely spaced rays of $\mathrm{PKP_{BC}}-\mathrm{PKP_{DF}}$ (Figure 4.24).

Test Models

If mantle anomalies are distributed randomly within the mantle, travel times should form a Gaussian distribution. However, in reality, the mantle has well-defined linear subductions and upwellings that are not randomly oriented. To investigate the effect of coherent structures in the mantle, results using test models are analysed. The first test model contains a vertical low density anomaly and a subduction whose orientation is assigned by the $\mathrm{PKP_{AB}}$ path calculated at the epicentral distance of 160°. The maximum density perturbation at every depth is set to $\pm 1.5\%$ and the width of the anomalies is kept constant. Results are shown in Figures 4.25 and 4.26. Because there are only two anomalies, the rays mainly travel through homogeneous mantle, so travel times are mostly zero. However, when the anomalies are sampled, extreme travel times are observed. In addition, the fast structure recreates the skewness in the distribution of $\mathrm{PKP_{AB}}-\mathrm{PKP_{DF}}$ with long tail in the negative values (Figure 4.25). The multiple peaks are not reproduced, but comparison of results from different simulation models suggests that they are related to multiple occurrences of slow and fast wave speed anomalies with different orientations. In contrast, the distribution of $\mathrm{PKP_{BC}}-\mathrm{PKP_{DF}}$ have a longer tail in the positive values which is not observed in results from convection simulation

Figure 4.23: PKP$_{\mathrm{AB}}$−PKP$_{\mathrm{DF}}$ from Simulated Mantle Heterogeneity

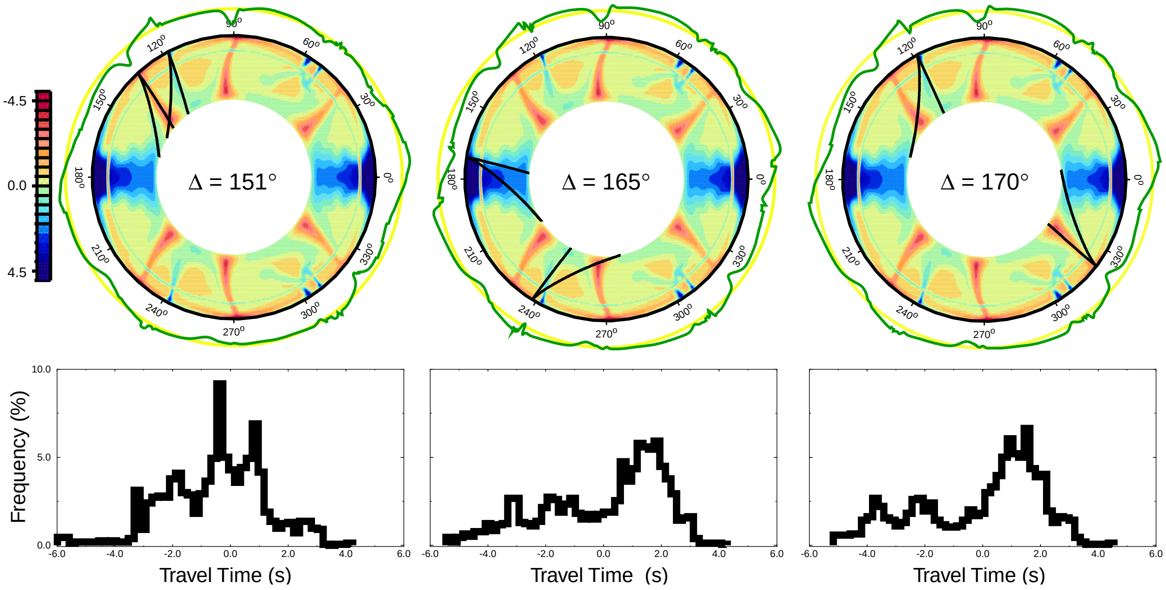

(*top*) Compressional wave speed and travel time variations at three different epicentral distances, 151° (left), 165° (centre), and 170° (right). The colour scale is given in percent compressional wave speed variations. The green curve around the yellow circle represents variations in the differential travel times due to the mantle structure with the yellow circle as the zero reference. PKP$_{\mathrm{AB}}$−PKP$_{\mathrm{DF}}$ residual is positive when the green curve is plotted outside this circle, and negative when it is inside. The perturbation in differential travel time is plotted at the angle at which the two rays originate. The black curves overlaying the mantle are the ray paths at positions where maximum and minimum travel times are obtained. More vertical of the two rays is the PKP$_{\mathrm{DF}}$ path in the mantle and the other is the PKP$_{\mathrm{AB}}$ path.
(*bottom*) Histogram of differential travel times obtained for the three epicentral distances. The number of measurements within each travel time range is given in percentage of the entire measurements.

Figure 4.24: PKP$_{\mathrm{BC}}$−PKP$_{\mathrm{DF}}$ from Simulated Mantle Heterogeneity

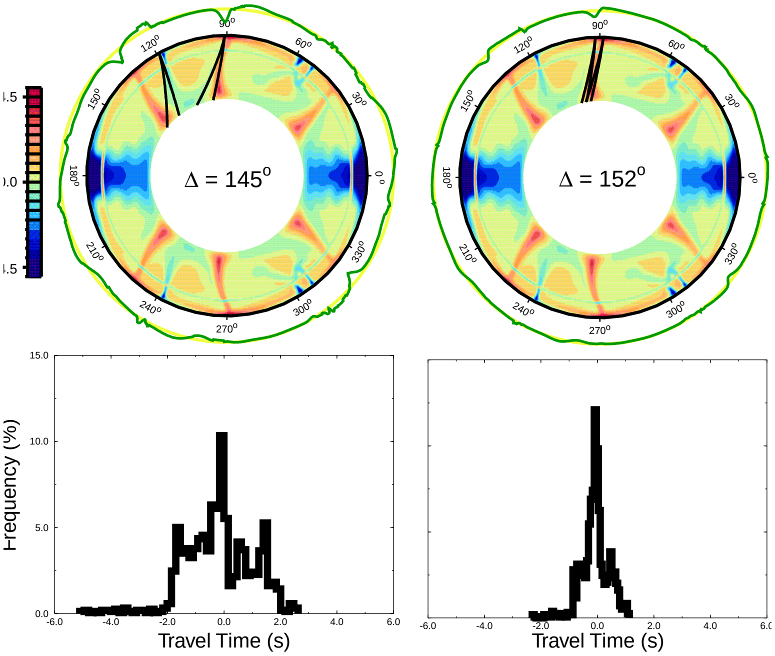

Same as in Figure 4.23 except that PKP$_{\mathrm{BC}}$−PKP$_{\mathrm{DF}}$ travel times are considered at 145° (left) and 152° (right) distances.

Figure 4.25: PKP$_{\mathrm{AB}}-$PKP$_{\mathrm{DF}}$ from the Test Mantle Model

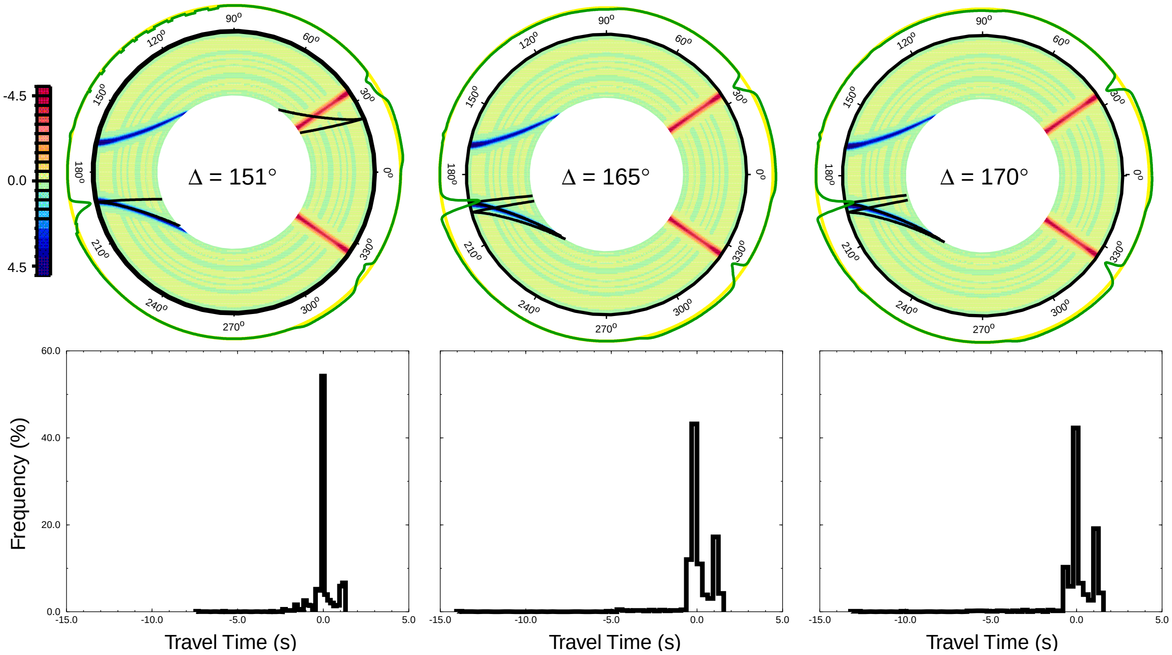

Same as in Figure 4.23 except that the heterogeneities are calculated from the test model with vertical low density anomaly and high density anomaly that follows the path of PKP$_{\mathrm{AB}}$. Note that there is a long tail in negative travel times (i.e., zero travel time is not at the centre of the histograms).

models (Figure 4.26). This is due to the particular choice of structures, and there are orientations of slow and fast anomalies which produce distributions of PKP$_{\mathrm{AB}}-$PKP$_{\mathrm{DF}}$ and PKP$_{\mathrm{BC}}-$PKP$_{\mathrm{DF}}$ with larger negative values.

The second test model addresses the question regarding the source of extreme differential travel times. Contrary to expectation, large values of PKP$_{\mathrm{AB}}-$PKP$_{\mathrm{DF}}$ and PKP$_{\mathrm{BC}}-$PKP$_{\mathrm{DF}}$ are observed near strong upper mantle heterogeneity. Consequently, the second test model is constructed using the first model but without anomalies in the lower mantle. The travel times are generally smaller than obtained using simulation models, but they are not trivial when the upper mantle anomalies are sampled (Figures 4.27 and 4.28). The resulting distributions of travel times appear as δ-functions for both PKP$_{\mathrm{AB}}-$PKP$_{\mathrm{DF}}$ and PKP$_{\mathrm{BC}}-$PKP$_{\mathrm{DF}}$, but there is a relatively wide range of values which may have significant consequences.

Summary

Shooting rays through mantle models showed some unexpected results. Observations of large travel times are strongly correlated with near surface features, and extreme differential travel times can be produced by upper mantle structure even for PKP$_{\mathrm{BC}}-$PKP$_{\mathrm{DF}}$.. Furthermore, the distributions of travel times are not Gaussian, and the most frequently observed values are often non-zero. The skewness of the distributions can be explained by the angle of linear structures within the mantle, and the multiple peaks in distribution can be associated with the number of anomalies with varying orientations. These observations suggest that the effects due to the mantle can be much stronger for

Figure 4.26: $\mathrm{PKP_{BC}}-\mathrm{PKP_{DF}}$ from the Test Model

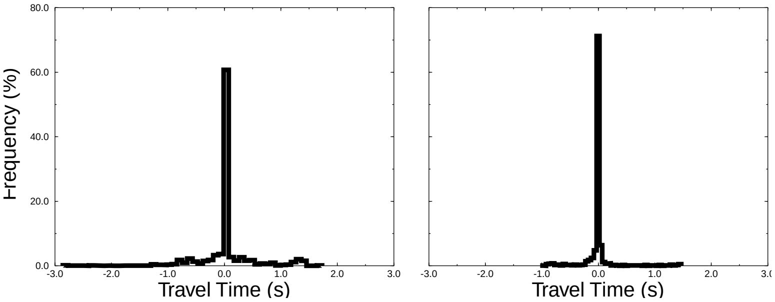

Histogram of differential travel times obtained at 145° (left) and 152° (right) epicentral distances.

Figure 4.27: $\mathrm{PKP_{AB}}-\mathrm{PKP_{DF}}$ from Upper Mantle Heterogeneity

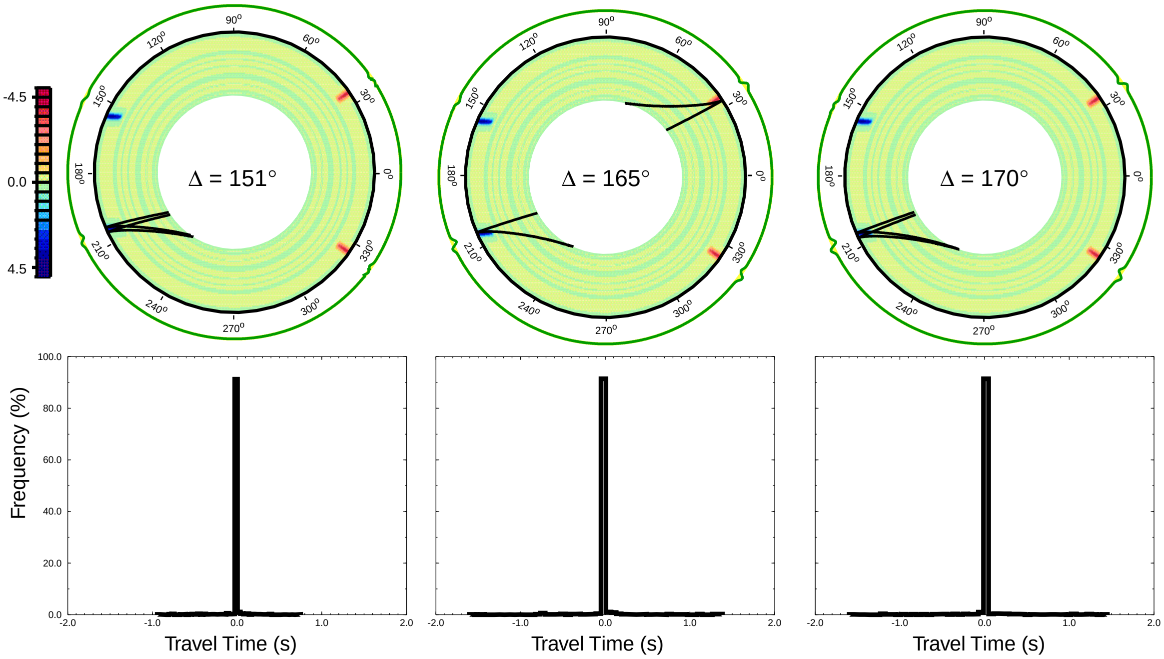

Same as in Figure 4.23 except that the mantle model is the test model with only structure in the upper mantle.

Figure 4.28: $\mathrm{PKP_{BC}}-\mathrm{PKP_{DF}}$ from Upper Mantle Heterogeneity

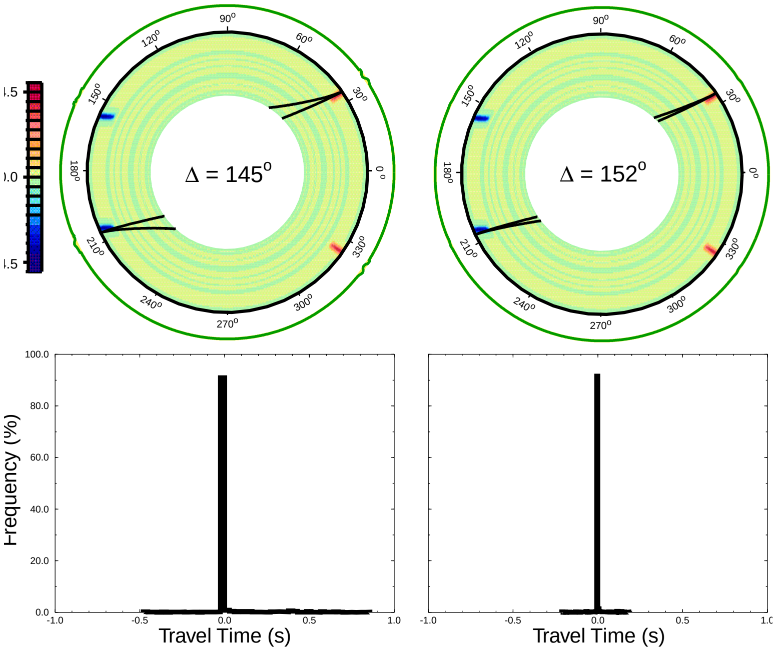

Same as in Figure 4.27 except that $\mathrm{PKP_{BC}}-\mathrm{PKP_{DF}}$ travel times are considered.

differential travel times than often assumed in inner core studies. For example, the upper mantle below Alaska contains a small-scale fast anomaly associated with the subducted slab. This feature may have the right structure for producing anomalously large $\mathrm{PKP_{BC}}-\mathrm{PKP_{DF}}$ observed for the path between South Sandwich Islands and Alaska. Another anomalous path is one between south of Africa and California. Extreme travel time values are often observed in the ray shooting exercise when one of the rays sample slow anomalies. There is a significant slow anomaly beneath Africa extending from the surface to the core-mantle boundary which structure may contribute to the large differential travel times observed.

The deep mantle structure produces diffuse variations in differential travel times, thus a strong correlation, such as that for the upper mantle structure, is not observed. This is probably because in the simulation models, anomalies near the core-mantle boundary are not as narrow as those near the surface. Global tomographic models are also dominated by long-wavelength features near the core-mantle boundary, but regional studies suggest that there may be rapid and considerable variations at the bottom of the mantle (e.g., Garnero et al., 1998). Such variations should produce large differential travel times because the ray separation is greatest in the deepest mantle.

There are several assumptions involved in these experiments, one of which is that the lateral perturbations in wave speeds are weak enough that the ray paths are not affected. Ray tracing studies indicate that lateral variations can bend rays considerably (e.g., Moser et al., 1992; Liu et al., 1998). Small amount of ray bending may make significant contribution, because it can change the ray separation considerably. In addition, the anomalies that are likely to produce large differential travel times are small, especially for $\mathrm{PKP_{BC}}-\mathrm{PKP_{DF}}$ data. For such small anomalies, ray theory may no longer be valid, and contributions from structures around the path may become important. Therefore, a numerical simulation of wave propagation is required in order to robustly establish the relation between narrow mantle structure and differential travel time anomalies.

4.8 Discussion

A simple model of inner core anisotropy, one that does not vary with radius, has been shown to satisfy normal mode, absolute and differential travel time observations. The differential travel times are not as well explained by this model as other data, but there are indications that variations in properties outside the inner core or small structures within the inner core are responsible for the misfit. In particular, residual differential travel times suggest that there may be a strongly heterogeneous region near the core-mantle boundary. The mantle model used to correct $\mathrm{PKP_{DF}}$ does not include this layer nor does the model derived from the mode inversion. Because $\mathrm{PKP_{DF}}$ data have better coverage, and since they are almost vertical when they enter or exit the core, the effect of the layer near the core-mantle boundary will be small. Similarly, deeply penetrating modes have a broad kernel near the core-mantle boundary, and the splitting due to this layer will not be substantial. Furthermore, the zonal component of the heterogeneity indicated by residual differential travel times is relatively small, so the effect on the zonal part of the splitting function, which is the component used in inner core modelling, is negligible. On the other hand, the non-zonal residual of inner core sensitive modes (Figure 4.18), may be related to the structure in the lower-most mantle.

The model of constant anisotropy contradicts the hypothesis that the inner core is isotropic near the inner core boundary (e.g., Song & Helmberger, 1998; Ouzounis & Creager, 2001; Song & Xu, 2002). Normal mode data can accommodate an isotropic layer of less than 150 km thickness, however, data from body waves penetrating shallowly in the inner core cannot be well explained by a model with an isotropic layer. Recent studies based upon waveform modelling propose inner core models with a ~ 250 km thick isotropic layer with a highly anisotropic ($\sim 8\%$) interior (Ouzounis & Creager, 2001; Song & Xu, 2002). Normal mode observations would not be consistent with this model, since the isotropic layer is too thick to fit modes which are only sensitive to the shallow part of the inner core, and the interior is too strongly anisotropic for modes with deeper sensitivity. In addition, $\sim 8\%$ anisotropy over-predicts $\mathrm{PKP_{DF}}$ data at distances above 150°.

Another complication in inner core anisotropy introduced by differential travel time observations is its hemispheric or quasi-hemispheric dependence. It is true that hemispherically averaged data show a distinct behavior between the eastern and western hemispheres, but the number of measurements used for each hemisphere differ greatly, and it is not clear how much of the hemispheric discrepancy originates from biased sampling. The inversion results show an unreasonably large difference between hemispheres, and the improvements in fit, by modelling the inner core in hemispheres, are only marginal. Physically, the inner core is thought to be homogeneous due to its slow growth within a homogeneous liquid (e.g., Jacobs, 1953). Even if the possibility of hemispheric variations is accepted, it will be difficult to explain large and discontinuous behaviour of travel times which is inconsistent with transverse isotropy. On the other hand, data from the two hemispheres are similar at small values of $\cos^2 \xi$. At some distance ranges, data from the two hemispheres exhibit baseline differences when $\cos^2 \xi$ is small, but this may be due to poorly constrained degree 1 structure in the mantle. A baseline shift cannot be easily related to anisotropy.

This study highlights the advantage of combining different types of data which are sensitive to inner core structure. In particular, normal mode data with less biased sampling of the inner core provide an invaluable constraint on anisotropy at a global scale. In addition, the attempt to derive a model which simultaneously satisfies normal mode, absolute travel time, and differential travel time data has allowed for the separation of signal from global anisotropy of the inner core, and identification of anomalous travel times. There are some signals, such as residual degree 2 order 2 in splitting function and the apparent difference of body wave data between the eastern and western hemisphere, that remain unexplained.

Chapter 5

Inner-Most Inner Core

5.1 Introduction

Anomalous behaviour of data from nearly antipodal distances has been noted in the earliest study of inner core anisotropy, although it has not been studied rigorously. The distribution of antipodal data in Figure 1 of Morelli et al. (1986) exhibits large positive travel times at mid-latitudes that are not observed at smaller distances. Later studies of inner core anisotropy using $\mathrm{PKP_{DF}}$ travel times are also characterised by models with considerably stronger anisotropy near the centre of the Earth (Su & Dziewoński, 1995; Tromp, 1995a). Stronger anisotropy at the central inner core is also inferred from the differential travel times of $\mathrm{PKP_{AB}}-\mathrm{PKP_{DF}}$ (e.g., Vinnik et al., 1994; Song, 1996) although these data may contain significant effects from mantle heterogeneities near the core-mantle boundary (e.g., Song & Helmberger, 1997; Bréger et al., 2000). Joint inversion of normal mode, differential and absolute travel time data has shown that a constant model of anisotropy, weaker than that inferred by the differential travel time studies can explain much of the signal in these data (Ishii et al., 2002a,b). However, arrival times of $\mathrm{PKP_{DF}}$ from distances between 173° and 180°, sampling the central 300 km of the inner core, exhibit large deviations from predictions (Ishii & Dziewoński, 2002).

Motivated by the poor fit, data from the epicentral distances between 173° and 180° obtained from earthquakes and stations shown in Figure 5.1 are examined in this Chapter. Unfortunately, most of currently available normal mode data are insensitive to structure in the central 300 km of the Earth. This lack of mode constraint is because sensitivity of a mode is determined based upon its eigenfunctions which must vanish at the centre of the Earth. Therefore, experiments are performed only with absolute travel times to test if observed deviations are robust features associated with globally coherent change in anisotropy, and if the material still exhibits transversely isotropic behaviour at the centre of the core. In addition, data are analysed for the location of the best-fitting symmetry axis. Several tests are performed to determine how the inferred location is influenced by data distribution, prescribed weighting, and some anomalous paths.

5.2 Data Robustness

The constant anisotropy model obtained from joint inversion of mode and body wave data explains the absolute travel times well, except between 173° and 180° (Figure 5.2*a* and *b*). In particular, the residuals from the antipodal distances show strong dependence on $\cos^4 \xi$ (Figure 5.2*d*). The large deviations observed at this distance range may be associated with structure in the deepest inner core, but it is also possible that they are due to biased sampling. For example, the datum from the 153°–155° distance range with $0.8 \leq \cos^2 \xi < 0.9$ has been strongly biased by data from the path between South Sandwich Islands and Alaska (Figure 5.2*c*). When data from this path are

Figure 5.1: Distribution of Earthquakes and Stations for Antipodal Data

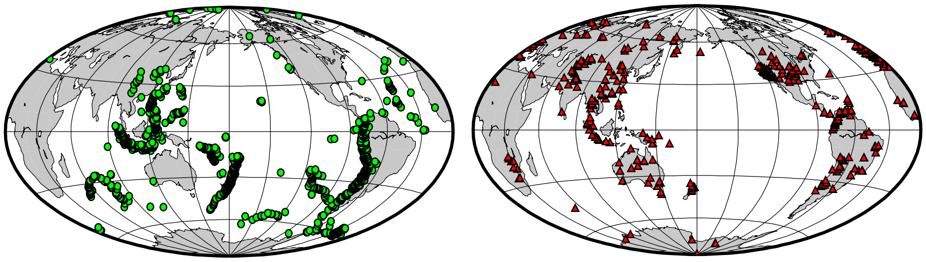

Distribution of nearly 1800 earthquakes (left) and 400 stations (right) for which $\mathrm{PKP_{DF}}$ arrival times at the distances of 173° to 180° are reported.

removed, the residuals at $\cos^2\xi = 0.65$ and 0.75 are close to zero. In the following investigations, data are corrected for effects of anisotropy in the upper 920 km of the inner core using the constant anisotropy model SPRI0 (Ishii et al., 2002a) to focus on the deviations from the SPRI0 model.

To begin, data are divided into four subsets on the basis of their bottoming points as discussed in the previous Chapter (Figure 5.3). If data dependence on $\cos^2\xi$ is due to a limited number of isolated data or regional variations, the four curves should differ from one another. Correspondingly, consistency in the curves suggests that the signal is associated with global anisotropy. In the distance range 153°–155°, the four curves all lie close to zero up to $\cos^2\xi$ of 0.6, then they diverge significantly with clear difference between the eastern and western equatorial data (Figure 5.3*a*). These curves indicate that the constant anisotropy model has explained most signal associated with global structure, and the residuals cannot be modelled for additional global anisotropy. In contrast, data from the 173°–180° distance range are non-zero and show coherent variations when $\cos^2\xi < 0.8$: all four sets of data are negative when $\cos^2\xi$ is small, increase to a maximum of about +1 second between $\cos^2\xi$ of 0.3 and 0.5, and decrease to large negative values (Figure 5.3*b*). When $\cos^2\xi > 0.8$, data from the eastern and western equatorial groups differ considerably, but there are only 19 measurements in all, thus they are not a reliable measure of the data trend. Consistency of the four data subsets at $\cos^2\xi < 0.8$ (where there are more than 3000 measurements) suggests that the misfit in Figure 5.2(*b*) is due to a change in global anisotropic properties within the central inner core.

5.2.1 Latitudinal Average Stacking

Longitudinal dependence of inner core anisotropy, in the form of hemispheric variation, has been proposed by studies based mainly upon differential travel time data (e.g., Tanaka & Hamaguchi, 1997; Creager, 1999; Garcia & Souriau, 2000; Niu & Wen, 2001). To test if there is strong longitudinal dependence, travel times are average using ray angle ξ and bottoming longitude ϕ_b. Consequently, any latitudinal variations are averaged, hence this averaging scheme is called "latitudinal average stacking". Two locations are assigned to each measurement, $\pm(90° - \xi)$ latitudes and ϕ_b east-longitude, which are used for cap averaging. For example, travel time of a ray almost parallel to the symmetry axis is binned into caps near the north and south poles. In contrast, a ray travelling almost perpendicular to the symmetry axis is averaged into caps at the equator regardless of its bottoming latitude. If anisotropy varies regionally, if there are anomalous paths, or if the material is not transversely isotropic, the distribution of latitudinally averaged data will not be dominated by zonal pattern at degrees 2 and 4 (equation 2.20).

For both 153°–155° and 173°–180° distance ranges, data coverage of latitudinal average is good even though each cap is required to have at least three measurements (Figure 5.4*a*). It should be remembered that there is no simple correspondence between the location of source or receiver at

Figure 5.2: Observed and Residual Absolute Travel Times

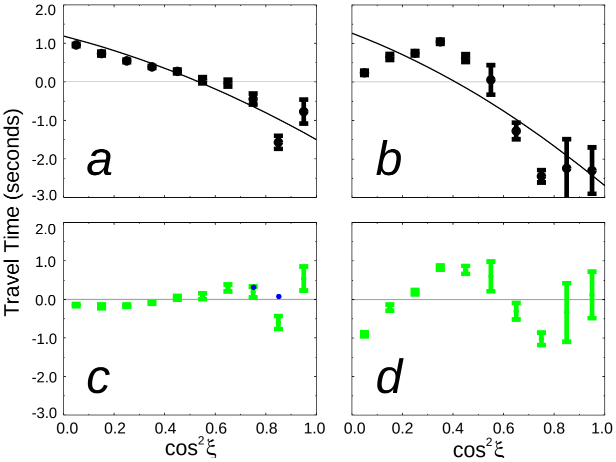

Comparison of data from the 153°–155° distance range, corresponding to bottoming depths of 275 to 360 km below the inner-core boundary (left) and from the 173°–180° distance range with bottoming depths in the central 300 km of the core (right).

(*a*) and (*b*) Observed travel times (black circles with error bars) in comparison to predictions using constant anisotropy model SPRI0 (Ishii et al., 2002a; black curve) with zero line in grey. Standard deviation of the mean is shown as the error bar.

(*c*) and (*d*) Residual travel times (green circles with error bars) after the effects due to constant anisotropy model have been removed. The blue circles in (*c*) are residuals if data from the anomalous path between South Sandwich Islands and Alaska are excluded. Note that the constant anisotropy model slightly overpredicts the data trend without the anomalous data.

Figure 5.3: Residuals of Four Data Subsets

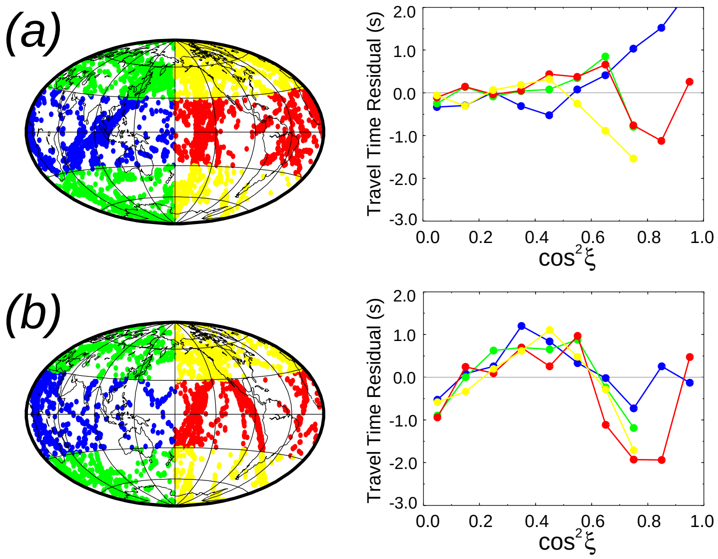

Travel time residuals from each quadrant as discussed in the previous Chapter are plotted as a function of $\cos^2\xi$ with colours identifying the bottoming region: blue corresponds to east equatorial; green corresponds to east polar; red corresponds to west equatorial; and yellow corresponds to west polar. The thin grey line is the zero line.

(a) Data from the distance range between 153° and 155°. There are ~ 12000 measurements from this distance range.

(b) Data from the distance range between 173° and 180°. There are more than 3000 measurements from this distance range.

Figure 5.4: Latitudinal Average Stacking

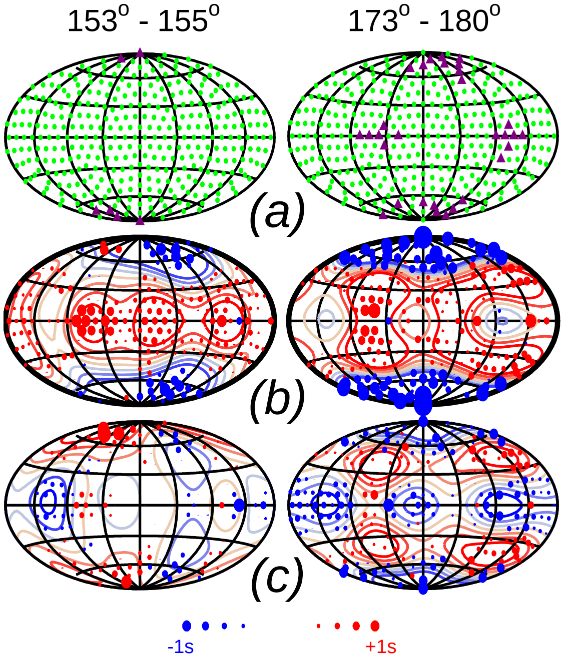

Results of the latitudinal stacking compared between the distance ranges 153°–155° (left) and 173°–180° (right).
(*a*) Data coverage. Green dots indicate caps with more than 3 measurements and purple triangles are those with less than 3 measurements. Note that the coverage is good for both distance ranges.
(*b*) Cap averages where the size and colour of circles give the magnitude and sign of the observed travel times before inner core correction. Background curves show the spherical harmonic expansion of averaged data using angular degrees up to and including 4. Data coverage and distribution should be symmetric across the equator because each measurement is assigned to $\pm(90^\circ - \xi)$ latitude. However, non-symmetric distribution of caps distorts this symmetry.
(*c*) Same as in (*b*) except that data have been corrected for effects due to the upper 920 km of the inner core.

the surface and ray bottoming coordinates. Even regions with a limited number of earthquakes (e.g., much of the Pacific) can be covered well by the ray bottoming points; mantle tomography is an instructive example (e.g., Figure 8 of Boschi & Dziewoński, 1999). Averaging the raw travel times before inner core correction results in a clear zonal pattern for both 153°–155° and 173°–180° distance ranges (Figure 5.4*b*). However, when effects due to anisotropy in the upper 920 km of the inner core are removed, residuals from the two distance ranges are significantly different. Residuals in the 153°–155° are almost zero with a weak degree 2 signal and considerable small-scale variations (Figures 5.4*c*). The South Sandwich Islands to Alaska anomalies show up as large negative values in the western hemisphere at high latitudes (Figures 5.4*c*). Note that variations at hemispheric scale are not observed consistently at all latitudes (ray angles), and are only obvious near the poles. In contrast, residuals from the 173°–180° distance range are much bigger than those from the 153°–155° range, and have coherent degree 4 zonal pattern. This indicates that the signal associated with the central 300 km of the inner core can be modelled by transverse isotropy with significantly different characteristics than the bulk inner core.

Figure 5.5: Power of Spherical Harmonic Coefficients Obtained from Latitudinal Averages

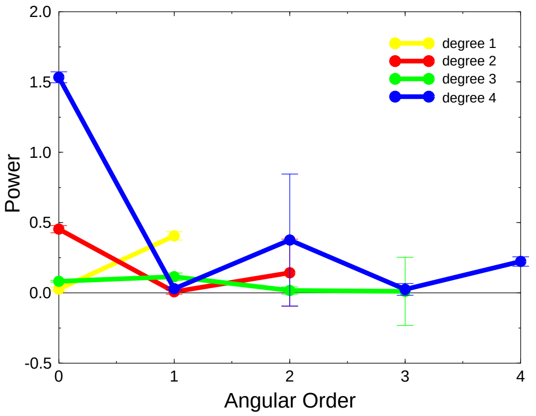

Average power (circles) of each spherical harmonic coefficient as a function of angular order using 100 data sets generated by random sampling. The error bars correspond to the standard deviation.

In order to quantify the dominance of zonal component at degree 4 and to determine its uncertainty, a Monte-Carlo simulation is performed. The number of travel time measurements for a given distance range is kept the same as used in obtaining Figure 5.4, but a new set is defined by randomly picking data from the original set, allowing for multiple inclusions. Latitudinal averages are calculated for each data set, and the spherical harmonic coefficients obtained from the averages are analysed. Coefficients between degrees 1 and 4 are compared in Figure 5.5. The zonal component at degree 4 has strongest power by far.

These results do not change even when the imposed symmetry across the equator is removed (Figure 5.6*b*). The South Sandwich Islands to Alaska data are further isolated in the 153°–155° data distribution. Although non-zonal component is still dominant, data from 153°–155° distance range show somewhat stronger zonal pattern than in Figure 5.4(*b*), suggesting that the constant anisotropy model used to remove effects of the upper 920 km may be slightly over-estimated due to data from the anomalous path. At antipodal distances, the degree 4 zonal signal persists (Figure 5.4*c*) even though the data coverage is poorer (Figure 5.6*a*). The unique behaviour of data sampling the deepest part of the Earth appears robustly related to behaviour of the inner-most inner core as a whole.

5.3 Axis of Symmetry

In this section, the antipodal data are analysed for the location of the symmetry axis. A systematic search for the axis is performed, and uncertainties due to data coverage, weighting, and anomalous paths are addressed. In order to test robustness, results of the symmetry axis search using different averaging schemes are compared.

5.3.1 Cylindrical Average Stacking

When searching for the axis of symmetry, data averaged by $\cos^2 \xi$ or using bottoming longitude ϕ_b are not the most convenient, since averaging must be performed for each axis location. There is a better averaging scheme for this purpose which does not require data processing with a change in the symmetry axis, i.e., a scheme that preserves the ray direction of individual measurement. Following

Figure 5.6: Non-Symmetric Latitudinal Average Stacking

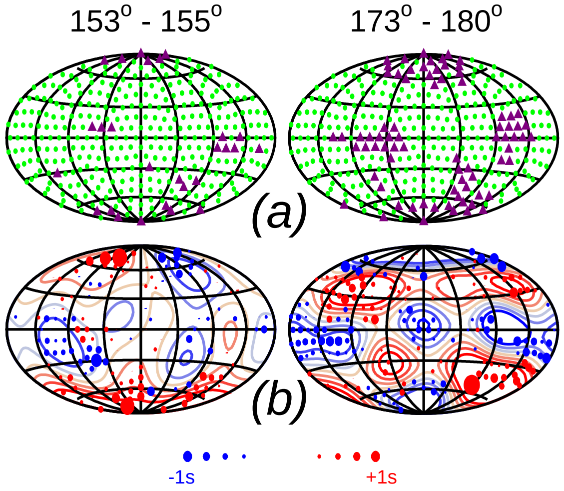

Results of the latitudinal stacking compared between the distance ranges 153°–155° (left) and 173°–180° (right).

(*a*) Same as in Figure 5.4(*a*) except that the symmetry across the equator is broken. Each datum is assigned to a single location on the unit sphere (ϕ_b and absolute latitude of ($90^\circ - \xi$ with sign determined by the bottoming latitude) instead of two (ϕ_b and $\pm(90^\circ - \xi)$). The coverage deteriorates slightly compared to (*a*).

(*b*) Distribution of cap averages using the non-symmetric method described in (*a*) for data corrected for the effect of anisotropy due to the upper 920 km of the inner core.

Figure 5.7: Cylindrical Average Stacking

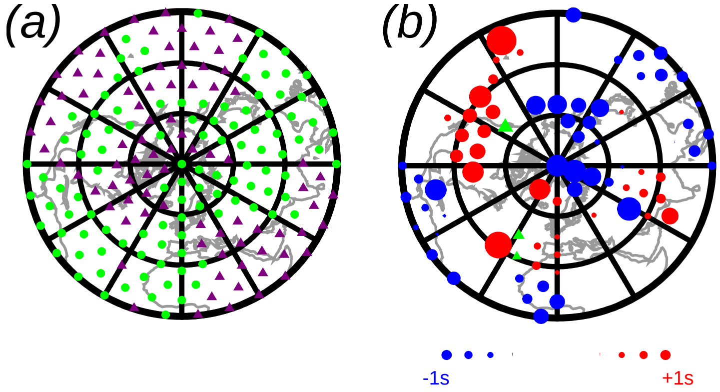

(a) Data coverage for cylindrically averaged data from the 173°–180° distance range. Green circles are cap locations with more than 3 measurements, and purple triangles are cap locations with less than 3 measurements. The north pole and the equator are at the centre and periphery of the map, respectively. For reference, coast lines are shown in grey. Because ray translation is small for antipodal data, the coverage approaches the distribution of earthquakes and stations.
(b) Cylindrically stacked data with magnitude and sign of the residuals indicated by the size and colour of circles, respectively. There are three unusually large positive residuals (> 4 seconds) which are shown by green triangles. In the inversion, data at the equator are included only if cap longitude is between 0° and 180°. To illustrate spatial variations, global average has been removed from these data.

Su & Dziewoński (1995), each ray path is translated to the centre of a unit sphere, and the two intercept points of the ray and the unit sphere, at $\pm(90°-\xi)$ latitudes and ϕ_c or $\phi_c+180°$ longitudes, are used to calculate the cap averages. This averaging scheme is referred to as "cylindrical average stacking". Physically, this method averages data from parallel rays, and implies that the angle between any axis of symmetry and a given cap average is the ray angle. Note that this scheme is not optimal when investigating the lateral variations of anisotropy or identifying anomalous paths, because data sampling different parts of the inner core (e.g., eastern and western hemispheres) will be averaged if the rays are parallel.

5.3.2 Results

Initially, data are averaged using the cylindrical stacking technique. There is an implicit 180° symmetry in the averaged data, hence only those with positive ray angle latitudes are included in the analysis. This gives 102 caps with more than 3 measurements with large regions without data such as under the Pacific (Figure 5.7a). The values of cylindrical averages (Figure 5.7b) are rather extreme: they are either close to zero or very large (> 1 second). In particular, there are three caps (shown by green triangles in Figure 5.7b) with unusually large positive values (> 4 seconds). These anomalous cap averages are included in the data set for inversion, but their effects on axis location are investigated later in this section. These data are inverted for values of spherical harmonic coefficients at degrees 0, 2, and 4 in equation (2.20), i.e., the best axis location is the one around which data show strongest cylindrical (i.e., zonal) distribution. The symmetry axis locations that are changed systematically in inversions to determine the location where data are well explained. However, data coverage is neither complete nor uniform (Figure 5.7a), which will influence the axis location significantly.

The distribution of variance reduction as a function of axis location shows that the geographic pole is not the best axis location for the cylindrically averaged data (Figure 5.8*a*). In fact, the data have strongest zonal pattern when the axis is tilted to near 120°E 35°N. This may be the axis of symmetry, but it may also be an artifact of the inversion process; data distribution, weighting, and spatially limited anomalous data, can tilt the symmetry axis.

With uneven data coverage, the axis location tends to be pushed towards a point around which the holes in data coverage appear zonally. This effect can be mapped by setting both cap averages d_i and the weighting ω_i in equation (2.21) to unity and solving for the spherical harmonic coefficients at degrees 2 and 4. Note that the degree 0 term is intentionally ignored. The current coverage with the cylindrically averaged data (Figure 5.7*a*) favours the symmetry axis to be beneath Somalia even though the real axis may be somewhere else (Figure 5.8*b*). Prescribed weighting on data can distort the axis locations in a similar manner. For example, if there is a datum with unusually large residual, a strong weighting on this datum will bring the maximum variance reduction to a location near it, although a weak weighting may put the maximum elsewhere. Setting all data values to unity and solving for m in equation (2.21) shows the combined effects due to weighting and data coverage on the axis location (Figure 5.8*c*). If the axis of symmetry inferred from data is at one of the locations preferred by weighting and coverage, its robustness is questionable.

The second factor that might influence the tilt of the symmetry axis is anomalously large data. For example, the axis of symmetry for the inner core was inferred to be tilted by $\sim 10°$ (Su & Dziewoński, 1995). However, it was later demonstrated to be a biased result due to travel times from the South Sandwich Islands to Alaska path (Dziewoński & Su, 1998). To investigate if results for the inner-most inner core suffer from similar effects, a cap average and its neighbours are systematically removed from data set, and changes in the location of maximum variance reduction are monitored. The neighbouring caps are removed due to the extensive cap overlap, since measurements from a single path can be averaged into several caps. Inversions with 102 data subsets show that the locations of maximum variance reduction cluster around 120°E 35°N except for three subsets where locations near 50°W 50°N are preferred (Figure 5.8*d*). Inspection of the three unwonted data sets reveals that the removal of western North America data creates a strong preference for the axis to be near 50°W 50°N due to data coverage. Inversion of the three subsets also show that the local maximum near 120°E 35°N is still well-defined, therefore the three deviants in Figure 5.8(*d*) are likely to be artifacts.

The effects due to the three large positive data ($>$ 4 seconds) shown by triangles in Figure 5.7(*b*) must also be examined. Because these data are given small weight in the inversion, removing these values from the data set does not change the results significantly, i.e., the distribution of variance reduction is similar to that in Figure 5.8(*a*). The only noticeable change is that a local maximum near the pole becomes better defined than in Figure 5.8(*a*). It appears then that the symmetry axis is robustly located near 120°E 35°N based upon cylindrically averaged data. Up to now, the weights are calculated by taking average of weight assigned to individual measurement as described by Su & Dziewoński (1995). Experiments with weighting values which are constant, based upon number of measurements, and the standard deviation produce the maximum near 120°E 35°N consistently, even though some weighting schemes give additional maxima with high variance reductions.

On the other hand, there is a disadvantage in using cylindrically averaged data at antipodal distance range. This is demonstrated by looking at the largest positive cap average (the largest triangle in Figure 5.7*b*). The value of 7 seconds is obtained by averaging 5 measurements. Although there are enough measurements to average, the 5 measurements are from 5 different earthquakes recorded at a single station. Recall that calculation of averages for absolute travel times was motivated, because ISC data suffer from station specific errors. Indeed, unusually large cylindrical averages occur when there are less than 5 stations contributing to the cap average (Figure 5.9*a*). Almost half of the cylindrically averaged caps have less than 5 stations (Figure 5.9*b*) whereas for latitudinal averaging, it is less than 15% (Figure 5.9*d*). This seems to be the reason why there is less scatter in latitudinally stacked data (Figure 5.9*c*). Note that variation of cylindrical averages at ±2 seconds

Figure 5.8: Symmetry Axis Location Using Cylindrical Average Stacks

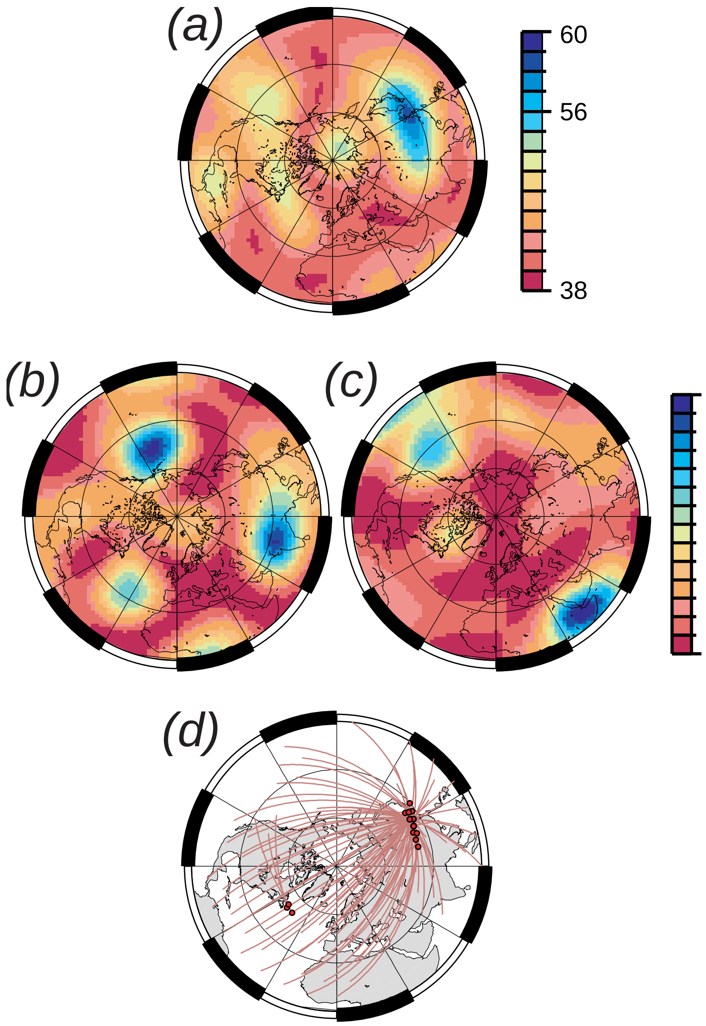

(a) Variance reductions obtained as a result of inverting cylindrically averaged data at various axis locations. The colour scale is linear between 38 and 56% as well as between 56 and 60%.
(b) Effects of uneven data coverage on axis location.
(c) Effects of data coverage and weighting on axis location.
(d) A plot of maximum variance reduction locations (red circles) when a datum and its neighbours are removed systematically and the set of inversions as in (a) is performed for each data set. The endpoint of each red curve corresponds to the location of the central datum removed from the inversion. On the average, 5 to 6 cap averages are removed from the complete data set.

Figure 5.9: Cap Averages as a Function of the Number of Stations

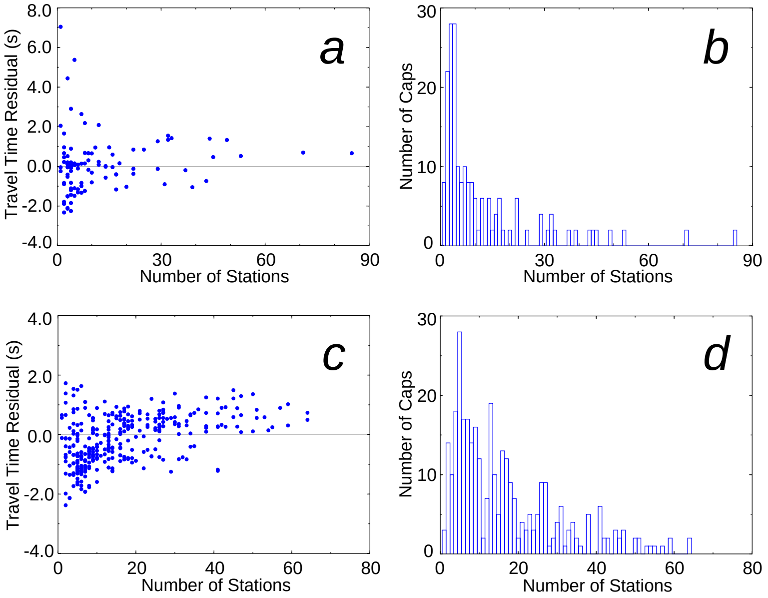

(*a*) and (*c*) Cap averaged travel times as a function of the number of stations contributing to a cap. (*a*) is for cylindrically averaged stacks and (*c*) is for latitudinally averaged data with the symmetry axis at the geographic pole. Data from both the northern and southern hemispheres are considered. Note that the scales on axes are different for (*a*) and (*c*).
(*b*) and (*d*) Number of caps as a function of the number of stations. (*b*) and (*d*) are based upon the cylindrical and latitudinal averaging, respectively. There are 86 cylindrically averaged caps out of 204 with measurements reported from less than 5 stations. In contrast, the numbers become 45 out of 332 for the latitudinal averaging scheme.

level is not due to some station specific errors (Figures 5.9*a* and *c*).

Considering that the results using the cylindrical average stacking may suffer from station errors, another set of inversions is performed using data averaged only in $\cos^2\xi$. Since measurements are grouped into 10 bins, there are more data available for each average, reducing the undesirable station effects. Resulting distribution of variance reduction as a function of the axis location has local maxima near those obtained using cylindrical averages (Figure 5.10). However, the highest variance reduction occurs when the axis is under western North America, and there are two maxima near 120°E 35°N, one south of Japan, and another within China. High variance reduction at western North America is partly due to the reduced number of data. This axis location is such that there are not enough measurements between $\cos^2\xi$ of 0.6 and 0.8, and only a small number of measurements are available for $\cos^2\xi$ ranges of 0.5–0.6, and 0.8–0.9. So the maximum at western North America is associated with poor data coverage. In contrast, none of the locations of high variance reduction give satisfactory result for latitudinally averaged data. In fact, the rotation axis is the preferred axis based upon this averaging scheme. These discrepancies indicate that it is premature to identify the location of the symmetry axis with current set of absolute travel time measurements. In the following section, anisotropy of the inner-most inner core is determined assuming that the axis of symmetry is at the geographic pole.

Figure 5.10: Symmetry Axis Location with Data Averaged by $\cos^2 \xi$

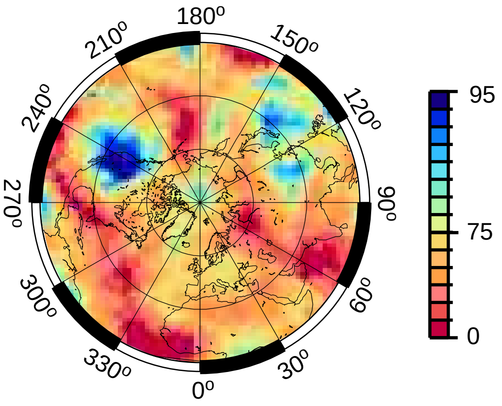

Same as Figure 5.8(a) except that the data used in the inversions are averaged only in terms of $\cos^2 \xi$. The colour scale is linear between 0 and 75%, and between 75 and 95%.

5.4 Anisotropy of the Inner-Most Inner Core

The $\mathrm{PKP_{DF}}$ signal associated with the central 300 km of the inner core is so poorly predicted by the constant anisotropy model SPRI0 that the variance reduction is -15%. Inverting these data results in a model which predicts dominant dependence of travel times on $\cos^4 \xi$ (Figure 5.11a), and the variance reduction is substantially better, 87%. The values of ϵ and σ for the inner-most inner core are 3.7 and -20%, respectively, which are much larger than those for the bulk inner core (1.8 and -0.67%, respectively). In terms of compressional wave speed variations with ray angle, the two models of anisotropy differ in two respects (Figure 5.11b). The direction of slowest wave propagation is perpendicular to the rotation axis for the bulk inner core model but is about 45° from the axis for the inner-most inner core. In addition, the difference in wave speed between fastest and slowest directions are different by a factor of four, 0.2 and 0.8 km/s for bulk and inner-most inner core, respectively.

Such a dramatic change in anisotropy at 300 km radius should produce seismically observable effects. For example, a reflected wave is expected if there is a sharp transition in wave speed. Furthermore, depending upon whether the wave speed increases or decreases toward the centre, different phases should be observed at different epicentral distances. If the wave speed increases, such as when the ray is travelling parallel to the rotation axis (Figure 5.12a), the reflected phase and the ray travelling through the inner-most 300 km of the core produce a triplication (Figure 5.12b). In contrast, a decrease in wave speed, such as when the ray is travelling at 45° from the rotation axis, results in a shadow zone, followed by pro- and retro-grade phases from rays travelling through the inner-most inner core (Figure 5.12c). However, details of such predictions are affected by parameters which are not well-constrained by the current data set. For example, the discontinuity at 300 km radius is introduced for convenience: data used in the inversion cannot determine how rapidly or gradually the transition in anisotropic property occurs. In addition, tilt of the symmetry axis will bring additional complexity, because a given ray angle within the bulk inner core can have variety of ray angles within the inner-most inner core if the axis of symmetry is different for two regions of the inner core.

Figure 5.11: Model of the Inner-Most Inner Core

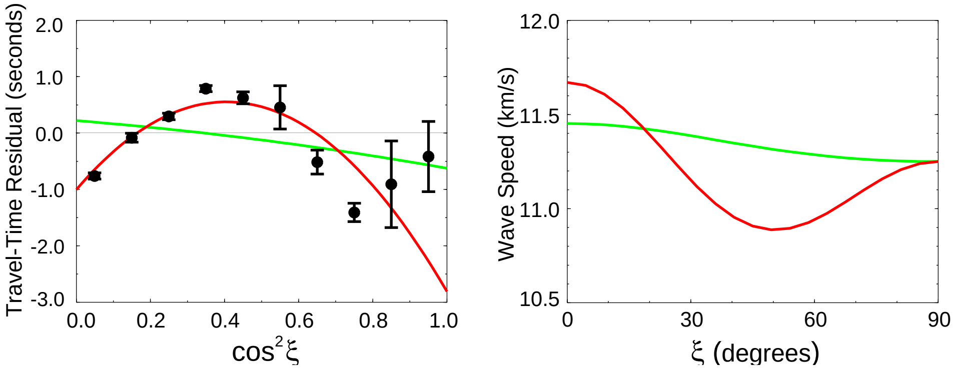

(*a*) $\mathrm{PKP_{DF}}$ data associated with the central 300 km of the inner core (black circles with error bars given by standard deviation of the mean) and predictions based upon the bulk (green) and inner-most (red) inner core anisotropy models.
(*b*) Compressional wave speed variations as a function of ray angle ξ for the two anisotropy models. Note that because the x-axis is ξ and not $\cos^2\xi$, rays parallel to the rotation axis are on the left of the plot.

5.5 Discussion

The absolute $\mathrm{PKP_{DF}}$ travel time data between 173° and 180° distance have considerably different characteristics compared to data from smaller distances. These antipodal data show robust variations with the ray angle which implies that the property of the inner-most inner core can be described sufficiently by transverse isotropy, and that higher order anisotropy is not necessary. Analysis of data suggests that the symmetry axis may be tilted far from the geographic pole, somewhere near 110°E 35°N, but better quality and quantity of data are required for more definitive and precise determination of the symmetry axis location. However, inversions with different axis locations consistently produce models of anisotropy which are substantially different from that of the bulk inner core. The model of the inner-most inner core with the symmetry axis at the geographic pole is characterised by fast and slow wave propagation directions that are parallel and 45° to the rotation axis. The difference between the maximum and minimum wave speeds is four times greater than that of the bulk inner core.

Theoretical calculations of the elastic parameters of iron, the main constituent of the Earth's core, predict a minimum in compressional wave speed at $\sim 50°$ from the direction of maximum speed (Steinle-Neumann et al., 2001). Experimental results at high pressures also indicate that the lowest speed occurs at $\sim 45°$ from the direction of fastest wave propagation (Mao et al., 1998). Although these two results do not agree in the fast direction, they are consistent with the inner-most inner core model if there is a mechanism that aligns the fast axis with the axis of rotation. In addition, in both of these mineralogical studies, iron is found to be highly anisotropic with a wave speed difference of $2 \sim 2.5$ km/s, suggesting that only a fraction of crystal alignment is required to generate the anisotropic signal observed for the inner-most inner core.

Figure 5.12: Travel Time Predictions Associated with the Inner-Most Inner Core

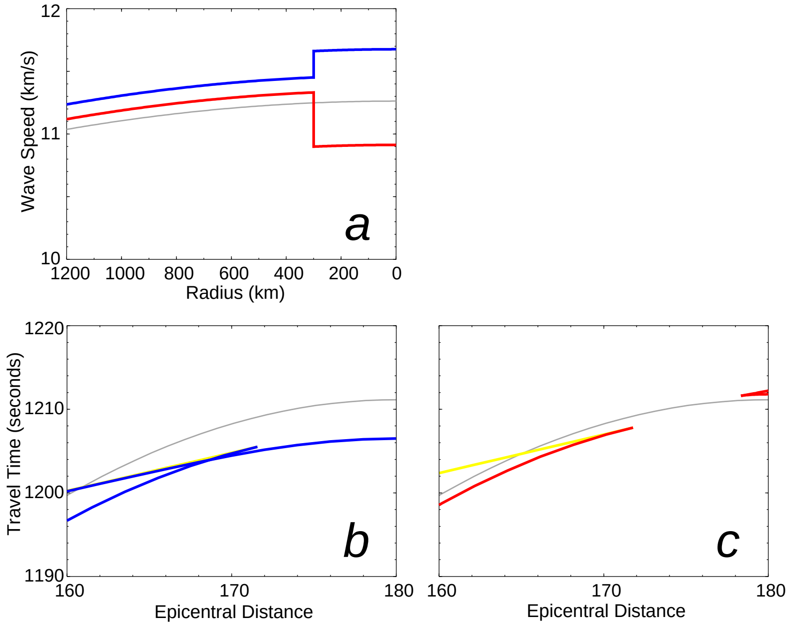

(a) Changes in the compressional wave speed with radius. Assuming that the symmetry axis is always at the poles, wave speeds for rays travelling parallel (blue curve) and at 45° (black dashed curve) to the rotation axis are compared with wave speed in PREM (Dziewoński & Anderson, 1981; grey thin curve). Note that the wave speed decreases from bulk to the inner-most inner core if the ray is travelling at 45° angle from the symmetry axis, but increases if the ray is parallel to the axis. No offset is included (i.e., the value of η_0 in equation (2.16) is ignored).

(b) Travel time prediction for a ray travelling parallel to the symmetry axis (blue curve). Because the speed increases in the inner-most inner core, there is a triplication. Reflection from the discontinuity at 300 km radius is shown by yellow curve which is barely visible on this plot.

(c) Travel time prediction for a ray travelling at 45° from the symmetry axis (red curve). Because wave speed decreases at the centre, there is a shadow zone between 160° and 170° distances followed by pro- and retro-grade phases.

Chapter 6

Summary Discussion

The previous Chapters offer models of the mantle and the inner core that contain both expected and surprising features. There are vast implications, and the models give insight into the current state and possible evolution process occurring within the Earth. In this Chapter, some consequences of the models not focused on in earlier Chapters are presented, along with discussion of other approaches and data available to better understand the internal structure of the Earth.

6.1 Mantle

The distribution of density anomalies show unexpected de-correlation from wave speed models. However, this observation is consistent with mounting evidence that the lower-most mantle contains variations in both temperature and chemistry. Seismological studies using various data and methods draw similar conclusions (e.g., Su & Dziewoński, 1997; Ritsema et al., 1998; van der Hilst & Kárason, 1999; Masters et al., 2000c; Ni et al., 2002) as well as mineralogical consideration of the scaling ratio (Karato & Karki, 2001). Attempts to separate temperature and composition contributions to seismic wave speed variations, using temperature and composition derivatives given by experiments, indicate that variations in seismic waves alone cannot reliably distinguish the two contributions (Forte & Mitrovica, 2001). Density model adds valuable constraints for this problem, although such investigations also require well-determined derivatives from mineral physics.

Density models can also be used to probe the dynamics of the mantle. For example, calculation of the local Bullen parameter (determined in a similar manner as laterally varying scaling ratios) suggests that values for the plumes in the lower-most mantle are consistent with a thermo-chemical origin of these plumes (Matyska & Yuen, 2002). Moreover, the Bullen parameters obtained using the density model imply that the mantle is not as adiabatic as commonly assumed. This view of the mantle has significant impact on a wide range of geosciences. In addition, studies of mantle rheology can utilise the density model rather than converting seismic wave speed models to density distributions. Because the density model differs considerably from wave speed models, it may lead to a viscosity profile that is unlike existing models.

These applications assume that the density model reflects the real density distribution within the mantle. There is a debate on the resolvability of density variations using mode data, and most studies argue that the sensitivity is not sufficient to constrain density heterogeneities independently (e.g., Resovsky & Ritzwoller, 1999b; Romanowicz, 2001; Masters et al., 2000b; Kuo & Romanowicz, 2002). These studies use various techniques on mode data to obtain greatly differing models, but the data set is often different from study to study. In some cases, only a small number of data is used. Furthermore, some studies make certain assumptions, such as confining density variations within a given layer, which are unrealistic. Chapter 3 addressed issues of resolution, but a discussion on potential improvements in density modelling from future data set appears appropriate.

The splitting function coefficients used in this study by no means represent the full data set that can be extracted from normal modes. There are modes whose splitting coefficients have not yet been measured, and the angular degree s of splitting coefficients can be extended to higher values. Consideration of splitting coefficients with larger angular degree allows for modelling of smaller structure both in wave speed and density perturbations. On the other hand, additional splitting data from currently unavailable modes provide better constraints on wave speed variations but not very much on density. This is because the density sensitivity kernel become oscillatory in radius, i.e., these modes approach the body wave regime. Splitting data from coupled modes are not abundant and are practically ignored in this study, but they can provide further constraints on even, as well as odd, degree structures. It has also been noted that the effects of mode interaction may be more significant than is generally assumed, even for isolated modes (Deuss & Woodhouse, 2001). This influence may affect splitting coefficient measurements, and subsequently alter mantle structure. Therefore coupled mode analysis is necessary to improve the mode database for better constraining the internal structure.

Because many modes, for which gravitational restoring force is important, have already been analysed, a dramatic improvement on the resolution of low degree density structure seems unlikely from future mode measurements. Alternatively, one can look for better constraints on seismic wave speeds. If seismic wave speed variations are known perfectly, the density contribution to splitting functions can be isolated and modelled. It is impossible to have perfect wave speed models, but there are numerous data for improving these models. Additional mode splitting, body waves, and surface wave data can be inverted simultaneously to obtain perturbations in wave speed (e.g., Bolton, 1996; Masters et al., 1996). Better wave speed models may help to limit trade-off between density and wave speed variations.

There are also non-seismological data with sensitivity to density within the mantle. One of these, the free air gravity anomaly, has been modelled in Chapter 3 based upon a static approach using topography on various discontinuities. Replacing topography by viscosity, i.e., switching to a dynamic approach, will permit inclusion of other geodynamical data for density modelling. Such data, e.g., glacial rebound and plate velocity, have poor depth resolution, but will provide much desired information about low degree structure. However, there will inevitably be a trade off between density and viscosity, and combining the linear mode problem with non-linear geodynamic data may not be simple.

Finally, there are neutrinos. Two flavours of neutrinos exist, electron and mu, and the transformation of one flavour to another, called neutrino oscillation, is sensitive to the density of the medium in which neutrinos travel. In theory, this sensitivity can be exploited to constrain internal density variations of the Earth. However, neutrinos are easily altered by small changes in density, much smaller than the uncertainty associated with the radial density profile. In addition, obtaining good coverage, i.e., depth resolution, is difficult, if not impossible. To relate neutrino oscillation to density variations, one must have a controlled neutrino source (rather than neutrinos from the Sun), which are distributed more sparsely than earthquakes. It is also unlikely that a world-wide network of expensive neutrino detectors will be available in the near future to improve coverage. Therefore the prospect of neutrino tomography seems improbable.

Chapter 3 investigates large-scale variations in elastic parameters and density within the mantle, but one aspect not considered here is the lateral variations in attenuation. This structure is difficult to constrain, because signal due to attenuation is hard to distinguish from other effects such as focusing and defocusing. Nonetheless, lateral variation in attenuation has been estimated using body and surface wave data (Reid et al., 2001; Romanowicz & Gung, 2002). If the imaginary part of the splitting matrix H (equation 2.3) can be constrained reliably, it will be possible to constrain large-scale variations in attenuation using normal mode data.

6.2 Inner Core

The mechanism responsible for development of anisotropy of the inner core is not understood, but there are various hypotheses. Preferential alignment of iron crystals at the inner-core boundary during inner core growth has been argued as one possible mechanism. This type of models rely on the effects of spheroidal (Karato, 1993b) and toroidal (Buffett & Wenk, 2001) magnetic fields, or texturing produced by rotation (Bergman, 1997). These processes predict anisotropy that is strongest at the surface without much variation with radius. Alternatively, flow within the inner core may align iron crystals. Thermal convection driven by internal heating is a possibility (e.g., Jeanloz & Wenk, 1988), although it is difficult to put radiogenic elements into the inner core (e.g., Ito et al., 1993; Parker et al., 1996). Other hypotheses include flow induced by Maxwell stresses (Karato, 1999) or by preferential growth of the inner core along its equator due to uneven heat removal by outer core convection (Yoshida et al., 1996). In the latter model, the inner core tries to return to its hydrostatic equilibrium position, driving flow to align crystals (Yoshida et al., 1996). Anisotropy due to large-scale internal flow is likely to vary little with radius. Another mechanism for inner core anisotropy involves survival of domains that are aligned with the lowest strain energy within the inner core (Stevenson, 1996; Song, 1997). This process predicts increasing crystal alignment with depth.

Because discrepancies exist in the fast and slow directions of hexagonal close packed iron crystals under inner core conditions (e.g., Stixrude & Cohen, 1995; Mao et al., 1996; Steinle-Neumann et al., 2001), observed anisotropic behaviour cannot be used to determine which of the above hypotheses are more probable than others. For example, the two arguments using spheroidal and toroidal magnetic fields (Karato, 1993b; Buffett & Wenk, 2001) predict crystal alignments which are perpendicular to one another. However, there are mineral physical estimates of iron with fast directions differing by 90°, so either mechanism can be compatible with observed anisotropy. On the other hand, changes in anisotropic strength with radius can be used to distinguish various hypotheses. The simple radial profile of SPRI0, suggests that the preferential survival of domains as the cause of anisotropy is unlikely.

The requirement of anisotropy near the inner core boundary provides another constraint on the manner of inner core growth. A mushy zone at the top of the inner core has been proposed to occur as a transition zone from liquid to solid core (e.g., Fearn et al., 1981). This layer must be very thin to accommodate anisotropy observed near the inner core boundary. In fact, this observation is consistent with an earlier demonstration of sharp transition from outer to inner core based upon high frequency waves reflected from the inner core boundary (Engdahl et al., 1970).

Although the simple anisotropy model reconciles a variety of seismic observations, there are several outstanding questions, such as the source of apparent hemispheric dichotomy and residual splitting functions. Unlike the density model of the mantle, these questions can be addressed with improved databases and approaches. For example, splitting measurements of more inner core modes will determine if higher order anisotropy or superposition of two different transversely isotropic models is required to explain the residual signal. Better quality and quantity of travel time data will allow for identification of the source of anomalous observations. In particular, better station coverage may provide data from rays travelling in different directions for a given portion of the inner core, such as the part sampled by the South Sandwich Islands to Alaska path. This would be ideal in distinguishing whether the extreme travel times are associated with unusual anisotropy or isotropic heterogeneity. Finally, most diagnostic information on inner core anisotropy is obtained by the directional dependence of PKJKP travel times. However, observation of this phase is difficult and controversial (Okal & Cansi, 1998; Deuss et al., 2000) let alone variations with the direction of propagation.

There are other issues of inner core that are not addressed in this study. The possibility of the tilted axis of symmetry has been suggested by various researchers with the amount of tilt ranging from 5 to 10 degrees from the rotation axis (e.g., Shearer & Toy, 1991; Creager, 1992; Su &

Dziewoński, 1995; Song & Richards, 1996; McSweeney et al., 1997). Some of the studies rely heavily upon a limited number of paths (e.g., South Sandwich Islands to Alaska) to determine the location of the optimal axis of symmetry. A global analysis of absolute travel time data, such as the one presented for the inner-most inner core, combined with normal mode constraints, should provide a valuable contribution to this problem. Since travel time coverage at smaller epicentral distances is much better than that at nearly antipodal distances, more reliable results should be attainable.

Another observation with a significant consequence on the dynamics of the inner core is its super rotation. The eastward rotation was first reported using both differential (Song & Richards, 1996) and absolute (Su et al., 1996) travel times. This observation is consistent with theoretical calculations and simulations of the geomagnetic field which predict strong torque on the inner core due to electromagnetic coupling (e.g., Gubbins, 1981; Glatzmaier & Roberts, 1995b; Aurnou et al., 1996; Kuang & Bloxham, 1997). An alternative source of inner core super rotation is gravitational interaction between the inner core and the mantle, which can also produce results that are consistent with seismic observations (Buffett & Creager, 1999). The initial investigations of inner core rotation based upon travel times suggested rates of few degrees per year (Song & Richards, 1996; Su et al., 1996), but subsequent studies have reduced the rate to a value much less than one degree per year, between 0.05 to 0.6 degrees a year (Creager, 1997; Song, 2000). Temporal changes in splitting function of inner core modes have also been analysed for super rotation, giving a nearly zero rate (Sharrock & Woodhouse, 1998; Laske & Masters, 1999). These observations assume either tilted axis of symmetry or lateral variations within the inner core. A better constraint on super rotation may be obtained once these assumptions are verified. There is also a suggestion that the absolute travel time data can be separated into time dependent and stationary signals (Dziewoński, 2000) which should also be considered in future investigations.

Although it is more difficult to constrain than anisotropy of wave speed, knowledge of anelasticity, especially its radial dependence, provides additional information about the inner core. Attenuation within the inner core is stronger than other parts of the Earth (e.g., Sacks, 1969; Cormier, 1981; Widmer et al., 1991), and there are suggestions that it varies with frequency (e.g., Doornbos, 1983; Cummins & Johnson, 1988; Cormier et al., 1998). This frequency dependence of attenuation is controversial with some studies preferring frequency independence in the upper inner core (e.g., Bhattacharyya et al., 1993; Souriau & Roudil, 1995). The resolution of depth dependence of attenuation is also argued for (e.g., Souriau & Roudil, 1995) and against (e.g., Niazi & Johnson, 1992; Bhattacharyya et al., 1993). Anisotropy in attenuation has been suggested to exist based upon a mechanism for elastic anisotropy (Carcione & Cavallini, 1994). Due to uneven coverage and possible contaminations from sources outside the inner core, anisotropic anelasticity is difficult to resolve, but attempts have been made to observe this effect (Souriau & Romanowicz, 1996).

6.3 Inner-Most Inner Core

The inner-most inner core, introduced to explain the peculiar behaviour of absolute travel times from antipodal distances, is a small sphere of 300 km radius within the inner core. It constitutes less than 0.01% of the Earth's volume; its location and size make observations scarce. Because it is so small, finite frequency effects may become significant. Studies of ray sensitivity based upon Born approximation have shown that waves are insensitive to structure along its path, but sensitive to a broad region around it (e.g., Dahlen et al., 2000). The area of insensitivity, the Fresnel zone, is roughly the square root of the product of the wavelength and path length of the ray, and for the antipodal rays used to infer the inner-most inner core, the width of this zone is about 300 km. It is broad and should be considered in future studies, but it is not broad enough to hide the entire inner-most inner core. In addition, because of the constant anisotropy model fits to data between 165° and 173°, the main effect of the broad sensitivity kernel is to make the inner-most inner core much smaller than the current estimate.

The existence of the inner-most inner core with a distinct seismic behaviour poses many questions.

Material properties at such high pressures and temperatures are not well understood enough to determine whether the inner-most inner core can be explained by a phase change or if it requires change in composition. Furthermore, gravity in this region is nearly zero, which may affect the development of crystal structure. With so little information for guidance, one needs to speculate on the consequences, origin, and the role of the inner-most inner core in the evolution of the Earth. The distinct anisotropy may be a preserved region from the time when the Earth differentiated, and the tilt of the axis and the development of subsequent bulk inner core anisotropy may be due to a subsequent cataclysmic event. Alternatively, if inner core anisotropy is induced by the magnetic field generated in the outer core (e.g., Karato, 1993b; Buffett & Wenk, 2001), the change of anisotropy in the inner core signifies a major change in the dominant pattern of the magnetic field as inner core grew. These two scenarios require that the unique anisotropy of the inner-most inner core survive through the Earth's history. It would not be compatible with the theory of anisotropy developed by degree 1 convection within the inner core (e.g., Jeanloz & Wenk, 1988; Romanowicz et al., 1996), but the dynamics of the inner core is poorly known.

One useful and important key to unlocking the secrets of the inner-most inner core is its density. It is not an easily obtained parameter, but if enough measurements of the characteristic frequency of radial modes with high overtone number are made, it may be possible to resolve if the density changes from bulk to inner-most inner core. These modes possess sensitivity to the central 300 km of the core, and are convenient since their resonance peaks are not affected by the non-sphericity of the Earth. The complexities in the travel time table predicted from the inner-most inner core model suggest that high quality arrival time measurements will also provide valuable information on the properties of the inner-most inner core. To obtain such data, a densely spaced linear array in the 15° range of antipodal distance from a relatively active source region is required. With improvements in global coverage of seismometers and projects such as the USArray with its "flexible" component, or even a one-year deployment of broad band seismographs below the ocean bottom, it might be possible to conduct a more detailed survey of the distinct anisotropy that characterises the very center of the Earth.

6.4 Outer Core

Throughout the study, the outer core has been assumed to be seismologically homogeneous. There have been studies which argued for structure in the outer core (e.g., Ritzwoller et al., 1986; Widmer et al., 1992; Vasco & Johnson, 1998; Boschi & Dziewoński, 2000). Recent proposals of a sediment layer underneath the core-mantle boundary (Buffett et al., 2000) and possible isolation of light elements within the tangent cylinder (Hollerbach & Jones, 1995; Olson et al., 1999) have motivated some studies in which inner core sensitive data are modelled for outer core heterogeneity (Romanowicz & Bréger, 2000; Romanowicz et al., 2003). This is an important question that must be addressed in order to better model the inner core. The the investigation of the outer core is likely to benefit more by an analysis of data that are not sensitive to the inner core. Rather than forcing signals that might originate within the inner core into the outer core, data such as $\mathrm{PKP_{BC}}$, $\mathrm{PKP_{AB}}$, $\mathrm{PKP_{BC}}-\mathrm{PKP_{AB}}$, and splitting of mantle modes should be used to provide bounds on the strength of outer core heterogeneity.

6.5 Acknowledgements

The author would like to thank G. Masters for providing splitting coefficients of mantle modes, K. Creager for making differential travel time measurements easily accessible on the web, P. Shearer for ISC summary ray data used in Figure 4.8, W.-J. Su for processing the ISC data, and R. Pysklywec for models of convection simulation used to study the range of differential travel times due to mantle heterogeneity. Some data analyses were performed using programs provided by W.-J. Su, Y.J. Gu, and M. Antolik. Also, a few figures in this study were created using the Geomap software written by W.-J. Su, and GMT software (Wessel & Smith, 1991). Finally, I would like to thank A.M. Dziewoński, G. Ekström, H.-K. Mao, G. Masters, W.F. McDonough, J.X. Mitrovica, M. Nettles, R.J. O'Connell, S. Panasyuk, J. Ritsema, J. Tromp and H.J. van Heijst for discussions and suggestions.

References

Agnon, A., & Bukowinski, M.S.T., 1990. δ_S at high pressure and $d \ln V_s / d \ln V_p$ in the lower mantle. *Geophys. Res. Lett.* **17**, 1149–1152.

Anderson, D.L., 1987. A seismic equation of state II. Shear properties and thermodynamics of the lower mantle. *Phys. Earth Planet. Inter.* **45**, 307–323.

Anderson, O.L., & Isaak, D.G., 1995. Elastic constants of mantle minerals at high temperature. in *Mineral Physics & Crystallography: A Handbook of Physical Constants*, edited by T.J. Ahrens, pp. 64–97, American Geophysical Union, Washington DC.

Anderson, O.L., & Suzuki, I., 1983. Anharmonicity of three minerals at high temperature; forsterite, fayalite, and periclase. *J. Geophys. Res.* **88**, 3549–3556.

Anderson, O.L., Schreiber, E., Liebermann, R.C., & Soga, N., 1968. Some elastic constant data on minerals relevant to geophysics. *Rev. Geophys.* **6**, 491–524.

Anderson, O.L., Isaak, D.G., & Oda, H., 1991. Thermoelastic parameters for six minerals at high temperature. *J. Geophys. Res.* **96**, 18037–18046.

Antolik, M., Gu, Y.J., Ekström, G., & Dziewoński, A.M., 2003. J362D28: A new joint compressional and shear velocity model of the Earth's mantle. *Geophys. J. Int.*, in press.

Aurnou, J.M., Brito, D., & Olson, P.L., 1996. Mechanics of inner-core super-rotation. *Geophys. Res. Lett.* **23**, 3401–3404.

Backus, G.E., 1965. Possible forms of seismic anisotropy of the uppermost mantle under oceans. *J. Geophys. Res.* **70**, 3429–3439.

Backus, G., & Gilbert, F., 1968. The resolving power of gross Earth data. *Geophys. J. R. Astron. Soc.* **16**, 169–205.

Bergman, M.I., 1997. Measurements of elastic anisotropy due to solidification texturing and the implications for the Earth's inner core. *Nature* **389**, 60–63.

Bhattacharyya, J., Shearer, P., & Masters, G., 1993. Inner core attenuation from short-period PKP(BC) versus PKP(DF) waveforms. *Geophys. J. Int.* **114**, 1–11.

Bijwaard, H., Spakman, W., & Engdahl, E.R., 1998. Closing the gap between regional and global travel time tomography. *J. Geophys. Res.* **101**, 27791–27810.

Bokelmann, G.H.R., & Silver, P.G., 1993. The Caribbean anomaly; short-wavelength lateral heterogeneity in the lower mantle. *Geophys. Res. Lett.* **20**, 1131–1134.

Bolton, H., 1996. *Long Period Travel Times and the Structure of the Mantle.* Ph.D. Thesis, U.C. San Diego.

Boschi, L., & Dziewoński, A.M., 1999. "High" and "low" resolution images of the Earth's mantle: Implications of different approaches to tomographic modeling. *J. Geophys. Res.* **104**, 25567–25594.

Boschi, L., & Dziewoński, A.M., 2000. Whole Earth tomography from delay times of P, PcP, and

PKP phases: Lateral heterogeneities in the outer core or radial anisotropy in the mantle? *J. Geophys. Res.* **105**, 13675–13696.

Braginsky, S.I., 1963. Structure of the F layer and reasons for convection in the Earth's core. *Dokl. Akad. Nauk. SSSR* **149**, 1311–1314; trans. *Sov. Phys. Dokl.* **149**, 8–10.

Braginsky, S.I., & Roberts, P.H., 1995. Equations governing convection in Earth's core and the geodynamo. *Geophys. Astrophys. Fluid Dyn.* **79**, 1–97.

Bréger, L., & Romanowicz, B., 1998. Three-dimensional structure at the base of the mantle beneath the central Pacific. *Science* **282**, 718–720.

Bréger, L., Romanowicz, B., & Tkalčić, H., 1999. PKP(BC−DF) travel time residuals and short scale heterogeneity in the deep Earth. *Geophys. Res. Lett.* **26**, 3169–3172.

Bréger, L., Tkalčić, H., & Romanowicz, B., 2000. The effect of D" on PKP(AB−DF) travel time residuals and possible implications for inner core structure. *Earth Planet. Sci. Lett.* **175**, 133–143.

Buffett, B.A., 1997. Geodynamic estimates of the viscosity of the Earth's inner core. *Nature* **388**, 571–573.

Buffett, B.A., & Creager, K.C., 1999. A comparison of geodetic and seismic estimates of inner-core rotation. *Geophys. Res. Lett.* **26**, 1509–1512.

Buffett, B.A., & Wenk, H.R., 2001. Texturing of the Earth's inner core by Maxwell stresses. *Nature* **413**, 60–63.

Buffett, B.A., Garnero, E.J., & Jeanloz, R., 2000. Sediments at the top of Earth's core. *Science* **290**, 1338–1342.

Carcione, J.M., & Cavallini, F., 1994. A rheological model for anelastic anisotropic media with application to seismic wave propagation. *Geophys. J. Int.* **119**, 338–348.

Cazenave, A., Souriau, A., & Dominh, K., 1989. Global coupling of Earth surface topography with hotspots, geoid and mantle. *Nature* **340**, 54–57.

Chopelas, A., 1992. Sound velocities of MgO to very high compression. *Earth Planet. Sci. Lett.* **114**, 185–192.

Chopelas, A., & Boehler, R., 1989. Thermal expansion measurements at very high pressure, systematics, and a case for a chemically homogeneous mantle. *Geophys. Res. Lett.* **16**, 1347–1350.

Christensen, U., 1984. Instability of a hot boundary layer and initiation of thermo-chemical plumes. *Ann. Geophys.* **2**, 311–320.

Cormier, V.F., 1981. Short-period PKP phase and the anelastic mechanism of the inner core. *Phys. Earth Planet. Inter.* **24**, 291–301.

Cormier, V.F., & Choy, G.L., 1986. A search for lateral heterogeneity in the inner core from differential travel times near PKP-D and PKP-C. *Geophys. Res. Lett.* **13**, 1553–1556.

Cormier, V.F., Li, X., & Choy, G.L., 1998. Seismic attenuation of the inner core: Viscoelastic or stratigraphic? *Geophys. Res. Lett.* **25**, 4019–4022.

Corrieu, V., Ricard, Y., & Froidevaux, C., 1994. Converting mantle tomography into mass anomalies to predict the Earth's radial viscosity. *Phys. Earth Planet. Inter.* **84**, 3–13.

Crampin, S., 1977. A review of the effects of anisotropic layering on the propagation of seismic waves. *Geophys. J. R. Astron. Soc.* **49**, 9–27.

Creager, K.C., 1992. Anisotropy of the inner core from differential travel times of the phases PKP and PKIKP. *Nature*, **356**, 309-314.

Creager, K.C., 1997. Inner core rotation rate from small-scale heterogeneity and time-varying travel times. *Science* **278**, 1284–1288.

Creager, K.C., 1999. Large-scale variations in inner-core anisotropy. *J. Geophys. Res.* **104**, 23127–23139.

Creager, K.C., 2000. Inner core anisotropy and rotation. in *Earth's Deep Interior: Mineral Physics and Tomography From the Atomic to the Global Scale*, edited by S. Karato, A. Forte, R.C. Liebermann, G. Masters, and L. Stixrude, pp. 89–114, American Geophysical Union, Washington DC.

Cummins, P., & Johnson, L.R., 1988. Short-period body wave constraints on properties of the Earth's inner core boundary. *J. Geophys. Res.* **93**, 9058–9074.

Dahlen, F.A., & Tromp, J., 1998. *Theoretical Global Seismology.* Princeton University Press, Princeton, New Jersey.

Dahlen, F.A., Hung, S.H., & Nolet, G., 2000. Fréchet kernels for finite-frequency traveltimes; I, Theory. *Geophys. J. Int.* **141**, 157–174.

Davies, G.F., & Gurnis, M., 1986. Interaction of mantle dregs with convection: Lateral heterogeneity at the core-mantle boundary. *Geophys. Res. Lett.* **13**, 1517–1520.

de Boor, C., 1978. *A Practical Guide to Splines.* Springer Verlag, New York.

de Wijs, G.A., Kresse, G., Vocadlo, L., Dobson, D., Alfe, A., Gilan, M.J., & Price, G.D., 1998. The viscosity of liquid iron at the physical conditions of the Earth's core. *Nature* **392**, 805–807.

Deuss, A., & Woodhouse, J.H., 2001. Theoretical free-oscillation spectral; the importance of wide band coupling. *Geophys. J. Int.* **146**, 833–842.

Deuss, A., Woodhouse, J.H., Paulssen, H., & Trampert, J., 2000. The observation of inner core shear waves. *Geophys. J. Int.* **142**, 67–73.

Doornbos, D.J., 1983. Observable effects of the seismic absorption band in the Earth. *Geophys. J. R. Astron. Soc.* **75**, 693–711.

Doyle, H.A., & Hales, A.L., 1967. An analysis of the travel times of S waves to North American stations, in the distance range 28 degrees to 82 degrees. *Bull. Seismol. Soc. Am.* **57**, 761–771.

Durek, J.J., & Romanowicz, B., 1999. Inner core anisotropy inferred by direct inversion of normal mode spectra. *Geophys. J. Int.* **139**, 599–622.

Dziewoński, A.M., 1975. Resolution of large scale velocity anomalies in the mantle. *EOS Trans. Am. Geophys. Un. Suppl.* **56**, 395.

Dziewoński, A.M., 1984. Mapping the lower mantle: Determination of lateral heterogeneity in P velocity up to degree and order 6. *J. Geophys. Res.* **89**, 5929–5952.

Dziewoński, A.M., 2000. Global seismic tomography: Past, present and future. in *Problems in Geophysics for the New Millennium*, edited by E. Boschi, G. Ekström, and A. Morelli, pp. 289–349, Editrice Compositori, Bologna, Italy.

Dziewoński, A.M., & Anderson, D.L., 1981. Preliminary reference Earth model. *Phys. Earth Planet. Inter.* **25**, 297–356.

Dziewoński, A.M., & Gilbert, F., 1976. The effect of small, aspherical perturbations on travel times and a re-examination of the corrections for ellipticity. *Geophys. J. R. Astron. Soc.* **44**, 7–17.

Dziewoński, A.M., & Su, W.-J., 1998. A local anomaly in the inner core. *EOS Trans. Am. Geophys. Un. Suppl.* **79**, S218.

Dziewoński, A.M., & Woodhouse, J.H., 1987. Global images of the Earth's interior. *Science* **236**, 37–48.

Dziewoński, A.M., Hager, B.H., & O'Connell, R.J., 1977. Large scale heterogeneity in the lower mantle. *J. Geophys. Res.* **82**, 239–255.

Dziewoński, A.M., Ekström, G., & Salganik, M.P., 1994. Centroid-moment tensor solutions for

January - March 1993. *Phys. Earth Planet. Inter.* **82**, 9–17.

Dziewoński, A.M., Liu, X.-F. & Su, W.-J., 1997. Lateral heterogeneity in the lowermost mantle. in *Earth's Deep Interior*, edited by D. J. Crossley, pp. 11–50, Gordon and Breach, Newark, New Jersey.

Edmonds, A.R., 1960. *Angular Momentum in Quantum Mechanics.* Princeton Univ. Press, Princeton, New Jersey.

Ekström, G., & Dziewoński, A.M., 1998. The unique anisotropy of the Pacific upper mantle. *Nature* **394**, 168–172.

Engdahl, E.R., Flinn, E.A., & Romney, C.F., 1970. Seismic waves reflected from the Earth's inner core. *Nature* **228**, 852–853.

Engdahl, E.R., van der Hilst, R., & Buland, R., 1998. Global teleseismic earthquake relocation with improved travel times. *Bull. Seismol. Soc. Am.* **88**, 722–743.

Fearn, D.R., Loper, D.E., & Roberts, P.H., 1981. Structure of the Earth's inner core. *Nature* **292**, 232–233.

Flanagan, M.P., & Shearer, P.M., 1998. Global mapping of topography on transition zone velocity discontinuities by stacking *SS* precursors. *J. Geophys. Res.* **103**, 2673–2692.

Flanagan, M.P., & Shearer, P.M., 1999. A map of topography on the 410-km discontinuity from PP precursors. *Geophys. Res. Lett.* **26**, 549–552.

Forte, A.M., & Mitrovica, J.X., 2001. Deep-mantle high-viscosity flow and thermochemical structure inferred from seismic and geodynamic data. *Nature* **410**, 1049–1056.

Forte, A.M., & Peltier, W.R., 1987. Plate tectonics and aspherical earth structure: The importance of poloidal-toroidal coupling. *J. Geophys. Res.* **92**, 3645–3679.

Forte, A.M., & Woodward, R.L., 1997. Seismic-geodynamic constraints on three-dimensional structure, vertical flow, and heat transfer in the mantle. *J. Geophys. Res.* **102**, 17981–17994.

Forte, A.M., Woodward, R.L., & Dziewoński, A.M., 1994. Joint inversions of seismic and geodynamic data for models of three-dimensional mantle heterogeneity. *J. Geophys. Res.* **99**, 21857–21877.

Forte, A.M., Dziewoński A.M., & O'Connell, R.J., 1995a. Continent-ocean chemical heterogeneity in the mantle based on seismic tomography. *Science* **268**, 386–388.

Forte, A.M., Mitrovica, J.X., & Woodward, R.L., 1995b. Seismic-geodynamic determination of the origin of excess ellipticity of the core-mantle boundary. *Geophys. Res. Lett.* **22**, 1013–1016.

Gans, R.F., 1972. Viscosity of the Earth's core. *J. Geophys. Res.* **77**, 360–366.

Garcia, R., & Souriau, A., 2000. Inner core anisotropy and heterogeneity level. *Geophys. Res. Lett.* **27**, 3121–3124.

Garnero, E.J., & Helmberger, D.V., 1996. Seismic detection of a thin laterally varying boundary layer at the base of the mantle beneath the central-Pacific. *Geophys. Res. Lett.* **23**, 977–980.

Garnero, E.J., Revenaugh, J., Williams, Q., Lay, T., & Kellogg, L.H., 1998. Ultralow velocity zone at the core-mantle boundary. in *The Core-Mantle Boundary Region*, edited by M. Gurnis, M.E. Wysession, E. Knittle, and B.A. Buffett, pp. 319–334, American Geophysical Union, Washington DC.

Giardini, D., Li, X.-D., & Woodhouse, J.H., 1987. Three-dimensional structure of the Earth from splitting in free-oscillation spectra. *Nature* **325**, 405–411.

Giardini, D., Li, X.-D., & Woodhouse, J.H., 1988. Splitting functions of long-period normal modes of the Earth. *J. Geophys. Res.* **93**, 13716–13742.

Glatzmaier, G.A., & Roberts, P.H., 1995a. A three-dimensional self-consistent computer simulation of a geomagnetic reversal. *Nature* **377**, 203–209.

Glatzmaier, G.A., & Roberts, P.H., 1995b. A three-dimensional convective dynamo solution with rotation and finitely conducting inner core and mantle. *Phys. Earth Planet. Inter.* **91**, 63–75.

Grand, S.P., van der Hilst, R.D., & Widiyantoro, S., 1997. Global seismic tomography; a snapshot of convection in the Earth. *GSA Today* **7**, 1–7.

Gu, Y., Dziewoński, A.M., & Agee, C.B., 1998. Global de-correlation of the topography of transition zone discontinuities. *Earth Planet. Sci. Lett.* **157**, 57–67.

Gu, Y.J., Dziewoński, A.M., Su, W.-J., & Ekström, G., 2001. Models of the mantle shear velocity and discontinuities in the pattern of lateral heterogeneities. *J. Geophys. Res.* **106**, 11169–11199.

Gubbins, D., 1977. Energetics of the Earth's core. *Geophys. J.* **43**, 453–464.

Gubbins, D., 1981. Rotation of the inner core. *J. Geophys. Res.* **86**, 11695–11699.

Gurnis, M., 1990. Bounds on global dynamic topography from Phanerozoic flooding of continental platforms. *Nature* **344**, 754–756.

Gwinn, C.R., Herring, T.A., & Shapiro, I.I., 1986. Geodesy by radio interferometry: Studies of the forced nutations of the Earth 2. Interpretation. *J. Geophys. Res.* **91**, 4755–4765.

Hager, B.H., & Clayton, R.W., 1989. Constraints on the structure of mantle convection using seismic observations, flow models, and the geoid. in *Mantle Convection: Plate Tectonics and Global Dynamics*, edited by W.R. Peltier, pp. 657–763, Gordon and Breach, Newark, New Jersey.

Hager, B.H., Clayton, R.W., Richards, M.A., Comer, R.P., & Dziewoński, A.M., 1985. Lower mantle heterogeneity, dynamic topography and the geoid. *Nature* **313**, 541–545.

Hales, A.L., & Roberts, J.L., 1970. The travel times of S and SKS. *Bull. Seismol. Soc. Am.* **60**, 461–489.

Hansen, U., & Yuen, D.A., 1988. Numerical simulations of thermal-chemical instabilities at the core-mantle boundary. *Nature* **334**, 237–240.

He, X.,& Tromp, J., 1996. Normal-mode constraints on the structure of the Earth. *J. Geophys. Res.* **101**, 20053–20082.

Helffrich, G., & Sacks, S., 1994. Scatter and bias in differential PKP travel times and implications for mantle and core phenomena. *Geophys. Res. Lett.* **21**, 2167–2170.

Hollerbach, R., & Jones, C.A., 1993. Influence of the Earth's inner core on geomagnetic fluctuations and reversals. *Nature* **365**, 541–543.

Hollerbach, R., & Jones, C.A., 1995. On the magnetically stabilizing role of the Earth's inner core. *Phys. Earth Planet. Inter.* **87**, 171–181.

Huber, P.J., 1981. *Robust Statistics.* Wiley, New York.

Inoue, H., Fukao, Y., Tanabe, K., & Ogata, Y., 1990. Whole mantle P-wave travel time tomography. *Phys. Earth Planet. Inter.* **59**, 294–328.

Isaak, D.G., 1992. High-temperature elasticity of iron-bearing olivines. *J. Geophys. Res.* **97**, 1871–1885.

Isaak, D.G., Anderson, O.L., & Goto, T., 1989. Elasticity of single-crystal forsterite measured to 1700 K. *J. Geophys. Res.* **94**, 5895–5906.

Isaak, D.G., Anderson, O.L., & Cohen, R.E., 1992. The relationship between shear and compressional velocities at high pressures: Reconciliation of seismic tomography and mineral physics. *Geophys. Res. Lett.* **19**, 741–744.

Ishii, M., & Dziewoński, A.M., 2002. The innermost inner core of the earth: Evidence for a change in anisotropic behavior at the radius of about 300 km. *Proc. Natl. Acad. Sci. USA* **22**, 14026–14030.

Ishii, M., & Tromp, J., 1999. Normal-mode and free-air gravity constraints on lateral variations in velocity and density of the Earth's mantle. *Science* **285**, 1231–1236.

Ishii, M., & Tromp, J., 2001. Even-degree lateral variations in the mantle constrained by free oscillations and the free-air gravity anomaly. *Geophys. J. Int.* **145**, 77–96.

Ishii, M., Tromp, J., Dziewoński, A.M., & Ekström, G., 2002a. Joint inversion of normal mode and body wave data for inner core anisotropy: 1. Laterally homogeneous anisotropy. *J. Geophys. Res.* **107**, 10.1029/2001JB000712.

Ishii, M., Dziewoński, A.M., Tromp, J., & Ekström, G., 2002b. Joint inversion of normal mode and body wave data for inner core anisotropy: 2. Possible complexities. *J. Geophys. Res.* **107**, 10.1029/2001JB000713.

Ito, E., Morooka, K., & Ujike, O., 1993. Dissolution of K in molten iron at high pressure and temperature. *Geophys. Res. Lett.* **20**, 1651–1654.

Jackson, I., 1998. Elasticity, composition and temperature of the Earth's lower mantle. *Geophys. J. Int.* **134**, 291–311.

Jacobs, J.A., 1953. The earth's inner core. *Nature* **172**, 297–298.

Jeanloz, R., & Knittle, E.B., 1989. Density and composition of the lower mantle. *Phil. Trans. R. Soc. London Ser. A* **328**, 377–389.

Jeanloz, R., & Wenk, H.R., 1988. Convection and anisotropy of the inner core. *Geophys. Res. Lett.* **15**, 72–75.

Jeffreys, H., & Singh, K., 1973. Comparison of station errors in seismology. *Geophys. J. R. Astron. Soc.* **32**, 423–437.

Jordan, T.H., 1978. Composition and development of the continental tectosphere. *Nature* **274**, 544–548.

Jordan, T.H., & Lynn, W.S., 1974. A velocity anomaly in the lower mantle. *J. Geophys. Res.* **79**, 2679–2685.

Julian, B.R., & Sengupta, M.K., 1973. Seismic travel time evidence for lateral inhomogeneity in deep mantle. *Nature* **242**, 443–447.

Kárason, H., & van der Hilst, R.D., 2001. Tomographic imaging of the lowermost mantle with differential times of refracted and diffracted core phases (PKP, P_{diff}). *J. Geophys. Res.* **106**, 6569–6587.

Karato, S., 1993a. Importance of anelasticity in the interpretation of seismic tomography. *Geophys. Res. Lett.* **20**, 1623–1626.

Karato, S., 1993b. Inner core anisotropy due to the magnetic field-induced preferred orientation of iron. *Science* **262**, 1708–1711.

Karato, S., 1999. Seismic anisotropy of the earth's inner core resulting from flow induced by Maxwell stresses. *Nature* **402**, 871–873.

Karato, S., & Karki, B.B., 2001. Origin of lateral variation of seismic wave velocities and density in the deep mantle. *J. Geophys. Res.* **106**, 21771–21783.

Kawakatsu, H., & Niu, F., 1994. Seismic evidence for a 920-km discontinuity in the mantle. *Nature* **371**, 301–305.

Kendall, J-M., 2000. Seismic anisotropy in the boundary layers of the mantle. in *Earth's Deep Interior: Mineral Physics and Tomography From the Atomic to the Global Scale*, edited by S. Karato, A. Forte, R.C. Liebermann, G. Masters, and L. Stixrude, pp. 133–159, American Geophysical Union, Washington DC.

Kennett, B.L.N., Widiyantoro, S., & van der Hilst, R.D., 1998. Joint seismic tomography for bulk sound and shear wave speed in the Earth's mantle. *J. Geophys. Res.* **103**, 12469–12493.

Knittle, E., & Jeanloz, R., 1991. Earth's core-mantle boundary: Results of experiments at high pressures and temperatures. *Science* **251**, 1438–1443.

Kuang, W., & Bloxham, J., 1997. An Earth-like numerical dynamo model. *Nature* **389**, 371–374.

Kuo, C., & Romanowicz, B., 2002. On the resolution of density anomalies in the Earth's mantle using spectral fitting of normal mode data. *Geophys. J. Int.* **150**, 162–179.

Lancaster, P., & Salkauskas, K., 1990. *Curve and Surface Fitting.* Academic Press Inc., San Diego.

Laske, G., & Masters, G., 1999. Limits on differential rotation of the inner core from an analysis of the Earth's free oscillations. *Nature* **402**, 66–69.

Lay, T., 1983. Localized velocity anomalies in the lower mantle. *Geophys. J. R. Astron. Soc.* **72**, 483–516.

Lay, T., Williams, Q., Garnero, E.J., Kellogg, L., & Wysession, M.E., 1998. Seismic wave anisotropy in the D" region and its implications. in *The Core-Mantle Boundary Region*, edited by M. Gurnis, M.E. Wysession, E. Knittle, and B.A. Buffett, pp. 299–318, American Geophysical Union, Washington DC.

Lehmann, I., 1936. P'. *Publ. Bur. Cent. Seismol. Int. Trav. Sci. A* **14**, 87–115.

Lemoine, F.G., Smith, D.E., Kunz, L., Smith, R., Pavlis, N.K., Klosko, S.M., Chinn, D.S., Torrence, M.H., Williamson, R.G., Cox, C.M., Rachlin, K.E., Wang, Y.M., Kenyon, S.C., Salman, R., Trimmer, R., Rapp, R.H., & Nerem, R.S., 1997. The development of the NASA GSFC and NIMA joint geopotential model. In *International Association of Geodesy Symposia* **117**, pp. 462–469, edited by J. Segawa, H. Fujimoto, and S. Okubo, Springer-Verlag, Berlin.

Lemoine, F.G., Pavlis, N.K., Kenyon, S.C., Rapp, R.H., Pavlis, E.C., & Chao, B.F., 1998a. New high-resolution model developed for Earth's gravitational field. *EOS Trans. AGU* **79**, 117–118.

Lemoine, F.G., Kenyon, S.C., Factor, J.K., Trimmer, R.G., Pavlis, N.K., Chinn, D.S., Cox, C.M., Klosko, S.M., Luthcke, S.B., Torrence, M.H., Wang, Y.M., Williamson, R.G., Rapp, R.H., & Olson, T.R., 1998b. The development of the joint NASA GSFC and National Imagery and Mapping Agency (NIMA) geopotential model, EGM96. NASA/TP-1998–206861.

Li, X.-D., & Romanowicz, B., 1996. Global mantle shear-velocity model developed using nonlinear asymptotic coupling theory. *J. Geophys. Res.* **101**, 22245–22272.

Li, X.-D., Giardini, D., & Woodhouse, J.H., 1991a. Large-scale three-dimensional even-degree structure of the Earth from splitting of long-period normal modes. *J. Geophys. Res.* **96**, 551–577.

Li, X.-D., Giardini, D., & Woodhouse, J.H., 1991b. The relative amplitudes of mantle heterogeneity in P velocity, S velocity and density from free-oscillation data. *Geophys. J. Int.* **105**, 649–657.

Lister, J.R., & Buffett, B.A., 1995. The strength and efficiency of thermal and compositional convection in the geodynamo. *Phys. Earth Planet. Inter.* **91**, 17–30.

Lithgow-Bertelloni, C., & Richards, M.A., 1998. The dynamics of Cenozoic and Mesozoic plate motions. *Rev. Geophys.* **36**, 27–78.

Liu, X.-F., & Dziewoński, A.M., 1998. Global analysis of shear wave velocity anomalies in the lowermost mantle. in *The Core-Mantle Boundary Region*, edited by M. Gurnis, M.E. Wysession, E. Knittle, and B.A. Buffett, pp. 21–36, American Geophysical Union, Washington DC.

Liu, X.-F., Tromp, J., & Dziewoński, A.M., 1998. Is there a first-order discontinuity in the lowermost mantle? *Earth Planet. Sci. Lett.* **160**, 343–351.

Loper, D.E., & Roberts, P.H., 1978. On the motion of an iron-alloy core containing a slurry, I, General theory. *Geophys. Astrophys. Fluid Dyn.* **9**, 289–321.

Love, A.E.H., 1927. *A Treatise on the Theory of Elasticity*, 4th edition, Cambridge University Press, Cambridge.

Mao, H.-k., Shu, J., Shen, G., Hemley, R.J., Li, B., & Singh, A.K., 1998. Elasticity and rheology of iron above 220 GPa and the nature of the Earth's inner core. *Nature* **396**, 741–743.

Masters, G., & Gilbert, F., 1981. Structure of the inner core inferred from observations of its spheroidal shear modes. *Geophys. Res. Lett.* **8**, 569–571.

Masters, G., Johnson, S., Laske, G., & Bolton, H., 1996. A shear-velocity model of the mantle. *Phil. Trans. R. Soc. Lond. A* **354**, 1385–1411.

Masters, G., Laske, G., & Gilbert, F., 2000a. Autoregressive estimation of the splitting matrix of free-oscillation multiplets. *Geophys. J. Int.* **141**, 25–42.

Masters, G., Laske, G., & Gilbert, F., 2000b. Matrix autoregressive analysis of free-oscillation coupling and splitting. *Geophys. J. Int.* **143**, 478–489.

Masters, G., Laske, G., Bolton, H., & Dziewoński, A.M., 2000c. The relative behavior of shear velocity, bulk sound speed, and compressional velocity in the mantle: Implications for chemical and thermal structure. in *Earth's Deep Interior: Mineral Physics and Tomography From the Atomic to the Global Scale*, edited by S. Karato, A.M. Forte, R.C. Liebermann, G. Masters, and L. Stixrude, pp. 63–87, American Geophysical Union, Washington DC.

Matyska, C., & Yuen, D.A., 2002. Bullen's parameter η: A link between seismology and geodynamical modeling. *Earth Planet. Sci. Lett.* **198**, 471–483.

McNamara, A.K., Karato, S., & van Keken, P.E., 2001. Localization of dislocation creep in the lower mantle; implications for the origin of seismic anisotropy. *Earth Planet. Sci. Lett.* **191**, 85–99.

McSweeney, T.J., 1995. *Seismic Constraints on Core Structure and Dynamics.* Ph.D. Thesis, University of Washington, Seattle, WA.

McSweeney, T.J., Creager, K.C., & Merrill, R.T., 1997. Depth extent of inner-core seismic anisotropy and implications for geomagnetism. *Phys. Earth Planet. Int.* **101**, 131–156.

Mégnin, C., & Romanowicz, B., 2000. The 3D shear velocity structure of the mantle from the inversion of body, surface, and higher-mode waveforms. *Geophys. J. Int.* **143**, 709–728.

Menke, W., 1989. *Geophysical Data Analysis: Discrete Inverse Theory.* Academic Press, Inc., San Diego.

Mooney, W.D., Laske, G., & Masters, T.G., 1998. Crust 5.1: A global crustal model at 5° × 5°. *J. Geophys. Res.* **103**, 727–747.

Morelli, A., & Dziewoński, A.M., 1987. Topography of the core-mantle boundary and lateral homogeneity of the liquid core. *Nature* **325**, 678–683.

Morelli, A., Dziewoński, A.M., & Woodhouse, J.H., 1986. Anisotropy of the inner core inferred from *PKIKP* travel times. *Geophys. Res. Lett.* **13**, 1545–1548.

Mori, J., & Helmberger, D.V., 1995. Localized boundary layer below the mid-Pacific velocity anomaly identified from a *PcP* precursor. *J. Geophys. Res.* **100**, 20359–20365.

Moser, T.J., Nolet, G., & Snieder, R., 1992. Ray bending revisited. *Bull. Seismol. Soc. Am.* **82**, 259–288.

Nakiboglu, S.M., 1982. Hydrostatic theory of the Earth and its mechanical implications. *Phys. Earth Planet. Inter.* **28**, 302–311.

Nataf, H.C., Nakanishi, I., & Anderson, D.L., 1986. Measurements of mantle wave velocities and inversion for lateral heterogeneities and anisotropy, Part III: Inversion. *J. Geophys. Res.* **91**, 7261–7307.

Ni, S., Tan, E., Gurnis, M., & Helmberger, D.V., 2002. Sharp sides to the African Superplume. *Science* **296**, 1850–1852.

Niazi, M., & Johnson, L.R., 1992. Q in the inner core. *Phys. Earth Planet. Inter.* **74**, 55–62.

Niu, F., & Wen, L., 2001. Hemispherical variations in seismic velocity at the top of the Earth's inner core. *Nature* **410**, 1081–1084.

Okal, E.A., & Cansi, Y., 1998. Detection of PKJKP at intermediate periods by progressive multichannel correlation. *Earth Planet. Sci. Lett.* **164**, 23–30.

Olson, P., Christensen, U., & Glatzmaier, G., 1999. Numerical modeling of the geodynamo: Mechanisms of field generation and equilibration. *J. Geophys. Res.* **104**, 10383–10404.

Ouzounis, A., & Creager, K.C., 2001. Radial transition from isotropy to strong anisotropy in the upper inner core. *EOS Trans. Am. Geophys. Un. Suppl.* **82**, F943.

Parker, L.J., Atou, T., & Badding. J.V., 1996. Transition element-like chemistry for Potassium under pressure. *Science* **273**, 95–97.

Poirier, J.-P., 1988. Transport properties of liquid metals and viscosity of the Earth's core. *Geophys. J. R. Astron. Soc.* **92**, 99–105.

Poupinet, G., Pillet, R., & Souriau, A., 1983. Possible heterogeneity of the Earth's core deduced from PKIKP travel times. *Nature* **305**, 204–206.

Press, W.H., Teukolsky, S.A., Vetterling, W.T., & Flannery, B.P., 1992. *Numerical Recipes in Fortran 77*, 2nd edition, Cambridge University Press, New York.

Pulliam, R.J., Vasco, D.W., & Johnson, L.R., 1993. Tomographic inversions for mantle P wave velocity structure based on the minimization of ℓ_2 and ℓ_1 norms of International Seismological Center travel time residuals. *J. Geophys. Res.* **98**, 699–734.

Pulver, S., & Masters, G., 1990. PcP-P travel times and the ratio of P to S velocity variations in the lower mantle. *EOS Trans. Am. Geophys. Un. Suppl.* **71**, 1465.

Pysklywec, R.N., & Mitrovica, J.X., 2000. Mantle flow mechanisms of epeirogeny and their possible role in the evolution of the Western Canada Sedimentary Basin. *Can. J. Earth Sci.* **37**, 1535–1548.

Reid, F.J.L., Woodhouse, J.H., & van Heijst, H.J., 2001. Upper mantle attenuation and velocity structure from measurements of differential S phases. *Geophys. J. Int.* **145**, 615–630.

Resovsky, J.S., & Ritzwoller, M.H., 1995. Constraining odd-degree Earth structure with coupled free-oscillations. *Geophys. Res. Lett.* **22**, 2301–2304.

Resovsky, J.S., & Ritzwoller, M.H., 1998. New constraints on deep Earth structure from generalized spectral fitting: Application to free oscillations below 3 mHz. *J. Geophys. Res.* **103**, 783–810.

Resovsky, J.S., & Ritzwoller, M.H., 1999a. A degree 8 mantle shear velocity model from normal mode observations below 3mHz. *J. Geophys. Res.* **104**, 993–1014.

Resovsky, J.S., & Ritzwoller, M.H., 1999b. Regularization uncertainty in density models estimated from normal mode data. *Geophys. Res. Lett.* **26**, 2319–2322.

Reynard, B., & Price, G.D., 1990. Thermal expansion of mantle minerals at high pressures; a theoretical study. *Geophys. Res. Lett.* **17**, 689–692.

Rial, J.A., & Cormier, V.F., 1980. Seismic waves at the epicenter's antipodes. *J. Geophys. Res.* **85**, 2661–2668.

Ricard, Y., Richards, M., Lithgow-Bertelloni, C., & Le Stunff, Y., 1993. A geodynamic model of mantle density heterogeneity. *J. Geophys. Res.* **98**, 21895–21909.

Ritsema, J., Ni, S., Helmberger, D.V., & Crotwell, H.P., 1998. Evidence for strong shear velocity reductions and velocity gradients in the lower mantle beneath Africa. *Geophys. Res. Lett.* **25**, 4245–4248.

Ritsema, J., van Heijst, H.-J., & Woodhouse, J.H., 1999. Complex shear wave velocity structure imaged beneath Africa and Iceland. *Science* **286**, 1925–1928.

Ritzwoller, M.H., & Lavely, E.M., 1995. Three-dimensional seismic models of the Earth's mantle. *Rev. Geophys.* **33**, 1–66.

Ritzwoller, M.H., & Resovsky, J.S., 1995. The feasibility of normal mode constraints on higher degree structures. *Geophys. Res. Lett.* **22**, 2305–2308.

Ritzwoller, M.H., Masters, G., & Gilbert, F., 1986. Observation of anomalous splitting and their interpretation in terms of aspherical structure. *J. Geophys. Res.* **91**, 10203–10228.

Ritzwoller, M.H., Masters, G., & Gilbert, F., 1988. Constraining aspherical structure with low-degree interaction coefficients: Application to uncoupled multiplets. *J. Geophys. Res.* **93**, 6369–6396.

Robertson, G.S. & Woodhouse, J.H., 1995. Evidence for proportionality of P and S heterogeneity in the lower mantle. *Geophys. J. Int.* **123**, 85–116.

Robertson, G.S., & Woodhouse, J.H., 1996. Ratio of relative S to P velocity heterogeneity in the lower mantle. *J. Geophys. Res.* **101**, 20041–20052.

Romanowicz, B., 2001. Can we resolve 3D density heterogeneity in the lower mantle? *Geophys. Res. Lett.* **28**, 1107–1110.

Romanowicz, B., & Bréger, L., 2000. Anomalous splitting of free oscillations: A reevaluation of possible interpretations. *J. Geophys. Res.* **105**, 21559–21578.

Romanowicz, B.A., & Cara, M., 1980. Reconsideration of the relations between S and P station anomalies in North America. *Geophys. Res. Lett.* **7**, 417–420.

Romanowicz, B.A., & Gung, Y., 2002. Superplumes from the core-mantle boundary to the lithosphere; implications for heat flux. *Science* **296**, 513–516.

Romanowicz, B., Li, X.-D., & Durek, J., 1996 Anisotropy in the inner core: Could it be due to low order convection? *Science* **274**, 963–966.

Romanowicz, B., Tkalčić, H., & Bréger, L., 2003. On the origin of complexity in PKP travel time data. in *Earth's Core: Dynamics, Structure, Rotation*, edited by V. Dehant, K.C. Creager, S. Karato, and S. Zatman, pp. 31–44, American Geophysical Union, Washington DC.

Roudil, P., & Souriau, A., 1993. Liquid core structure and PKP station anomalies derived from PKP(BC) propagation times. *Phys. Earth Planet. Inter.* **77**, 225–236.

Sacks, I.S., 1969. Anelasticity of the inner core. *Carnegie Institution Year Book* **69**, 416–419.

Sharrock, D.S., & Woodhouse, J.H., 1998. Investigation of time dependent inner core structure by analysis of free oscillation spectra. *Earth Planet. Space* **50**, 1013–1018.

Shearer, P.M., 1994. Constraints on inner core anisotropy from PKP(DF) travel times. *J. Geophys. Res.* **99**, 19647–19659.

Shearer, P.M., & Toy, K.M., 1991. *PKP(BC)* versus *PKP(DF)* differential travel times and aspherical structure in the Earth's inner core. *J. Geophys. Res.* **96**, 2233–2247.

Shearer, P.M., Toy, K.M., & Orcutt, J.A., 1988. Axi-symmetric Earth models and inner-core anisotropy. *Nature* **333**, 228–232.

Song, X., 1996. Anisotropy in the central part of the inner core. *J. Geophys. Res.* **101**, 16089–16097.

Song, X., 1997. Anisotropy of the Earth's inner core. *Rev. Geophys.* **35**, 297—313.

Song, X., 2000. Joint inversion for inner core rotation, inner core anisotropy, and mantle heterogeneity. *J. Geophys. Res.* **105**, 7931–7943.

Song, X.-D., & Helmberger, D.V., 1993. Anisotropy of Earth's inner core. *Geophys. Res. Lett.* **20**, 2591–2594.

Song, X., & Helmberger, D.V., 1995. Depth dependence of anisotropy of Earth's inner core. *J. Geophys. Res.* **100**, 9805–9816.

Song, X.-D., & Helmberger, D.V., 1997. PKP differential travel times: Implications for 3-D lower mantle. *Geophys. Res. Lett.* **24**, 1863–1866.

Song, X., & Helmberger, D.V., 1998. Seismic evidence for an inner core transition zone. *Science* **282**, 924–9271.

Song, X., & Richards, P.G., 1996. Seismological evidence for differential rotation of the Earth's inner core. *Nature 382*, 221–224.

Song, X., & Xu, X., 2002. Inner core transition zone and anomalous PKP(DF) waveforms from polar paths. *Geophys. Res. Lett.* **29**, 10.1029/2001GL013822.

Souriau, A., & Poupinet, G., 2000. Inner core rotation: A test at the worldwide scale. *Phys. Earth Planet. Int.* **118**, 13–27.

Souriau, A., & Romanowicz, B., 1996. Anisotropy in the inner core attenuation: A new type of data to constrain the nature of the solid core. *Geophys. Res. Lett.* **23**, 1–4.

Souriau, A., & Roudil, P., 1995. Attenuation in the upper most inner core from broadband Geoscope PKP data. *Geophys. J. Int.* **123**, 572–587.

Souriau, A., & Souriau, M., 1989. Ellipticity and density at the inner core boundary from subcritical $PKiKP$ and PcP data. *Geophys. J. Int.* **98**, 39–54.

Souriau, A., & Woodhouse, J.H., 1985. A worldwide comparison of predicted S-wave delays from a three-dimensional upper mantle model with P-wave station corrections. *Phys. Earth Planet. Inter.* **39**, 75–88.

Souriau, A., Roudil, P., & Moynot, B., 1997. Inner core differential rotation: Facts and artefacts. *Geophys. Res. Lett.* **24**, 2103–2106.

Steinle-Neumann, G., Stixrude, L., Cohen, R.E., & Gulseren, O., 2001. Elasticity of iron at the temperature of the Earth's inner core. *Nature* **413**, 57–60.

Stevenson, D.J., 1987. Limits on lateral density and velocity variations in the Earth's outer core. *Geophys. J. R. Astron. Soc.* **88**, 311–319.

Stevenson, D.J., 1996. Inner core anisotropy. *EOS Trans. Am. Geophys. Un. Suppl.* **77**, F41.

Stixrude, L., & Cohen, R.E., 1995. High-pressure elasticity of iron and anisotropy of Earth's inner core. *Science* **267**, 1972–1975.

Su, W.-J., 1992. *The Three-Dimensional Shear-Wave Velocity Structure of the Earth's Mantle.* Ph.D. Thesis, Harvard University, Cambridge, MA.

Su, W.-J., & Dziewoński, A.M., 1993. Joint 3-D inversion for P and S velocity in the mantle. *EOS Trans. AGU* **74**, Fall Meeting Suppl., 557.

Su, W.-J., & Dziewoński, A.M., 1995. Inner core anisotropy in three dimensions. *J. Geophys. Res.* **100**, 9831–9852.

Su, W.-J., & Dziewoński, A.M., 1997. Simultaneous inversion for 3-D variations in shear and bulk velocity in the mantle. *Phys. Earth Planet. Inter.* **100**, 135–156.

Su, W.-J., Woodward, R.L., & Dziewoński, A.M., 1994. Degree-12 model of shear-velocity heterogeneity in the mantle. *J. Geophys. Res.* **99**, 6945–6980.

Su, W.-J., Dziewoński, A.M., & Jeanloz, R., 1996. Planet within a planet: Rotation of the inner core of Earth. *Science* **274**, 1883–1887.

Sylvander, M., Ponce, B., & Souriau, A., 1997. Seismic velocities at the core-mantle boundary inferred from P waves diffracted around the core. *Phys. Earth Planet. Inter.* **101**, 189–202.

Tackley, P.J., 1998. Three-dimensional simulations of mantle convection with a thermo-chemical basal boundary layer: D"? in *The Core-Mantle Boundary Region*, edited by M. Gurnis, M.E. Wysession, E. Knittle, and B.A. Buffett, pp. 231–253, American Geophysical Union, Washington

DC.

Tanaka, S., & Hamaguchi, H., 1997. Degree one heterogeneity and hemispherical variation of anisotropy in the inner core from PKP(BC) and PKP(DF) times. *J. Geophys. Res.* **102**, 2925–2938.

Tanimoto, T., 1991. Waveform inversion for three-dimensional density and S wave structure. *J. Geophys. Res.* **96**, 8167–8189.

Taylor, J.R., 1997. *An Introduction to Error Analysis: The Study of Uncertainties in Physical Measurements.* 2nd edition, University Science Books, Sausalito, California.

Tkalčić, H., Romanowicz, B., & Houy, N., 2002. Constraints on D" structure using PKP(AB−DF), PKP(BC−DF) and PcP−P travel time data from broadband records. *Geophys. J. Int.* **148**, 599–616.

Tromp, J., 1993. Support for anisotropy of the Earth's inner core from free oscillations. *Nature* **366**, 678–681.

Tromp, J., 1995a. Normal-mode splitting observations from the Great 1994 Bolivia and Kuril Islands earthquakes: Constraints on the structure of the mantle and inner core. *GSA Today* **5**, 137–151.

Tromp, J., 1995b. Normal-mode splitting due to inner-core anisotropy. *Geophys. J. Int.* **121**, 963–968.

Tromp, J., & Zanzerkia, E., 1995. Toroidal splitting observations from the great 1994 Bolivia and Kuril Islands earthquakes. *Geophys. Res. Lett.* **22**, 2297–2300.

Turcotte, D.L., & Schubert, G., 1982. *Geodynamics: Applications of Continuum Physics to Geological Problems.* John Wiley & Sons, Inc., New York.

van der Hilst, R.D., & Kárason, H., 1999. Composition heterogeneity in the bottom 1000 kilometers of Earth's mantle; toward a hybrid convection model. *Science* **283**, 1885–1888.

van der Hilst, R.D., Widiyantoro, S., & Engdahl, E.R., 1997. Evidence for deep mantle circulation from global tomography. *Nature* **386**, 578–584.

van der Hilst, R.D., Widiyantoro, S., Creager, K.C., & Sweeney, T.J., 1998. Deep subduction and aspherical variations in P-wavespeed at the base of Earth's mantle. in *The Core-Mantle Boundary Region*, edited by M. Gurnis, M.E. Wysession, E. Knittle, and B.A. Buffett, pp. 5–20, American Geophysical Union, Washington DC.

Vasco, D.W., & Johnson, L.R., 1998. Whole Earth structure estimated from seismic arrival times. *J. Geophys. Res.* **103**, 2633–2671.

Vasco, D.W., Johnson, L.R., Pulliam, R.J., & Earle, P.S., 1994. Robust inversion of IASP91 travel time residuals for mantle P and S velocity structure, earthquake mislocations, and station corrections. *J. Geophys. Res.* **99**, 13727–13755.

Vidale, J.E., & Hedlin, M.A.H., 1998. Intense scattering at the core-mantle boundary north of Tonga: Evidence for partial melt. *Nature* **391**, 682–685.

Vinnik, L., Romanowicz, B., & Bréger, L., 1994. Anisotropy in the center of the inner core. *Geophys. Res. Lett.* **21**, 1671–1674.

Wang, Z., & Dahlen, F.A., 1995. Spherical-spline parameterization of three-dimensional Earth models. *Geophys. Res. Lett.* **22**, 3099–3102.

Wen, L., & Anderson, D.L., 1997. Layered mantle convection: A model for geoid and topography. *Earth Planet. Sci. Lett.* **146**, 367–377.

Wessel, P., & Smith, W.H.F., 1991. Free software helps map and display data. *EOS Trans. Am. Geophys. Un.* **72**, 441.

Wickens, A.J., & Buchbinder, G.G.R., 1980. S-wave residuals in Canada. *Bull. Seismol. Soc. Am.*

70, 809–822.

Widmer, R., Maters, G., & Gilbert, F., 1991. Spherically symmetric attenuation within the Earth from normal mode data. *Geophys. J. Int.* **104**, 541–553.

Widmer, R., Masters, G., & Gilbert, F., 1992. Observably split multiplets - data analysis and interpretation in terms of large-scale aspherical structure. *Geophys. J. Int.* **111**, 559–576.

Woodhouse, J.H., 1980. The coupling and attenuation of nearly resonant multiplets in the Earth's free oscillation spectrum. *Geophys. J. R. Astron. Soc.* **61**, 261–283.

Woodhouse, J.H., & Dziewoński, A.M., 1984. Mapping the upper mantle: Three-dimensional modeling of Earth structure by inversion of seismic waveforms. *J. Geophys. Res.* **89**, 5953–5986.

Woodhouse, J.H., & Dahlen, F.A., 1978. The effect of a general aspherical perturbation on the free oscillations of the Earth. *Geophys. J. R. Astron. Soc.* **53**, 335–354.

Woodhouse, J.H., & Girnius, T.P., 1982. Surface waves and free oscillations in a regionalized Earth model. *Geophys. J. R. Astron. Soc.* **68**, 653–673.

Woodhouse, J.H., Giardini, D., & Li, X.-D., 1986. Evidence for inner core anisotropy from free oscillations. *Geophys. Res. Lett.* **13**, 1549–1552.

Ye, Z.R., 1989. Lateral variations of the mantle density and fluctuation of the core-mantle boundary. *Phys. Earth Planet. Inter.* **58**, 163–172.

Yeganeh-Haeri, A., Weidner, D.J., & Ito, E., 1989. Elasticity of $MgSiO_3$ in the perovskite structure. *Science* **243**, 787–789.

York, D., 1969. Least squares fitting of a straight line with correlated errors. *Earth Planet. Sci. Lett.* **5**, 320–324.

Yoshida, S., Sumita, I., & Kumazawa, M., 1996. Growth-model of the inner core coupled with the outer core dynamics and the resulting elastic anisotropy. *J. Geophys. Res.* **101**, 28085–28103.

Zhang, Y.-S., & Tanimoto, T., 1993. High-resolution global upper mantle structure and plate tectonics. *J. Geophys. Res.* **98**, 9793–9823.

Zhou, H.-W., 1996. A high-resolution P wave model for the top 1200 km of the mantle. *J. Geophys. Res.* **101**, 27791–27810.